UNIVERSITY OF CAMBRIDGE

The Mechanics of Layered Foams

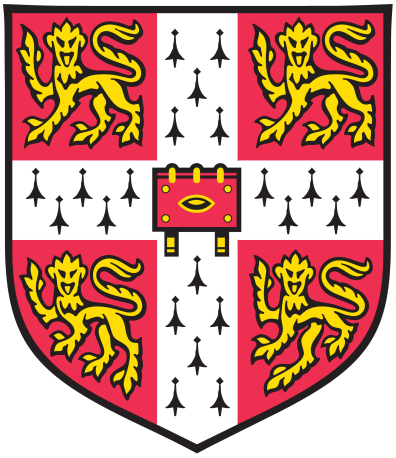

Author:

Adam Michael Boyce

Darwin College

Supervisor:

Prof Norman Fleck

Advisor:

Prof Vikram Deshpande

Submitted to the University of Cambridge for the degree of Doctor of Philosophy

February 2019

Preface

This thesis is submitted for the degree of Doctor of Philosophy at the University of Cambridge.

The work presented in this thesis was carried out during the period from October 2014 to February 2019 in the Cambridge University Engineering Department, under the supervision of Professor Norman A. Fleck. This research was sponsored by the Engineering and Physical Sciences Research Council (EPSRC) and industrial partners SABIC.

I hereby declare that this thesis is the result of my own work and to the best of my knowledge original except where reference is made to the work of others. It is not substantially the same as any that I have submitted, or, is being concurrently submitted for a degree or diploma or other qualification at the University of Cambridge or any other University or similar institution except as declared in the Preface and specified in the text.

Part II of Chapter 6 in this thesis was carried out in collaboration with Dr Harika Tankasala who aided in the formulation of analytical and finite element models.

This thesis contains approximately 32000 words, 67 figures, and 9 tables, which do not exceed the requirements of the Degree Committee.

Adam Michael Boyce
Centre for Micromechanics
Department of Engineering
University of Cambridge
Cambridge

February 2019

The Mechanics of Layered Foams

Adam Michael Boyce

This thesis contributes to the understanding of the mechanical response of layered and hybrid foam structures, such as the sandwich beam, and protective plates comprising foamed and solid materials. These materials may find applications ranging from critical structural members in aircraft wings and hulls of ships, to the packaging industry as well as protective components in bike helmets or dashboards of cars.

The thesis may be broadly split in two parts. Part I considers the influence of residual stress on the elastic indentation mode of collapse of a sandwich beam whilst the effect of residual stress on the elastic limit is also explored. Both are explored by the formulation of analytical models and subsequent numerical models and experiments. The elastic indentation collapse mode increases or decreases in the presence of a tensile or compressive residual stress. The elastic limit of a sandwich beam in bending is dictated by the occurrence of three competing mechanisms and the presence of residual stress, compressive or tensile, is found to negatively affect the load carrying capacity due to earlier yielding of the sandwich beam.

In Part II, the plane strain indentation response of a polycarbonate (PC) face sheet adhered to a polyvinyl chloride (PVC) foam substrate is measured. The deformation response is modelled by finite element simulations and, together with experimental observations, an analytical model is synthesised. The model assumes elastic membrane stretching of a face sheet on an elastic, perfectly-plastic foam foundation, and includes the role of shear-lag between face sheet and foam substrate. Finally, a parametric finite element study is performed on the indentation of a PC plate attached to a foam foundation consisting of a high-density PVC foam foundation which is in turn attached to a foundation of low-density foam. The purpose of such a hybrid material is to protect a structure underneath the foam foundation, whilst also providing similar indentation resistance at reduced weight.

Summary

This thesis contributes to the understanding of the mechanical response of layered and hybrid foam structures, such as the sandwich beam, and protective plates comprising foamed and solid materials. These materials may find applications ranging from critical structural members in aircraft wings and hulls of ships, to the packaging industry as well as protective components in bike helmets or dashboards of cars. The thesis may be broadly split in two parts. Part I is a study on the strength of sandwich beams. Here we provide novel insight into the bending behaviour of sandwich beams in the presence of a residual stress field. Part II of this thesis focuses on the indentation of a foam foundation protected by a solid polymeric layer in both the plane strain and axisymmetric (plate) configurations.

The thesis begins with an introduction and literature review and then an outline of the experimental procedures used to obtain the mechanical properties of the polyvinyl chloride (PVC) foams and polycarbonate (PC) face sheets that are used throughout the remainder of the thesis. Chapter 4 details an analytical model predicting the collapse load of a sandwich beam undergoing the elastic indentation mode of collapse during three point bending whilst subjected to a residual stress in the face sheets. A finite element model for a sandwich beam in three point bending and fully clamped conditions that incorporates a residual stress is developed and then used to validate the analytical model. An increase in collapse load is observed when a residual tensile stress is present in the upper face sheet, and vice versa in the case of a compressive residual stress. The boundaries of the collapse mode map are observed to shift with the magnitude of residual stress. It is observed that the level of residual stress in a sandwich beam is dependent on its material properties and sandwich geometry. Consequently, contours of maximum collapse load can be plotted on a collapse mode map. The model and results from this chapter indicate that it is possible to achieve significant increases in energy absorbed by a sandwich beam if a residual stress is present.

Second, the influence of residual stress on the elastic limit or first yield is explored by the formulation of analytical models and subsequently numerical models and experiments. The elastic limit of a sandwich beam in bending is dictated by the occurrence of three

competing mechanisms: i) yield of the face sheets via global bending of the sandwich structure, ii) yield via indentation i.e. local bending of the face sheet and simultaneous yield of the core adjacent to the indenter/point load, and iii) yield via shearing of the entire cross section of the core. The remainder of the chapter details an experimental implementation of residual stress in sandwich beams that comprise elasto-plastic face sheets and core, and the resulting effects on the elastic limit and plastic collapse. The experimental sandwich beam comprises polycarbonate face sheets and H200 PVC foam core. The limitations of the experimental method are discussed whilst the analytical models are validated for a number of sandwich beams using experiment and finite element methods. The experiments also give insight into the post-collapse behaviour of the sandwich beams and the associated final failure mechanisms. In general, the presence of residual stress, compressive or tensile, is found to negatively affect the load carrying capacity, and subsequent energy absorption behaviour of a sandwich beam.

Third, the plane strain indentation response of a PC face sheet adhered to a PVC foam substrate (on rigid foundation) is measured. Digital image correlation (DIC) is used to probe the indentation mode as a function of increasing indent depth. The effects of indenter size and shape (flat-bottom punch versus cylindrical roller) and of specimen length upon the collapse response and failure mechanisms are also explored. The deformation response is modelled by finite element simulations and, together with the observations, a simplified analytical model is synthesised. The model assumes elastic membrane stretching of a face sheet on an elastic, perfectly-plastic foam foundation, and includes the role of shear lag between face sheet and foam substrate. The chapter contains a comparison of the indentation response for a face sheet on foam substrate with that of a sandwich beam in 3-point bending. It is found that membrane stresses do not develop in the face sheet for the case of 3-point bending, and consequently the indentation response has negligible hardening post yield. An analytical model is developed to give direct insight into this alternative collapse mechanism.

Finally, a parametric finite element study is performed on the indentation of a thin PC plate attached to a foundation consisting of a high density PVC foam foundation which is in turn attached to a relatively thicker foundation of lower density PVC foam. The

purpose of such a hybrid material is to protect a structure underneath the foam foundation, whilst also providing similar indentation resistance at reduced weight. The following dimensionless parameters were varied in the finite element study; indenter diameter/facesheet thickness, and indenter diameter/high density foam foundation thickness. The plate was 70% lighter than the equivalent, reference thin PC plate supported by high density PVC foam only.

I dedicate this thesis to the strongest, most resilient and inspiring person I know:
my mother, Elizabeth Boyce.
This thesis would not exist without her lifelong love and support.

Acknowledgements

The research presented in this thesis is my own, however the reader will find that I have used the pronoun ‘we’rather than ‘I’throughout. I struggle to find the words to sufficiently describe the immense support I have received from my family, friends, and colleagues during the course of this doctoral degree and my education in general. I use ‘we’because I believe that this recognises and encapsulates the collective effort of all those who have been here for me during this four-year period and beyond, and to whom I am forever indebted.

I am eternally grateful to my supervisor Professor Norman Fleck who has been a source of immense kindness, support, patience, and guidance throughout my time at Cambridge. I would like to thank my advisor, Professor Vikram Deshpande for his wonderful kindness and encouragement. I am grateful for the support and funding of SABIC and to Dr Martin van Es of SABIC for his advice and guidance throughout.

The experimental aspects of this thesis could not have been achieved without the technicians Simon Marshall, Alan Heaver, Graham Smith, Stefan Savage, and the remaining members of the Division C technical staff. I would also like to thank Hilde Hambro-Fernandez for her support. I am immensely grateful for my place in the community at the Cambridge Centre for Micromechanics. I would also like to thank the amazing Harika Tankasala for her endless advice, guidance and patience.

I would like to recognise the unwavering support of my incredible friends, Gareth Kavanagh, Ian Campbell, and Mark Connaire. My Darwin friends, Anh Khoa, Fabio, Anjali, and Amani for always being there. And to Frederik Van Loock, Philipp Seiler, and Joe Stallard for their ceaseless friendship, support and banter, and for keeping me on my toes throughout my time in Cambridge.

To my parents for their lifetime of love and support, and my siblings for teaching me to never take life too seriously. To Paula and Sam for always being there for me, and Kevin for his ceaseless advice and support. To Polly, and that black cloud for teaching me about life.

Finally, this thesis would not have happened without the incredible support of Emma Donnelly and her mother Noeleen.

Contents

List of Figures

List of Tables

Chapter 1

Introduction

Microarchitectured materials such as lattices and foams are ubiquitous in nature. Such cellular materials range from cork and balsa wood, to the wings of a bird and the human bone structure. Man-made cellular materials derive their inspiration from nature and comprise many materials and structures. Polymer and metallic foams and lattices provide unique energy absorption and thermal insulation characteristics which are frequently used in myriad industries spanning aerospace, automotive, packaging, and construction technology.

1.1 Foams

Broadly speaking, a cellular solid is an interconnected network of struts and/or plates which form an array of cells that are arranged in a two dimensional, or three dimensional fashion (Gibson and Ashby (1999)). A two dimensional cellular solid is usually referred to as a lattice and an example of such a material is bee's honeycomb (see Figure 1.1(a)). On the other hand, foams constitute a three dimensional solid (either closed or open cell) and are usually manufactured using thermoplastic and thermoset polymers, ceramics, and a range of metals including stainless steel, aluminium, and copper. Examples of open and closed cell foams are shown in Figure 1.1(b) and (c). Foamed solids provide a

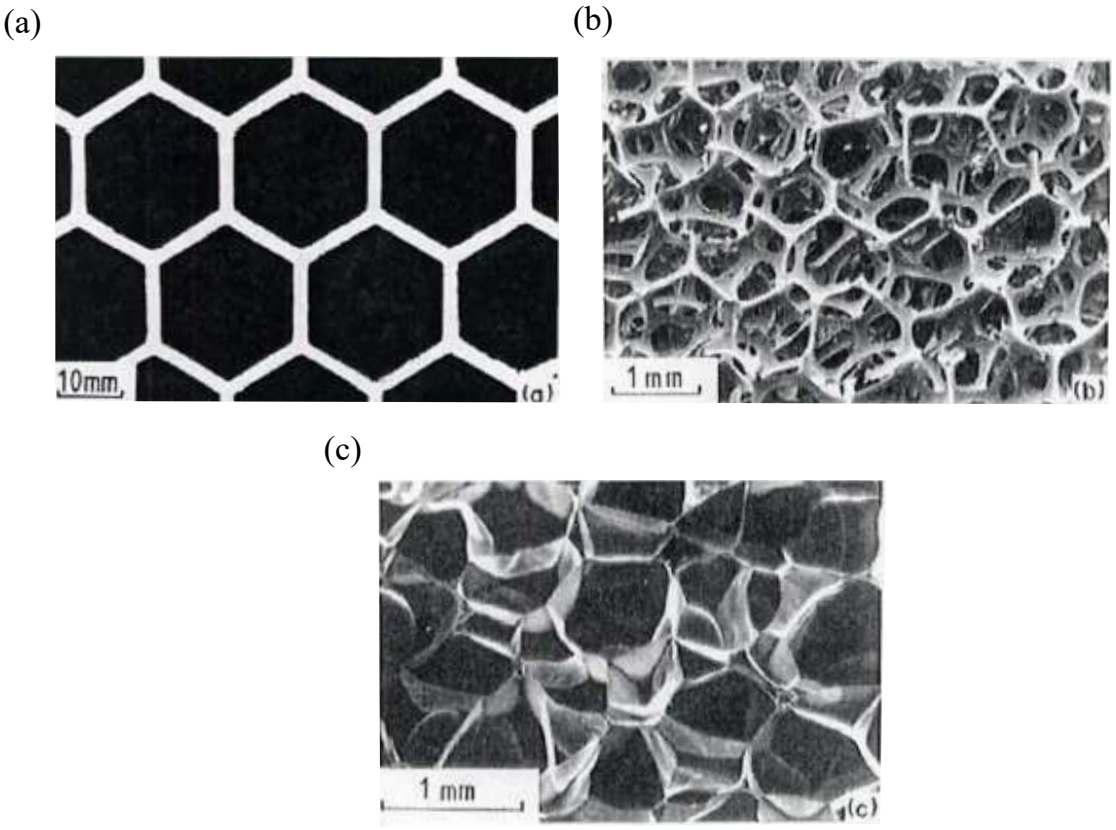

FIGURE 1.1: (a) Honeycomb lattice (b) open cell foam (c) closed cell foam (Adapted from Gibson and Ashby (1999))

dramatic increase in the properties available to the industrial engineer. There are three primary areas of application:

i) **Thermal**: Polymer foams are widely used as thermal insulators in a broad variety of applications from the coffee cup to space vehicles. Open cell metal foams (aluminium or copper) may also be used in heat exchanger applications. Microcellular foaming and more recently nanofoaming is being used to achieve ever improving thermal insulative properties.

ii) **Structural**: Nature provides an abundance of inspiration for structural applications of foams; cancellous bones, wood, and birds wings for example. These comprise of two layers of solid material separated by a foam providing superior flexural characteristics relative to the equivalent solid material. Man-made applications of such foam-based structures are panels for aerospace, automotive and marine applications.

iii) **Packaging and energy absorption**: Foams can undergo large compressive strains at constant stress and are therefore useful for absorbing large amounts of energy without experiencing excessive loads. This renders foams useful for applications such as cycling, or military helmets. They are frequently used in seating and bumpers of cars due to this constitutive behaviour along with their low stiffness.

Foams may also be used in buoyancy, acoustic insulation, and filtration applications. This thesis is concerned with the structural, and energy absorption properties of foams.

1.2 Layered and graded materials

Nature provides inspiration for countless man-made creations. Layered and graded materials are universal in natural materials and are a perfect example of such knowledge transfer between nature and humans. A layered or graded structure consists of a careful arrangement of a discrete or continuous combination of multiple materials with properties that may or may not vary with distance, see for example the owl's skull and maize leaf of Figure 1.2(b) and (c). An example of such materials are the often studied natural ceramic nacre, with its superior fracture properties that stem from its layered and composite structure.

A simple example and one of particular interest to the research carried out in this thesis is the sandwich structure. A sandwich structure comprises two stiff and strong face sheets separated by a lightweight material usually referred to as 'core'. Such a configuration provides a highly efficient material under flexural loading due to the increase in second moment of area as a result of the separation of the two stiff face sheets. Sandwich structures are ubiquitous in nature; the human skull is the most notable example (see Figure 1.2(c)). Man-made sandwich panels consist of metallic or fibre reinforced face sheets and polymer or metal foam, or lattice core. Typical sandwich panel configurations are shown in Figure 1.3(a), whilst a typical application, an aerospace structure, is shown in Figure 1.3.

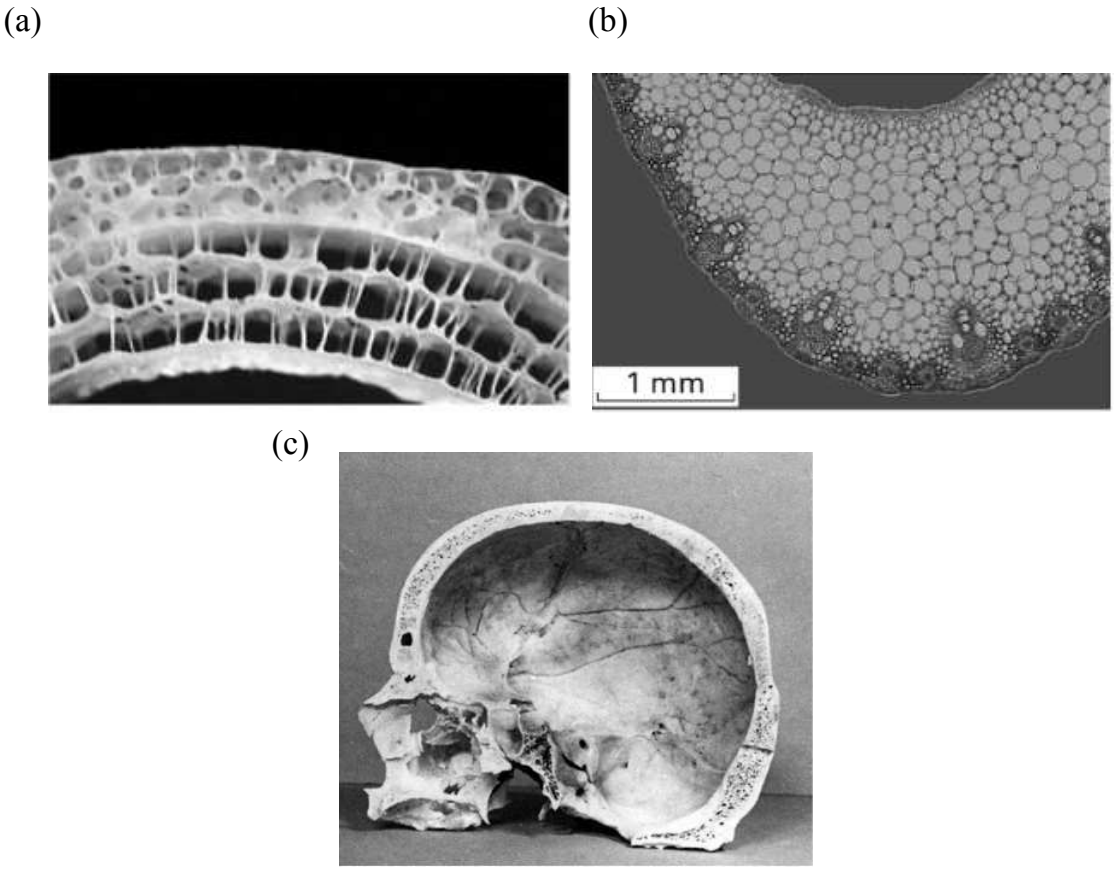

FIGURE 1.2: (a) Cross section of a tall eared owl's skull, note the graded and multilayered sandwich structure (b) Graded cellular structure of a maize leaf (c) Cross section of a human skull (Adapted from Gibson et al. (2010))

Both the linear elastic and collapse responses of sandwich beams and plates in flexure have been well documented, whilst there remains an absence of knowledge in the behaviour of a sandwich beam at the elastic limit and also in the post-collapse response. In addition, further insight is provided into the initial collapse, and elastic limit under the presence of a residual stress field which has the potential to provide novel strengthening methods for sandwich beams.

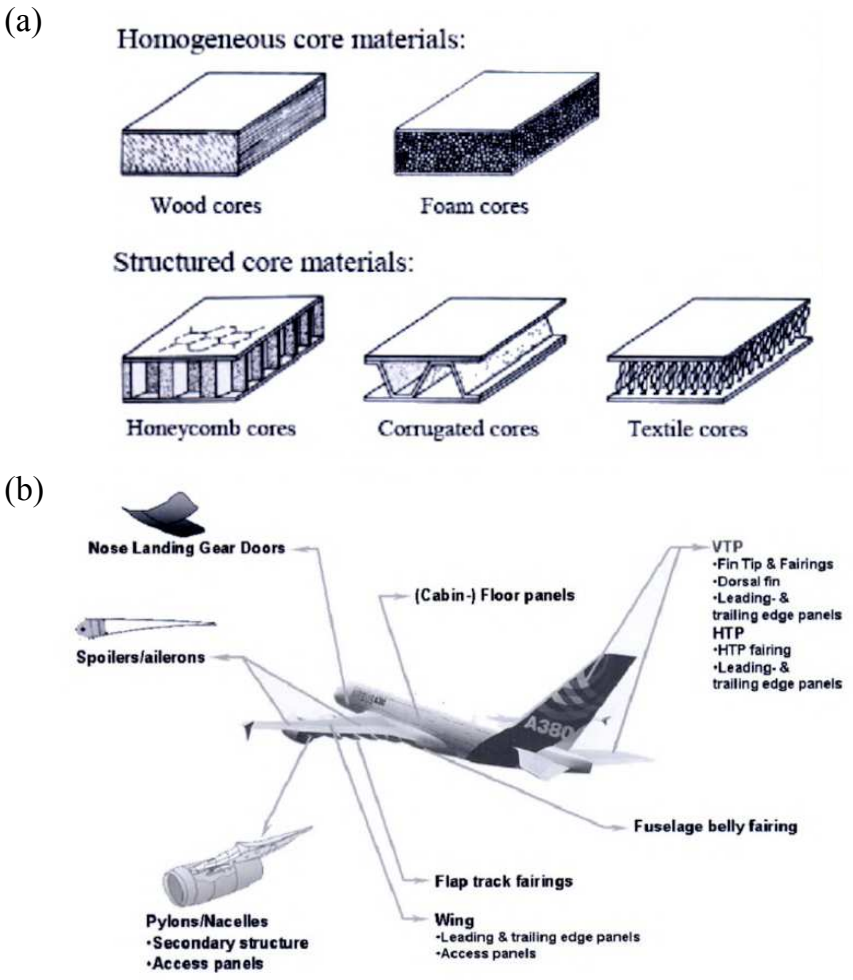

FIGURE 1.3: Sketches of (a) typical sandwich panels, and (b) typical applications of sandwich panels in an Airbus A380 Thomsen et al. (2005)

1.3 Scope of this thesis

The theme prevalent throughout this thesis is the analysis of indentation mechanics, capacity for energy absorption, and collapse of layered foam and sandwich structures. The primary objectives of this thesis are as follows

i) Investigate the influence of residual stress on the collapse mechanisms of sandwich beams.

ii) Study the first yield behaviour of sandwich beams, and subsequently the influence of residual stress on first yield.

iii) Understand and quantify the deep indentation behaviour of a foam protected by a reinforcing layer.

iv) Understand the indentation behaviour of a layered and graded foam plate.

There is a wealth of literature on the indentation and collapse of layered foam and sandwich structures. This is addressed in Chapter 2. Chapter 3 details the measurement of the uniaxial stress versus strain properties of a range of foam grades and a single grade of polycarbonate. This serves as a basis for the studies carried out in the remaining chapters. The influence of residual stress on the elastic indentation collapse response of sandwich beams with elastic face sheets and elastic-plastic core is probed in Chapter 4 and is carried out using analytical methods and supported by further finite element analyses. In Chapter 5, the point of first yield of sandwich panels is predicted which assumes a number of modes. The influence of residual stress on these first yield modes is then predicted using analytical methods and subsequently validated via experimental and numerical techniques.

The remaining chapters focus specifically on indentation of foam structures. Chapter 6 focuses on the plane strain, deep indentation behaviour of a polymer foam protected by a ductile polymer layer. Here the membrane stretching of the polymer layer during indentation is of primary concern. A new analytical model for such indentation behaviour is formulated and then validated and supported by experiments and finite element simulations. In Chapter 7, the indentation of multilayer foam plates protected by a polycarbonate layer is covered. This chapter uses experimental techniques and finite element simulations to design a graded or layered structure that achieves significant lightweighting whilst maintaining similar indentation properties.

Finally, Chapter 8 draws together the conclusions from each of the preceding chapters, whilst future and related work is suggested.

Chapter 2

Literature review

Summary

An overview of the literature on the mechanics of foam indentation and the deformation of hybrid layered foams is presented in this chapter. Firstly, the indentation of polymer and metal foams is addressed. We then describe the state of the art on the indentation of foams protected by a face sheet which are in turn supported by a rigid foundation. Subsequently, we cover the literature on the collapse of sandwich beams in bending, with a focus on the indentation mode of collapse. We also highlight the influence of residual stress on the deformation of composite materials as a precursor to the Chapters 4 and 5. Finally, the indentation and general deformation response of graded foams is discussed.

2.1 Indentation of foams

Polymeric foams typically exhibit a low ductility in tension (of only a few percent), but a high ductility in compression due to the formation of crush bands (Andrews et al. (1999); Gaitanaros and Kyriakides (2015); Jang and Kyriakides (2009)). The indentation strength of polymeric foams is comparable to their uniaxial yield strength due to the volumetric compressibility of the foam, and the indentation strength is only mildly

sensitive to the indenter geometry, see Andrews et al. (2001); Flores-Johnson and Li (2010); Olurin et al. (2000); Onck et al. (2001). For the practical application of foams to design for protective, energy absorbing packaging and for crash mitigation, it is desirable to enhance the indentation resistance of a foam substrate by the addition of a suitable face sheet.

The combination of a foam core and a stiff, strong face sheet commonly arises in sandwich construction: two stiff and strong face sheets are separated by a lightweight foam core. Sandwich panels are commonly used in flexural applications due to their low mass yet high stiffness and strength in bending. The early stage of plastic collapse of sandwich panels occurs by one of at least three competing mechanisms: face yield, core shear, and indentation (Ashby et al. (2000); Steeves and Fleck (2004b)). The present experimental and theoretical study gives additional insight into the indentation mode of collapse, and addresses the case where indent depths exceed the face sheet thickness such that the face sheet undergoes membrane action prior to failure. This regime is of high practical significance; yet it has received little attention in the literature.

Our primary study is concerned with the plane strain indentation response of a single PC face sheet bonded to a PVC foam substrate upon a rigid foundation. PC is chosen due to its high tensile strength and ductility, and it finds common use in impact-resistant transparent components such as masks for eye protection. Our study complements the experimental investigation of Mohan et al. (2007): they observed a significant elevation in the axisymmetric indentation strength of a metallic foam due to the presence of a stainless steel face sheet.

2.1.1 Existing models for the indentation of a face sheet, on a foam substrate

To date, the plane strain indentation response of a layer on foam substrate has been concerned primarily with indentation depths that are less than the face sheet thickness. In such a case, membrane stresses within the top layer play little role. For example, Biot (1937) analysed the indentation of an elastic layer, of thickness t and Young's

modulus E_f, on an elastic half-space, whilst Hetenyi (1961) simplified this problem by considering the idealised case of indentation of an elastic beam on an elastic spring foundation of modulus S by a line load P (per unit thickness), see Figure 2.1(a). Hetenyi found that the indentation load P is related to the indent depth v by

$$P = 1.52 S^{3/4} t^{3/4} E_f^{1/4} v \tag{2.1}$$

Soden (1996) extended the Hetenyi analysis for an elastic face sheet and a rigid perfectly-plastic foundation of strength σ_{cy} as shown in Figure 2.1(b). He found that

$$P = 2.1 t^{3/4} \sigma_{cy}^{3/4} E_f^{1/4} v^{1/4} \tag{2.2}$$

Shuaeib and Soden (1997) modified the foam substrate to that of an elastic-perfectly plastic foundation and more recently Pitarresi and Amorim (2011) considered the substrate to have a more general strain hardening characteristic as defined by a sequence of distributed springs.

Bostrom (1975) analysed the indentation resistance of a rigid, perfectly-plastic face sheet of strength σ_{fy} resting on a rigid, perfectly-plastic foundation and loaded by a transverse point force P. An upper bound for the collapse load was obtained by assuming a mechanism of 3 plastic hinges in the face sheet, to give

$$P = 2t\sqrt{\sigma_{fy}\sigma_{cy}} \tag{2.3}$$

Ashby et al. (2000) considered plane strain indentation of a metal face sheet (assumed as rigid, perfectly-plastic) on a metal foam core (also assumed to be rigid, perfectly-plastic) by a flat bottom punch of width $2a$. They gave an upper bound solution for the indentation load due to formation of 4 plastic hinges (adjacent to the punch) in the face sheet as sketched in Figure 2.1(c). They obtained a collapse load of

$$P = 2t\sqrt{\sigma_{fy}\sigma_{cy}} + 2a\sigma_{cy} \tag{2.4}$$

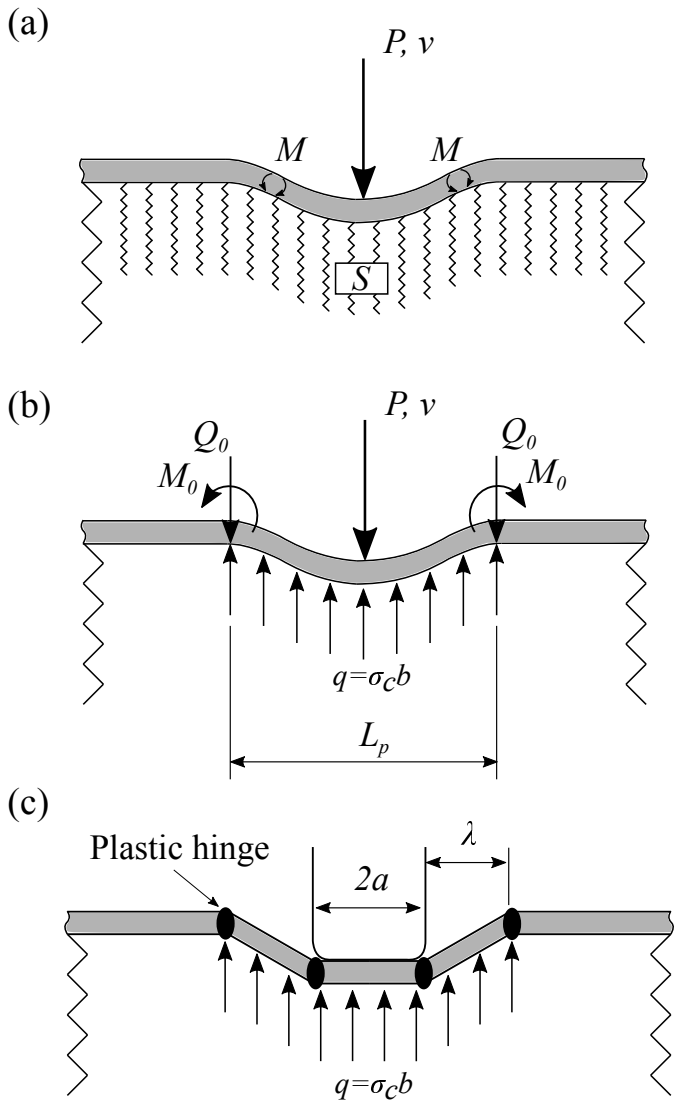

FIGURE 2.1: Sketches of (a) Hetenyi (1961) model with foundation modulus S, (b) Soden (1996) model, and (c) Ashby et al. (2000) upper bound model.

Chen et al. (2001), Bart-Smith et al. (2001), and McCormack et al. (2001) gave experimental support for this plastic collapse mechanism by performing 3-point and 4-point bend tests on sandwich beams. Whilst this mechanism exists at small indents (with respect to the face sheet thickness), it neglects the generation of membrane stretching within the face sheet at larger indent depths. The significance of such membrane stretching will be a focus of the present study.

Yu and Stronge (1990) realized the interaction between plastic bending and stretching in the regime of large indentation depth for a rigid, perfectly-plastic face sheet on a rigid,

perfectly-plastic foundation. Following an upper bound approach with an assumed velocity field, they obtained a 'membrane factor' to account for plastic stretching of the face sheet induced by large deflections. The indentation load P increases with the indent depth v in the stretching regime according to

$$P = 2\sqrt{\sigma_{fy}\sigma_{cy}tv} \tag{2.5}$$

An alternative model was developed recently by Rubino et al. (2010) based on experiments on Y-frame and corrugated core bi-layer made from stainless steel. The assumed collapse mechanism involves rotation about 4 plastic hinges, stretching of the face sheet between the inner and outer hinges, and shear deformation of the core (of depth c and shear strength τ_{cy}). The resulting indentation load versus displacement relation is

$$P = 2\sqrt{\sigma_{fy}\sigma_{cy}t(2v+t)} + c\tau_{cy} \tag{2.6}$$

More recent treatments of indentation on a foam substrate include combined analytical and finite element studies on the effect of plastic stretching of the face sheet due to large deflections Qin and Wang (2012); Qin et al. (2014); Xiao et al. (2016); Xie et al. (2011); Zhang et al. (2016). Both Xiao et al. (2016) and Xie et al. (2011) used an upper bound approach by assuming a velocity field and assumed that the face sheets and core are rigid, perfectly-plastic. Thereby, Xie et al. (2011) found the same collapse load as that given by Equation 2.5. Qin and Wang (2012) and Zhang et al. (2016) modelled the response of end-clamped sandwich beams under large deflections in their finite element calculations. Note that the above analyses, assuming rigid, perfectly-plastic behaviour, ignore elastic stretching of the top face sheet and elastic compliance of the foam core. It is anticipated that the role of elastic deformation is significant in bi-layers where each phase has a high value of yield strain, such as PC face sheets on a polymer foam core, as noted by Boyce et al. (2017). In order for membrane stresses to exist within the face sheet, there must be load transfer between the face sheet and the foam substrate. This problem of load diffusion between a strip and a substrate has a long and illustrious history, see for example Koiter (1966) and Muki and Sternberg (1967). Here, we shall

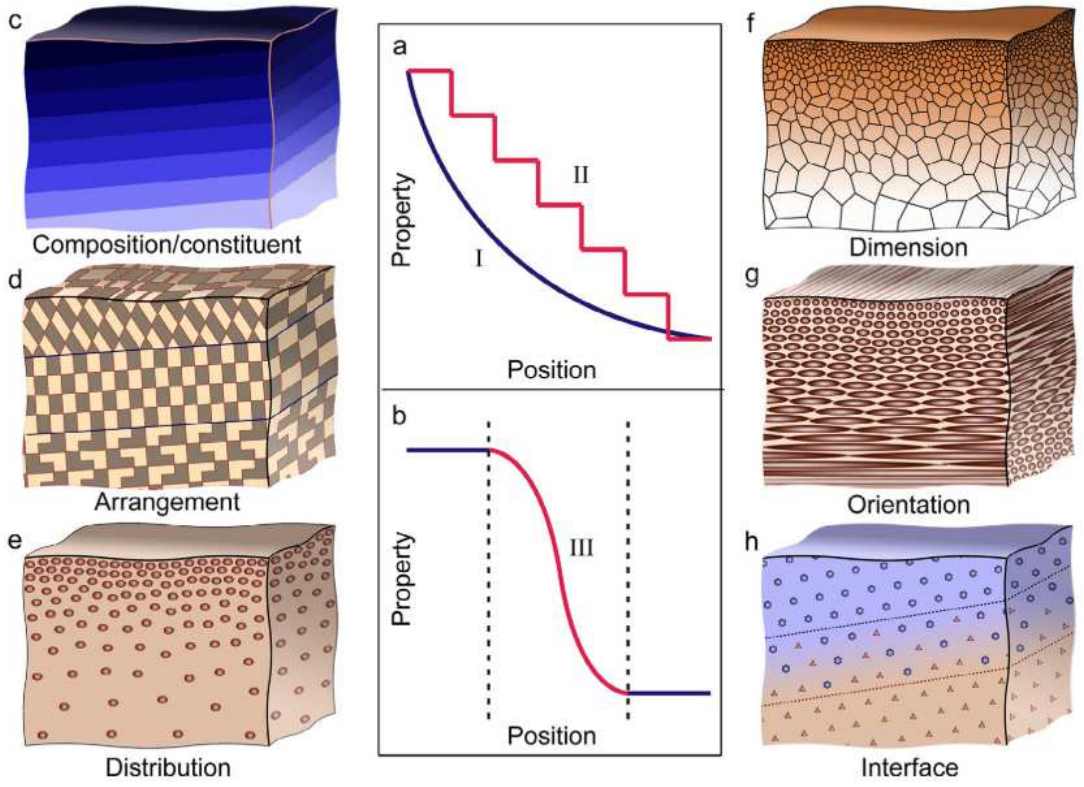

FIGURE 2.2: Local property profiles and basic forms of gradients in biological materials: (a) Local properties change either gradually (I) or in a stepwise manner (II) through the entire material volume; (b) Local properties vary continuously across the interface between dissimilar components; (c – g) The gradients in biological materials are fundamentally associated with the changes in chemical compositions/constituents (c) and structural characteristics, including the arrangement (d), distribution (e), dimensions (f), and orientations (g) of building units; (h) Gradient interface in biological materials. Adapted from Liu et al. (2017).

present a simple analytical model for membrane stretching of the face sheet during indentation, based on these classical ideas.

2.1.2 Indentation of gradient materials and structures

2.1.2.1 Basic results and modelling of indentation of gradient materials

Functionally graded materials (FGMs) are spatial composites that display discrete or continuously varying compositions over a definable geometrical length. The gradients can be continuous on a microscopic level or layers comprised of metals, ceramics and polymers. Gradient structures typically involve the variation of a particular material

property with distance e.g. change of Young's modulus with depth in a material. This usually stems from the change in the microstructure over the main dimensions of a specimen. A simple example of this being the change in cell size in a foamed material; this was highlighted in Chapter 1 where natural materials such maize leaves and animal/human skulls were concerned. Liu et al. (2017) provide insight into the bio-inspired nature of man-made graded material design; Figure 2.2 shows some biological gradient structures that inspire man-made designs.

The seminal work on indentation of solids with gradients in elastic properties was carried out by Giannakopoulos and Suresh (1997a,b). They took an analytical and numerical approach and gave the following key findings on the indentation of solids with varying Young's modulus with depth

- It was found that a decreasing elastic modulus with depth results in the spreading of stresses towards the surface rather than to the interior.
- An increasing elastic modulus results in diffusing the stresses towards the interior of the half-space.
- The influence of the Poisson ratio is strong whenever the elastic modulus is increasing with depth, and is weak whenever the elastic modulus is decreasing with depth. There is a competing constraint between the elastic modulus distribution and the increasing Poisson ratio towards the incompressibility limit.
- In all cases the load diffusion is far smoother for the graded material than for sharp layered cases (e.g. films on substrate), thus avoiding severe stress jumps that may promote delaminations or other forms of damage.
- On the other hand, a decreasing elastic modulus with depth results in a large surface deformation which is less localized than the surface deformation for increasing elastic modulus.

A variety of other authors have expanded upon these models and insights by Giannakopoulos and Suresh (1997a,b). Martin et al. (2002) provided a three dimensional

solution for indentation of a functionally graded material with exponentially varying elastic properties. Vasu and Bhandakkar (2018) modelled the plane strain solution of a material with exponentially varying elastic modulus. Giannakopoulos and Pallot (2000) proposed an indentation model for plane strain indentation by cylindrical punch of a functionally graded material given as an elastic halfspace in which the elastic modulus varied with depth according to a power law. Ke and Wang (2006) used a similar approach but gave a solution for an arbitrary variation in elastic properties with depth. They used a layered approach where the elastic properties changed with the layers and the variation was captured via a series of piecewise linear curves. Giannakopoulos (2002) explored the variation of plastic behaviour with depth during the indentation of a metal substrate. Variations in yield strength were attributed to the change in dislocation density with depth. They found that materials with increasing yield stress with depth were found to suppress residual stress on the surface whilst the converse promoted surface residual stress. Other authors have considered loading of gradient or layered structures, see Li et al. (2001).

Most studies outlined so far consider a decreasing elastic modulus with depth as being advantageous for a variety of reasons such as energy absorption, residual stress reduction etc. Ziegler and Kraft (2014) considered soft materials where an increase in elastic modulus with depth was required to reduce the surface tensile stresses during indentation and delay the onset of cracking relative to the equivalent homogeneous material.

2.1.2.2 Indentation of functionally graded foams

The use and research of functionally graded foams generally revolves around one particular objective; lightweighting whilst achieving sufficient energy absorption during impact or denting. A secondary objective typically considered is the protection of an underlying structure by a functionally graded foam, which may also be protected by an outer layer. Cui et al. (2009) carried out numerical analysis on impact of functionally graded foam specimens in compression. They observed that energy absorption capacity was superior to a homogenous specimen when the density decreased with depth. Although it was observed that this effect was not applicable during high velocity. They

also highlighted that if the range of material density between top and bottom of the specimen increases then energy absorption capacity can be increased.

Chapter 7 will focus on both of these issues related to indentation and localised deformation of such structures. There have been a small amount of studies that consider indentation of sandwich panels with graded foam cores, or the indentation of graded foams protected by thin layers. Both Mu et al. (2015) and Xiao et al. (2016), described an analytical model based on a virtual work formulation for the axisymmetric indentation of a plastic membrane on a core in which the plateau stress linearly decreased with depth. See Apetre et al. (2008) for another study on the energy absorption of gradient sandwich panels.

2.2 Collapse of sandwich beams under quasi-static bending

2.2.1 Elastic behaviour of sandwich beams in bending

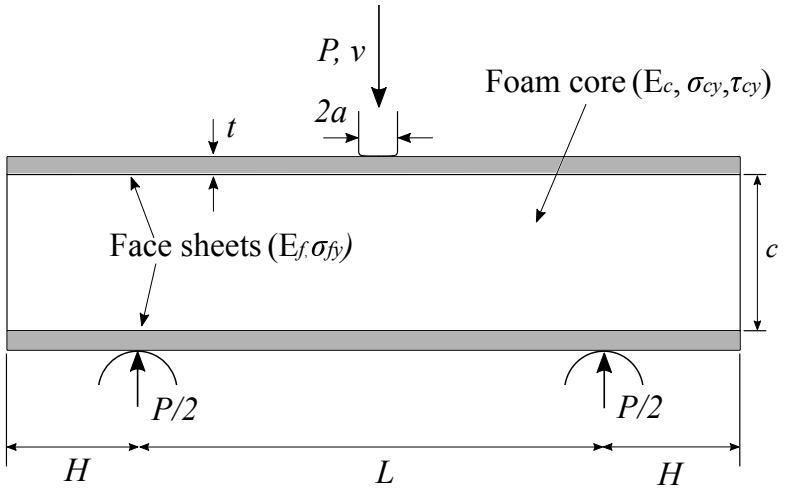

FIGURE 2.3: Simply supported geometry for a sandwich beam of thickness b into the page.

Consider the sandwich beam of span L shown in Figure 2.3. The beam is loaded by a flat-bottom punch of width $2a$. Assume that the face sheets and core behave as elastic,

perfectly-plastic solids of plane strain Young's moduli E_f and E_c , and of yield strengths σ_{fy} and σ_{cy}, respectively. The shear strength of the foam is given as τ_{cy}. At small values of punch displacement $v << t$, both the face sheets and core behave in an elastic manner such that the load P increases linearly with v according to Ashby et al. (2000) as

$$v = \frac{PL^3}{48(EI)_{eq}} + \frac{PL}{4(AG)_{eq}} \tag{2.7}$$

where $(EI)_{eq}$ is the equivalent flexural rigidity and $(AG)_{eq}$ is the equivalent shear rigidity of the sandwich beam; these relate to the elastic moduli and cross-sectional dimensions of the beam as

$$(EI)_{eq} = \frac{E_f bt(t+c)^2}{2} + \frac{E_f bt^3}{6} + \frac{E_c bc^3}{12} \tag{2.8}$$

and

$$(AG)_{eq} = \frac{G_c b(t+c)^2}{2} \tag{2.9}$$

Here, G_c is the shear modulus of the core.

A sandwich panel loaded in bending may collapse in a variety of ways and we shall outline all collapse modes in turn. We refer to these as collapse mechanisms, and the active mode of collapse is determined by the sandwich geometry and its constituent material properties. Broadly speaking, there are three mechanisms of collapse; face yield, core shear, and indentation. Subsequently we may differentiate between elastic and plastic indentation modes of collapse. Elastic indentation is applicable to stiff, elastic brittle face sheets such as CFRP or GFRP whilst plastic indentation is generally considered for elastic-plastic face sheets such as aluminium or stainless steel. In addition there are two modes of core shear collapse. Furthermore, it is found that boundary conditions (simply supported vs clamped) alter the operative collapse mechanisms. For an extensive description of the mechanics and design of sandwich structures, the reader is referred to the works of Plantema (1966), Allen (1969), and Zenkert (1995).

2.2.2 Face yield

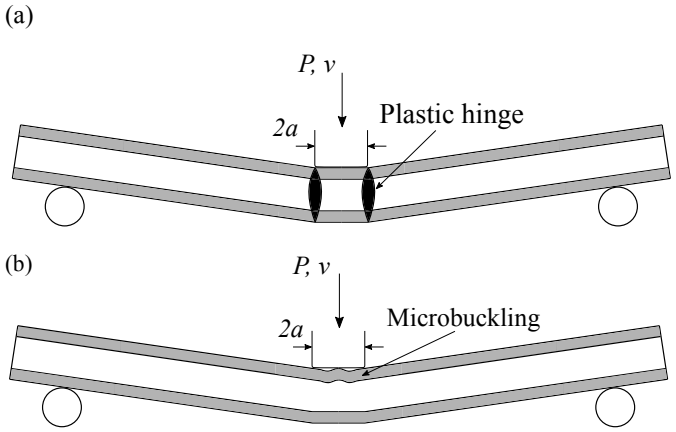

FIGURE 2.4: Sketches of (a) face yield, and (b) face microbuckling collapse

Face yield or microbuckling occurs when the axial stress in the sandwich face attains the yield or microbuckling strength of the face material. In the case of an elastic-brittle facesheet, failure occurs in the tension-loaded face sheet and for long-fibre composite face sheets, microbuckling occurs on the compression-loaded facesheet at a compressive stress σ_{fy} less than the tensile strength of the face sheet (see Figure 2.4(a)). The collapse load P_M (the subscript M refers to microbuckling), under simply supported conditions is predicted using the following expression:

$$P_M = \frac{4bt(t+c)}{L-2a}\sigma_{fy} \tag{2.10}$$

or for clamped specimens (Tagarielli and Fleck (2005)), the following holds

$$P_M = \frac{8bt(t+c)}{L-2a}\sigma_{fy} \tag{2.11}$$

If the facesheets are elastic-plastic then we consider an upper bound solution in which the entire midsection of the beam attains yield, both core and facesheets yield simultaneously (see Figure 2.4(b)). The expression that predicts this form of collapse is as follows:

$$P_{FY} = \frac{4bt(t+c)}{L-2a}\sigma_{fy} + \frac{bc^2}{L-2a}\sigma_{cy} \tag{2.12}$$

A similar result follows when clamped conditions are considered. There are now two hinges at the boundaries (Tagarielli and Fleck (2005)). The collapse load is as follows

$$P_{FY} = \frac{8bt(t+c)}{L-2a}\sigma_{fy} + \frac{2bc^2}{L-2a}\sigma_{cy} \tag{2.13}$$

It is clear that both the microbuckling load and face yield are equivalent, with the exception of an extra term.

2.2.3 Core shear

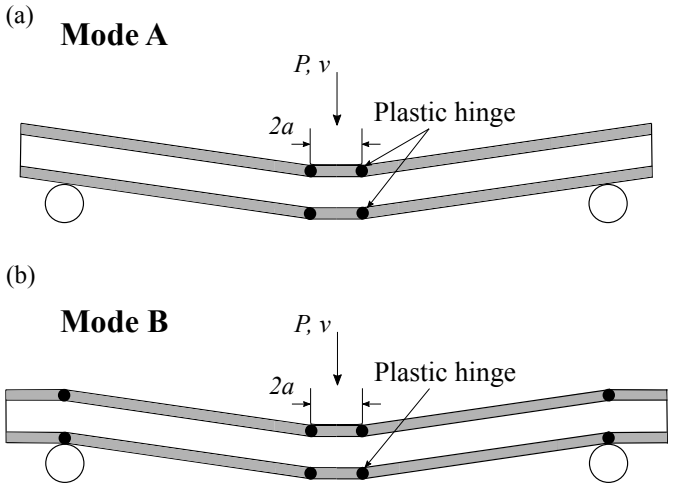

FIGURE 2.5: Sketches of (a) mode A, and (b) mode B core shear collapse

When a sandwich beam is loaded in three-point bending, in general, the transverse shear force is carried mostly by the core and collapse of the beam may occur via yielding of the core which is driven by a specific combination of geometry and material properties. There are two variations on the core shear collapse mode as shown in Figure 2.5. Mode A involves the formation of four plastic hinges in the face sheets and and shearing of the core over the length $(L/2+2H)$. H is defined as the overhang. The collapse load for mode A is as follows

$$P_{CS} = \frac{2bt^2}{L-2a}\sigma_{fy} + 2\tau_{cy}b(t+c)\left(1+\frac{H}{L-2a}\right) \tag{2.14}$$

Mode B involves the formation of four additional plastic hinges at the supported ends of the beam and shearing behaviour of the length L. The collapse load of a beam in mode B, core shear is described using

$$P_{CS} = \frac{2bt^2}{L-2a}\sigma_{fy} + 2\tau_{cy}b(t+c) \tag{2.15}$$

Subsequently, a transition between the two modes can be found where H_t is given as

$$H_t = \frac{t^2\sigma_{fy}}{2c\tau_{cy}} \tag{2.16}$$

Mode B is the only permissible core shear collapse mode for clamped conditions and follows Equation 2.15 (Tagarielli and Fleck (2005)). If the face sheets are loaded elastically, as in the case of GFRP and CFRP face sheets, then the contribution of the face sheets can be neglected by allowing $\sigma_f = 0$ in Equations 2.14 and 2.16.

2.2.4 Indentation

It is commonly assumed that the indentation of a face sheet on a foam substrate is an adequate representation of the indentation of a sandwich beam under 3 point or 4 point bending. We shall show mater in the thesis that this is not always the case.

2.2.4.1 Plastic indentation

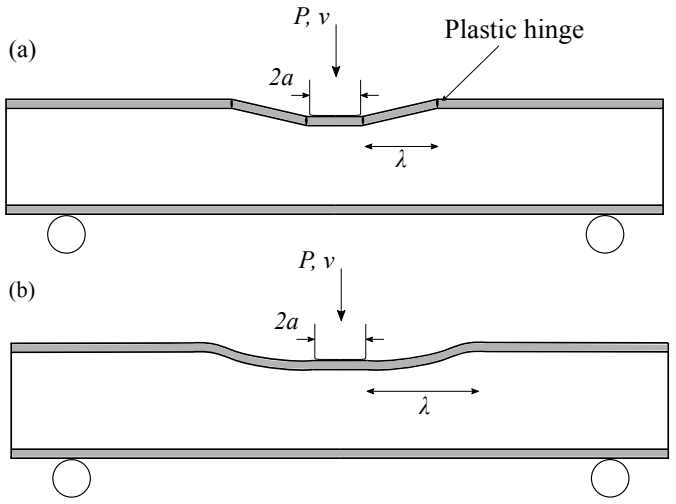

FIGURE 2.6: Sketches of (a) plastic and (b) elastic indentation collapse

Two modes of indentation failure may exist; elastic and plastic. Plastic indentation has typically been applied to sandwich panels comprised of ductile metal facesheets and metal foam cores. The mechanism of collapse assumes the formation of four plastic hinges adjacent to the indenter and at the boundaries of the indentation region, a distance λ from the indenter. The collapse load can be obtained using an upper bound calculation

$$P_{PI} = \frac{4M_p}{\lambda} + (a+\lambda)b\sigma_c \tag{2.17}$$

The full plastic moment, M_p is given as $M_p = \sigma_f bt^2/4$. If P_{PI} is minimised with respect to λ the expression for the peak load, described by Ashby et al. (2000), is found to be

$$P_{PI} = 2bt(\sigma_c\sigma_f)^{\frac{1}{2}} + 2ab\sigma_c \tag{2.18}$$

The indentation region is given by $\lambda = t\sqrt{\sigma_f/\sigma_c}$.

2.2.4.2 Elastic indentation

Steeves and Fleck (2004b) modelled the elastic indentation of sandwich panels under three point bending, suitable to elastic face sheets and plastic core, as an elastic beam upon an ideally plastic foundation. During collapse, the face sheet local to the indenter buckles elastically whilst the core yields. The peak load is as follows

$$P_{EI} = bt\left(\frac{\pi^2(t+c)E_f\sigma_{cy}^2}{3L}\right)^{\frac{1}{3}} \tag{2.19}$$

Tagarielli et al. (2004) extended this analysis to the elastic indentation of sandwich panels with clamped boundary conditions. The resulting peak load was given as

$$P_{EI} = bt\left(\frac{2\pi^2(t+c)E_f\sigma_{cy}^2}{3L}\right)^{\frac{1}{3}} \tag{2.20}$$

2.2.5 Collapse mechanism maps

The operative collapse mode is the one occuring at the lowest load relative to the others, a load which may be calculated as described in the preceding sections. It is convenient, for design purposes, to have graphical methods to portray the competing collapse mechanisms. Gibson and Ashby (1999) developed these methods and formed collapse mode maps for specific face sheet/core combinations which gives the regions of dominance of each collapse mode for a given combination of geometrical parameters. Other authors have made use of these maps for a variety of sandwich beam systems (Petras and Sutcliffe (1999); Triantafillou and Gibson (1987a,b)). An example of a collapse mode map for aluminium face sheets and aluminium alloy foam core is shown in Figure 2.7, where the normalised collapse load $\bar{F} = F/(2bL\sigma_f)$ is plotted as a function of t/c and c/L. Also plotted are contours of constant $\bar{F}$ for each collapse mode, and constant contours of $\bar{M}$, the normalised mass of the beam (based on the density of the core (ρ_c) and the face sheet (ρ_f) where

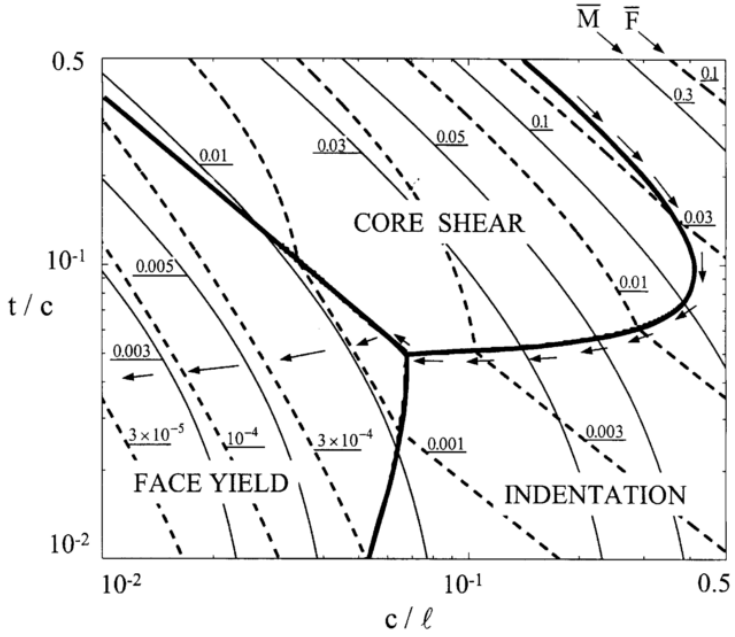

FIGURE 2.7: An example of a collapse mode map for aluminium face sheets and aluminium alloy foam core. Adapted from Chen et al. (2001)

$$\bar{M} = \frac{M}{\rho_f b L^2} = 2\bar{t} + \bar{c}\frac{\rho_c}{\rho_f} \tag{2.21}$$

Both $\bar{F}$ and $\bar{M}$ are useful when obtaining a minimum weight design for a given collapse load.

2.3 Prestressing and the use of residual stress as a strengthening mechanism

The idea of prestressed materials exists predominantly in civil engineering applications i.e. that of prestressed steel in concrete. Steel reinforced concrete exists in order to improve the poor tensile properties of concrete (particularly under flexural loads). Further improvement is achieved via the prestressing of the steel; it exerts a compressive load on the tensile face of a beam in flexure, for example, and thereby protecting it from fracture. To date, this mechanism has widely been used in concrete, however, limited use has also occurred in other materials, such as carbon or glass fibre reinforced

polymers (Daynes et al. (2010, 2008); Fancey (2011); Motahhari and Cameron (1998); Tuttle (1988); Tuttle et al. (1996)).

One main application for prestressed composites are control surfaces on aircraft, where traditional structures such as ailerons can be replaced by adaptive prestressed structures that can selectively alter the component curvature (Daynes et al. (2008)). Improvement of impact resistance is another prime area for the use of prestressed materials; Motahhari and Cameron observed that prestressing glass fibre epoxy composites increased the impact strength of laminates by up to 33% (Motahhari and Cameron (1998)). Other authors have found similar results (Fazal and Fancey (2014); Nishi et al. (2014)). Motahhari and Cameron (1998) carried out a further study on their material in flexure, noting that the strength and stiffness increased substantially. The work of Tuttle, and Daynes outlined analytical (based on laminate plate theory) and finite element models on the introduction of prestresses to such materials (Daynes et al. (2010); Tuttle (1988)). Mines and Li (2000) studied the influence of residual stress on the quasi static bending response of carbon fibre composites and found a resulting increase in peak load.

Richards and Richards (1990), designed a foam structural member with internal prestressed tendons made from twine, or steel cables. It was found that the flexural performance of such material improved upon application of a prestress to the tendons. To the best of the authors knowledge, there has been no work carried out on the flexural performance of prestressed foam sandwich beams and this leaves room for further work in this area.

Chapter 3

Material characterisation

3.1 Introduction

In order to successfully carry out further studies on the mechanical behaviour foams, and hybrid foam structures, it is important to understand the basic mechanical properties of both the foam and the reinforcing material, polycarbonate (PC). In particular, studies on the indentation and flexural behaviour of these materials will require extensive compression and tensile characterisation; it is thus necessary to develop a reliable and accurate test methodology. The following chapter will outline this test methodology as well as the basic mechanical properties of Lexan 9020-112 polycarbonate and three grades of polyvinyl chloride (PVC) foam. The foams are manufactured by Divinycell, with product names: H35, H80, and H200 and having densities of 38, 80, and 200 kg/m^3 respectively.

The mechanical properties of the above materials have been covered widely before, however the present chapter details the material properties used for analytical and numerical studies carried out in the remaining chapters and is thus a necessary addition to this thesis.

3.2 Experimental methods

3.2.1 Foam material characterisation

The influence of strain rate on each material in both compression and tension was assessed. All materials were tested at $10^{-3}, 10^{-2}, 10^{-1}s^{-1}$ strain rates in the z-direction. In addition to this, a study was carried out on the potential anisotropy introduced as a result of the manufacturing process. The foams were supplied in large boards which were 25mm thick and tested in x, y, z, and 45° to the x-y directions (see Figure 3.1) at a strain rate of $10^{-3}s^{-1}$. In the case of tension, the foams were not tested in the z direction. All foams were tested in a 5500R-6025 Instron machine. Load cells of 1.5kN, 5kN, and 15kN were used for each of the foams, H35, H80, and H200 respectively. The variation in load cells ensured that the measured loads achieved the greatest resolution possible for all foams. An EIR LE-05 laser extensometer was used to make all displacement measurements between two 2mm highly reflective adhesive tags. The laser extensometer had a resolution of 1μm and a variable range between 5mm and 127mm.

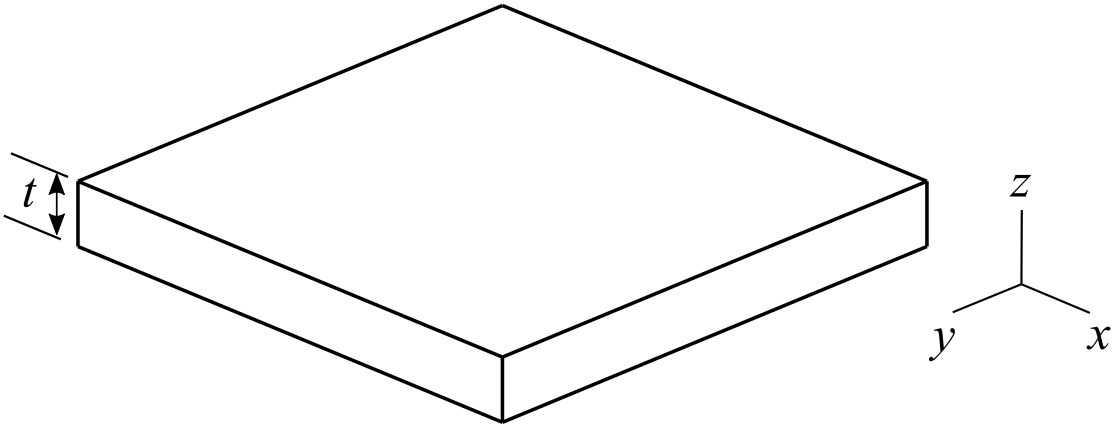

FIGURE 3.1: Loading directions

3.2.1.1 Compression tests

The three grades of foam were loaded between compression platens at three different strain rates and in four different directions. The specimen used was a 25mm cube, which was manufactured on a milling machine to ensure that all faces were parallel

and orthogonal to one another. The gauge length and displacement were both measured between the reflective tags placed on the loading platens. Three repeat tests were carried out for each strain rate and each direction.

3.2.1.2 Tension tests

Tension specimens were tested and manufactured using purposely designed loading rigs and fixtures. The tension specimens themselves (Figure 3.2) were loaded via aluminium loading shackles and pins (see Figure 3.3), the motivation for such a design was to ensure that no crushing of the foam occurred during testing. Two aluminium tabs were bonded to each end of the dogbone to ensure that no indentation of the foam occurred. 10mm holes were centrally located and placed in the aluminium tabs and dogbone to ensure that the 10mm pins applied the load through the centre of the dogbone.

The prepartion procedure for the dogbone samples was carried out as follows. All four aluminium tabs were bonded simultaneously. The tabs were abraded using coarse emery paper to promote adhesion and then rinsed using acetone. Once they were dry, Araldite Rapid epoxy adhesive was then used to bond the tabs to the dogbones. A 10mm pin (which was attached to a flat baseplate) was then passed through the two aluminium tabs (with adhesive applied) and the dogbone, this was done on both ends of the specimen and ensured that all holes were correctly located and aligned. A 4.5kg weight was placed on either end to ensure full contact between the aluminium tabs and foam. Plates, spanning the length and width of the dogbone were then clamped either side of the specimen to ensure that all aluminium tabs were orientated correctly and aligned parallel with the edge of the dogbone. The specimens remained in this configuration for one hour prior to removal of the weights, plates, and clamps.

The dogbones themselves were machined in such a way that the centre of the loading holes were in line with the centre line of the specimen. This was carried out by clamping a 200mm x 75mm x25mm block in a purposely made jig. The holes were drilled in either end, and without unclamping the radius and gauge length were machined. All relevant dimensions were referenced to the end of the specimen as shown in Figure 3.2.

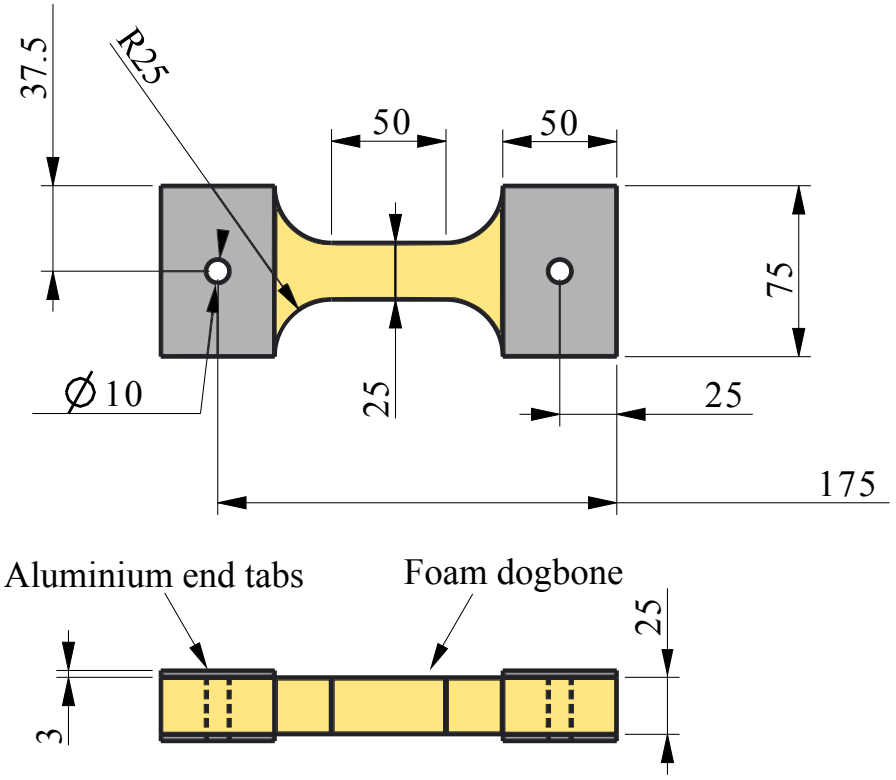

FIGURE 3.2: Tensile dogbone specimen (all dimensions in millimetres)

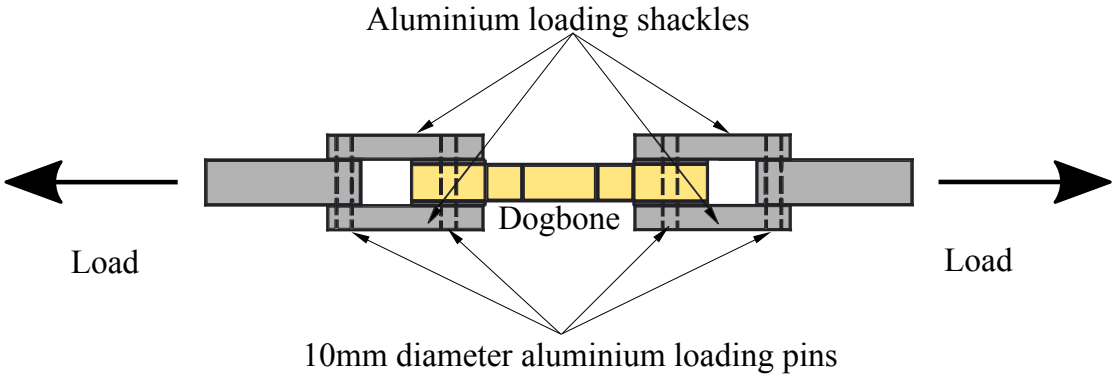

FIGURE 3.3: Tensile dogbone specimen loading configuration

The three grades of foam were loaded at three different strain rates and in three different directions. The displacement was measured using a laser extensometer; the gauge length and displacement were measured between the reflective tags placed at a distance of 40mm apart. This distance corresponded with the centre of the gauge length. Three repeat tests were carried out for each strain rate and each direction (except for the z-direction).

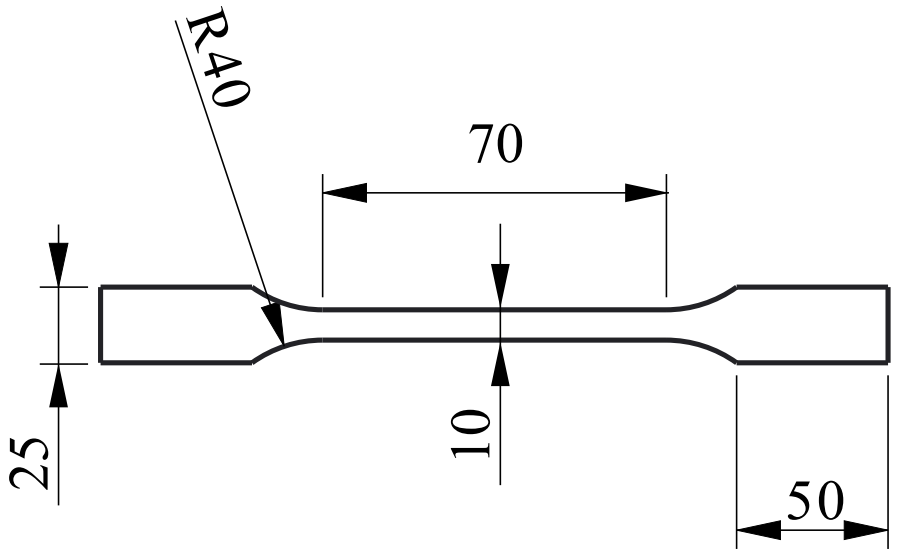

FIGURE 3.4: Tensile dogbone specimen (all dimensions in mm)

3.2.2 PC material characterisation

3.2.2.1 Tension tests

For the tensile tests, Lexan 9020-112 polycarbonate was acquired in large sheets of 1mm thickness. Dogbone specimens were machined using a milling machine with the dimensions as shown in Figure 3.4. The ends of the dogbone were gripped in a 5500R-6025 Instron machine and loaded at rates which corresponded to strain rates in the range $10^{-3}, 10^{-2}, 10^{-1} s^{-1}$. An EIR LE-05 laser extensometer was used to make all displacement measurements between two 2mm highly reflective adhesive tags, a distance of 60mm apart within the gauge section. Three repeat tests were carried out for each strain rate.

3.2.2.2 Compression tests

Compression tests were carried out on cylindrical specimens with a height of 12mm and diameter of 12mm. The tests were performed on the Instron machine (as mentioned previously) between loading platens lubricated with PTFE spray. The laser extensometer

was used to make displacement measurements between the two platens and the specimen was loaded at three different strain rates $10^{-3}, 10^{-2}, 10^{-1} s^{-1}$. Three repeat tests were carried out for each strain rate.

3.3 Results and discussion

3.3.1 Foam properties

Tables 3.1 and 3.2 summarise the mechanical properties found during the material characterisation process in the out-of-plane and in-plane directions respectively. A comparison is also drawn between the properties measured during this studies and those measured by the manufacturer DIAB (2005). There was negligible scatter between the three repeated tests in all compression and tension experiments. It is clear that small differences exist between the experimental work in this study and that of the manufacturer. The ductility of the materials in this study varied significantly from that of the manufacturers measurements, this may be due to the difference in strain measurement or testing methods. It must be noted that all stresses σ and strains ε, are given as nominal values in the remaining sections.

3.3.1.1 Influence of loading direction and strain rate

It is evident that strain rate plays a moderate role in the compressive and tensile deformation (Figures 3.5 (a), (c) (e)) behaviour of PVC foams. In compression, higher strain rates give higher yield strengths and plateau strengths. Little effect is seen on the foam stiffness. In tension, the foam experiences higher yield strengths and stiffness with increasing strain rate. However, the strain to failure decreases with strain rate, whilst the failure strength increases. This tensile behaviour is similar to that found by Poapongsakorn and Kanchanomai (2011) and Deshpande and Fleck (2001) who tested a range of Divinycell foams.

TABLE 3.1: Out-of-plane mechanical properties (z direction)

	Compressive strength (MPa)	Compressive modulus (MPa)	Tensile strength (MPa)	Tensile modulus (MPa)	Failure strain (%)
H35-Experiment	0.423 ± 0.006	27.8 ± 0.393	N/A	N/A	N/A
H35-Manufacturer	0.5	40	1	49	N/A
H80-Experiment	1.321 ± 0.009	61.9 ± 4.4	N/A	N/A	N/A
H80-Manufacturer	1.4	90	2.5	95	N/A
H200-Experiment	5.363 ± 0.248	134.88 ± 2.062	N/A	N/A	N/A
H200-Manufacturer	5.4	310	7.1	250	N/A

TABLE 3.2: In-plane properties (x and y directions)

	Compressive strength (MPa)	Compressive modulus (MPa)	Tensile strength (MPa)	Tensile modulus (MPa)	Failure strain (%)
H35-Experiment	0.335 ± 0.003	14.86 ± 0.469	0.9 ± 0.044	29.361 ± 1.578	5.353 ± 0.414
H35-Manufacturer	N/A	N/A	N/A	N/A	N/A
H80-Experiment	0.84 ± 0.009	38.271 ± 3.042	1.95 ± 0.088	53.307 ± 4.051	11.623 ± 0.967
H80-Manufacturer	1	37	2	75	6.5
H200-Experiment	3.446 ± 0.056	124.67 ± 1.973	5.755 ± 0.07976	160.541 ± 3.76617	15.413 ± 0.492
H200-Manufacturer	4	120	4.8	210	10

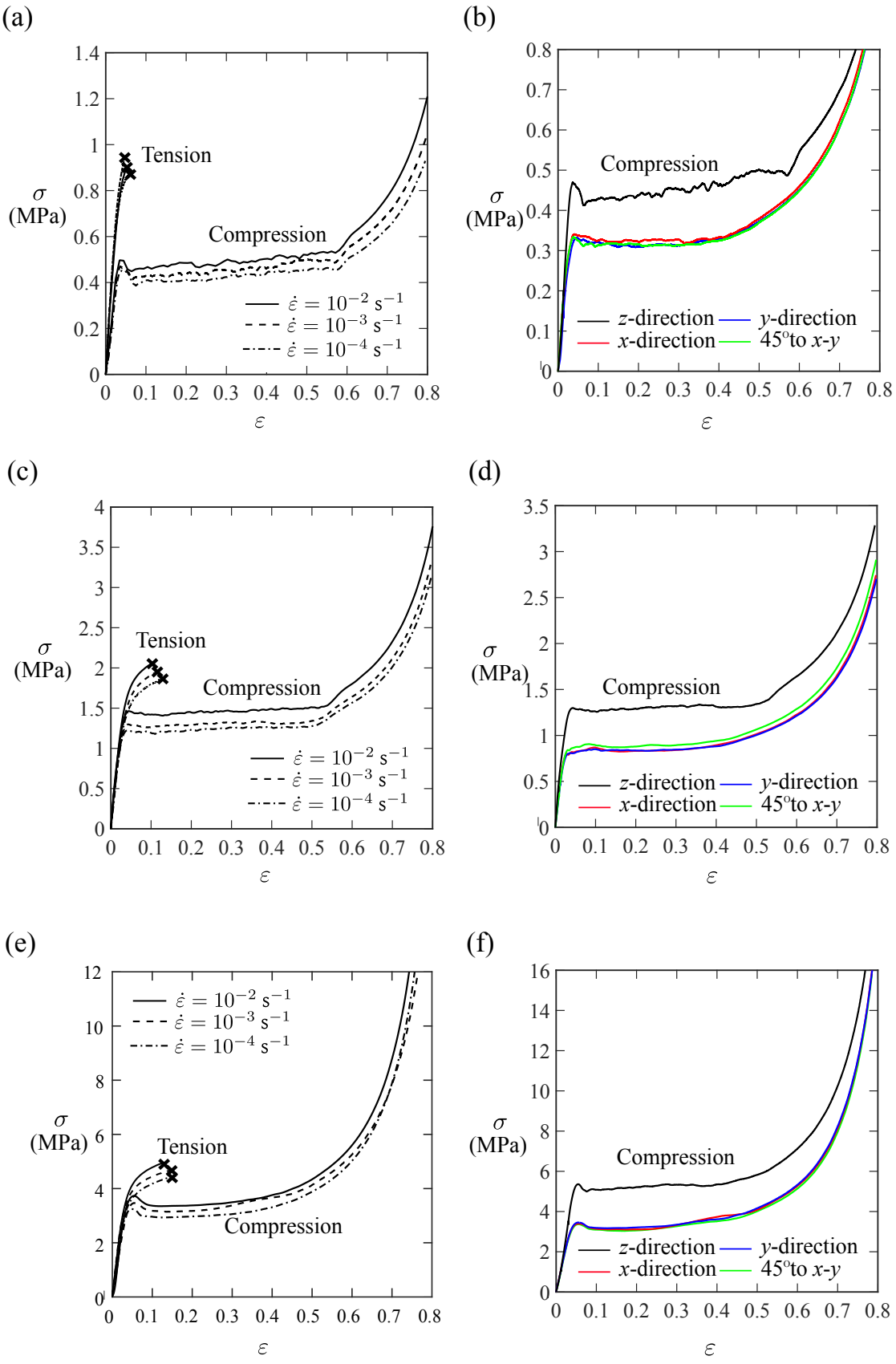

FIGURE 3.5: Comparison of nominal compressive and tensile stress strain responses under varying strain rates for H35, H80, H200 in (a), (c), (e) respectively. Comparison of nominal compressive stress strain responses under varying loading direction for H35, H80, H200 in (b), (d), (f) respectively.

We show the effect of loading direction on the stress versus strain responses in compression for the full range of foams (H35, H80, H200) in Figures 3.5 (b), (d), and (f) respectively. Compression tests in the in-plane (x and y) directions of the foam showed significantly lower yield and plateau strengths than the tests in the out-of-plane z-direction, although the stiffness is relatively unchanged. Variation between in-plane properties was minimal indicating that the material is transversely isotropic. The same trends exist in the tension samples (results not shown), however, the tensile behaviour in the z-direction could not be obtained due to geometrical limitations. We attribute the transverse isotropic behaviour to inherent alignment of the cell due to gravitational effects during the manufacturing process. The cells are longer in the z-direction in comparison to the x-y-directions giving higher yield and plateau strengths.

3.3.1.2 Tension compression asymmetry and ductility

Figures 3.5 (a), (c), (e) show the typical asymmetrical behaviour, where it is very ductile (and does not fail) in compression, whilst it is very brittle in tension. Despite this, it is evident that the foams yield at a higher strength in tension than that of compression. This behaviour may be due to the fact that a foam is bending dominated in compression whilst bending and then stretching dominated in tension. The struts buckle and collapse in compression via the formation of shear bands, whilst in tension they fail via tearing of the cell struts and walls. We observe that the disparity between the failure strength in tension and the peak compressive yield strength decreases as the relative density increases for these foams. The H35 tensile/compressive strength ratio is approximately 2 whilst in the case of H200 a ratio of approximately 1.25 is observed. It is hypothesised that this is a result of the change in the aspect ratio of the cells due to the change in relative density. The cell shape of the higher density is more homogeneous than the lower density H35.

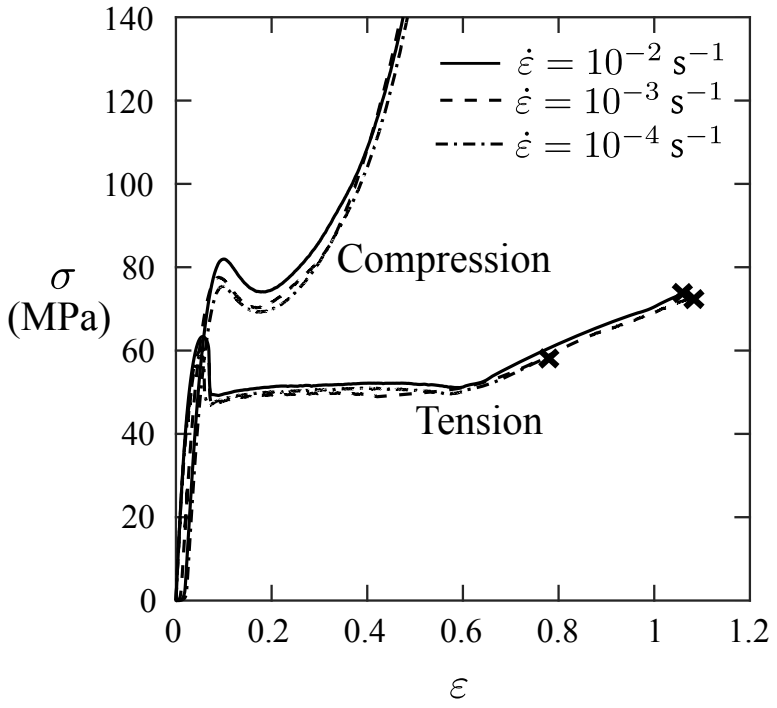

FIGURE 3.6: Nominal stress versus strain for polycarbonate in compression and tension.

3.3.2 Polycarbonate properties

The nominal stress versus strain curves for polycarbonate in both compression and tension, for three different strain rates, are shown in Figure 3.6. There was negligible scatter between the three repeated tests in all compression and tension experiments. In tension we measure a Young's modulus of $E = 2200$MPa and observe that the once the elastic limit is exceeded the stress reaches a local maximum in stress at ≈ 60MPa. We then observe a sharp drop in stress at this point which coincides with the formation of a neck within the gauge length. The stress stabilises at a stress of $\sigma \approx 52$MPa. Subsequently we observe a plateau in the stress as the neck stabilises and propagates along the gauge length. This phenomenon is associated with the alignment of the molecular chains in the polymer. At a nominal strain of 0.6, the plateau region ends and we observe a stiffening of the response. At this point all of the polymer chains have aligned and eventually break under increasing strain with a final nominal strain of $\varepsilon \approx 1.1$.

In compression, we observe that once the elastic limit is exceeded, a small amount of softening occurs followed by significant hardening. We note that the yield stress of

polycarbonate in compression is greater than that in tension ($\sigma_y = 82$, approximately 1.3 times greater).

3.4 Conclusion

This section has outlined the successful characterisation of the basic tensile and compressive properties of a range of Divinycell PVC foams as well as a single grade of solid polcarbonate. It is clear that one must be mindful of strain rate and the direction of loading in any further experiments. Further studies will involve the fracture and bending of the foam in the in-plane directions and these properties must be considered. In addition to this, a clear difference between the yield behaviour in tension, versus the yield behaviour in compression. This fact typifies the asymmetrical behaviour of a foam and will be needed in further studies, such as that of the analytical behaviour of a beam in bending.

Part I

The influence of residual stress on the mechanical response of sandwich beams

Chapter 4

The influence of residual stress on the collapse of sandwich beams with elastic face sheets

Summary

The influence of residual stress on the elastic indentation mode of sandwich beam collapse for both simply supported and clamped boundary conditions is first investigated analytically and then via finite element simulations. An indentation model is presented in which an elastic beam, supported by a rigid plastic foundation, is loaded by a cylindrical roller. In addition to bending loads, the elastic beam undergoes axial loading due to the action of a residual stress (compressive or tensile) as well as a compressive force due to the global bending of the entire sandwich structure. The analytical model quantifies the change in collapse load as a function of a non-dimensional residual stress, independent of sandwich beam geometry. Subsequently, a collapse mechanism map is formed for a sandwich beam system comprising GFRP facesheets, and a PVC foam core, which incorporates contours of the change in collapse load as a function of sandwich beam geometry and applied residual stress. The influence of residual stress on the

boundaries of the collapse map is explored using the analytical model. The relationship between residual stress and collapse load is validated for both a simply supported sandwich beam and clamped beams loaded by a cylindrical roller. A marked increase or decrease in collapse load is shown to occur when a tensile or compressive residual stress is present in a simply supported beam respectively. A clamped beam shows the same behaviour when a compressive residual stress is present. However, when a tensile residual stress is present the response becomes dominated by membrane stretching and no increase in collapse load occurs.

4.1 Introduction

Sandwich panels are used extensively as structural elements in the aerospace and automotive industries. Consequently, their mechanical behaviour, and in particular their collapse mechanisms under flexural loading have been widely studied. As described in Chapter 2, sandwich panels collapse via competing mechanisms (face yield, core shear, or indentation) which depends upon their constituent properties as well as geometry. Sandwich structures are frequently subjected to concentrated loads resulting in denting, or indentation, and the theme of this chapter is this indentation mode of collapse and how it is influenced by the presence of residual stress.

In general, residual stress exists in all materials on some level and to some extent which may have positive and/or negative effects on the structural behaviour. Residual stress is multi-scale and can exist at the micro-scale in fibre reinforced materials which may cause cracking or debonding of fibres from the matrix material. It is a deleterious effect in this case. The development of residual stress may also occur at a macro-scale via asymmetrical cooling across a component depth such as PMMA during the casting process, for example. This can lead to warped and defective components. In contrast, we can observe positive effects from residual stress. Within the field of civil engineering, a cast concrete component for a bridge or building exhibits elastic brittle behaviour in tension. To overcome this issue, steel reinforcing members are added to concrete during the casting process. This serves to strengthen the structure in tension, under bending.

If further strength is required, then a residual stress is added to the structure via pre-stressing or post-stressing. This is achieved by placing the steel members in tension during the casting process. Once the concrete has solidified, the tensile load on the steel members is released and is subsequently transferred to the concrete, placing it in a state of compression. This protects it from failure in tension.

The study presented in this chapter draws inspiration from the pre-stressing process in the field of civil engineering. The presence of residual stress has the potential to improve or adversely affect the collapse load; this is analysed in detail in this chapter. Residual stress may also influence the displacement to failure, and significantly alter the mode by which the sandwich beam attains initial yield or fails, and this is subsequently analysed in the next chapter, Chapter 5. Here, both face sheets are pre-stressed in tension, whilst the foam material is placed in a compressive state, akin to that of pre-stressed concrete. The faces and core behave in an interconnected manner when collapse occurs and this altered stress state may have a strong influence in changing these collapse states. A systematic analytical and numerical study has been carried out on a pre-stressed sandwich beam comprising an elastic brittle GFRP face sheet and PVC foam core with the aim of understanding the positive or negative effects under the action of a residual stress. This chapter aims to address the following research questions

1. Is it possible to quantify the change in the elastic indentation collapse due to the presence of residual stress?
2. Do the boundary conditions alter the influence of residual stress on the collapse load?
3. Are the boundaries of the collapse mode map sensitive to the presence of residual stress?

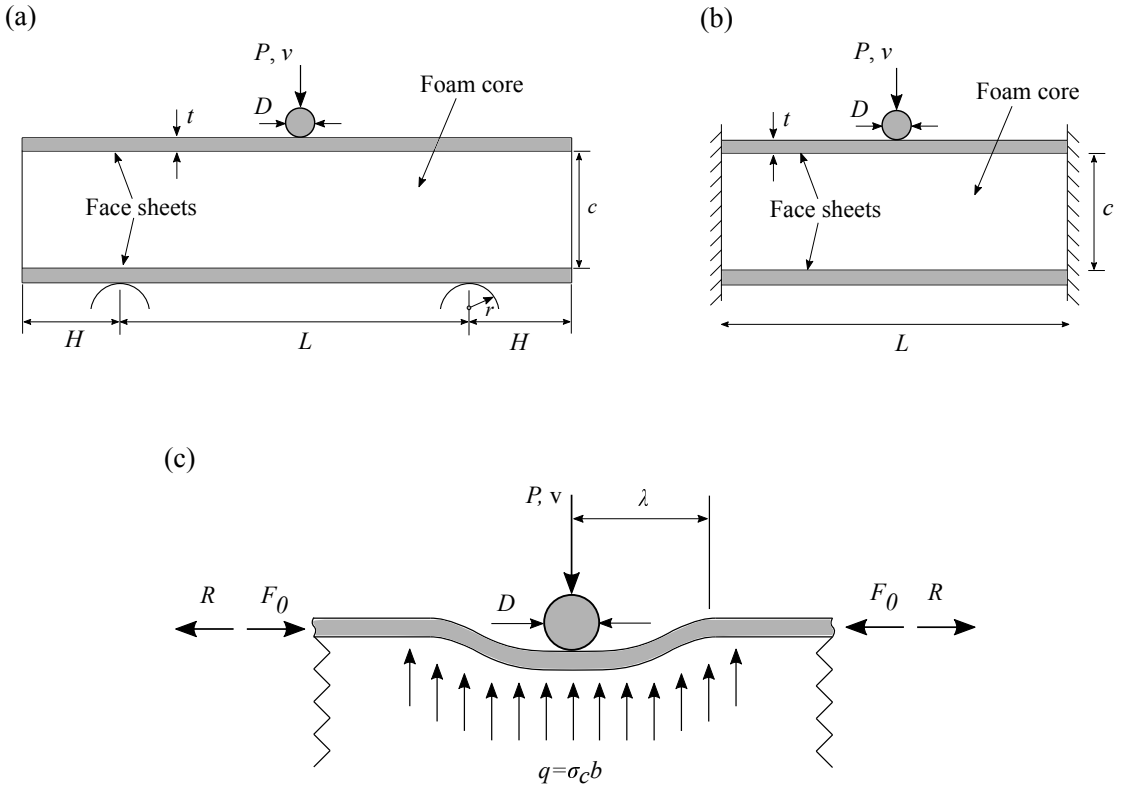

FIGURE 4.1: (a) Simply supported beam geometry (b) clamped beam geometry (c) schematic of top face sheet of the sandwich beam during the elastic indentation collapse mechanism with residual stress R and axial compressive load due to bending, F_0.

4.2 An analytical description of the influence of residual stress on the elastic face indentation collapse mode

4.2.1 A model for the influence of residual stress on the elastic face indentation collapse of a simply supported beam

Consider a simply supported sandwich beam in bending of depth, b, length, L, facesheet thickness, t, and core thickness, c, as shown in Figure 4.1(a). A clamped beam is dealt with later in the chapter and is shown in Figure 4.1(b). The beam behaves in a linear elastic manner under the applied point load P, resulting in a maximum bending moment at the centre of the beam of $PL/4$. This bending moment is in equilibrium with axial loads $\pm F_0$ in the face sheets, where

$$F_0 = \frac{PL}{4d} \tag{4.1}$$

and $d = t + c$. The core beneath the indenter yields at σ_{cy}, and the upper face sheet bends in an elastic manner with a wavelength λ. This mechanism is outlined in Figure 4.1(c). Steeves and Fleck (2004b) identified this mode as the elastic face indentation collapse mode. Subsequently, we will idealise the problem by considering the top face sheet as an elastic beam sitting on a core idealised as a rigid perfectly-plastic foundation. Further, assume that the upper face sheet is subjected to a net axial load F which comprises the residual tension (or compression), R, and the compressive load, F_0

$$F = F_0 - R \tag{4.2}$$

where $R = \sigma_R t$ in terms of a residual stress σ_R, see Figure 4.1(c). If a differential beam element is considered then a moment M and shear force V are applied via a transverse load per unit length $q = \sigma_c b$, subsequently vertical force equilibrium is given as

$$q = \frac{dV}{dx} \tag{4.3}$$

and moment equilibrium as

$$F\frac{dv}{dx} + V = \frac{dM}{dx} \tag{4.4}$$

where $v(x)$ is the transverse deflection of the beam. We now invoke classical Euler beam theory

$$M = -E_f I_f \frac{d^2 v}{dx^2} \tag{4.5}$$

This results in the following governing differential equation

$$\frac{d^4v}{dx^4} + \frac{F}{E_f I_f}\frac{d^2v}{dx^2} = \frac{-q}{E_f I_f} \tag{4.6}$$

with solution

$$v(x) = A_1 cos(kx) + A_2 sin(kx) + A_3 x + A_4 - \frac{\sigma_{cy} b x^2}{2F} \tag{4.7}$$

The wave number k is defined as

$$k = \sqrt{\frac{F}{E_f I_f}} \tag{4.8}$$

The coefficients A_1, A_2, A_3, and A_4 are determined from the boundary conditions as follows

a) Symmetry gives

$$v'(x = 0) = 0 \tag{4.9}$$

b) The shear force on the mid-section of the beam equals $P/2$ at $x = 0$, giving

$$v'''(x = 0) = \frac{P}{2E_f I_f} \tag{4.10}$$

c) At the end of the indentation zone, the core is rigid. This gives

$$v(x = \lambda) = 0 \tag{4.11}$$

d) The slope at the end of the indented zone equals zero

$$v'(x=\lambda)=0 \tag{4.12}$$

e) The moment in the face sheet at the end of the indented zone equals zero since the bending moment is taken to be continuous

$$v''(x=\lambda)=0 \tag{4.13}$$

The coefficients A_1 to A_4 follow as

$$A_1=\frac{2d}{Lk\alpha}\left(\frac{1-cos\mu-\mu sin\mu}{sin\mu-\mu cos\mu}\right) \tag{4.14}$$

$$A_2=-\frac{2d}{Lk\alpha} \tag{4.15}$$

$$A_3=\frac{2d}{L\alpha} \tag{4.16}$$

$$A_4=\frac{2d}{Lk\alpha}\left(\frac{1-cos\mu-\mu sin\mu}{sin\mu-\mu cos\mu}\right)+\frac{d\mu^2}{Lk\alpha}\left(\frac{1+cos\mu}{sin\mu-\mu cos\mu}\right) \tag{4.17}$$

Here we define $\mu=k\lambda$ and α as

$$\alpha=\left(1-\frac{4Rd}{PL}\right) \tag{4.18}$$

The load P, mid span roller displacement $v(0)$, and wavelength λ can be given as a function of the parameters α and μ. First, we obtain an implicit expression for P, μ and α by using boundary condition (d), expressed as Equation 4.12; this is given as

$$\alpha^{1/3}P=\left[\frac{4dE_f{\sigma_{cy}}^2}{3L}\left(\frac{sin\mu-\mu cos\mu}{1-cos\mu}\right)^2\right]^{1/3} \tag{4.19}$$

Equations 4.1, 4.8, and 4.19 can be used to obtain an expression for the wavelength λ

$$\alpha^{1/3}\lambda = t\mu\left[\frac{dE_f}{6L{\sigma_{cy}}^2}\left(\frac{1-cos\mu}{sin\mu-\mu cos\mu}\right)\right]^{1/3} \tag{4.20}$$

The deflection $v(x=0)$ may also be found as $v(0)=A_1+A_4$ such that

$$v(0) = \frac{4d}{Lk\alpha}\left(\frac{1-cos\mu-\mu sin\mu}{sin\mu-\mu cos\mu}\right)+\frac{d\mu^2}{Lk\alpha}\left(\frac{1+cos\mu}{sin\mu-\mu cos\mu}\right) \tag{4.21}$$

We recognise that $v(0)$ increases monotonically from zero as μ increases from zero. The parameter μ reaches a value of π at $P=P_{R,max}$ where

$$\alpha^{1/3}P_{R,max} = bt\left(\frac{\pi^2 dE_f{\sigma_c}^2}{3L}\right)^{1/3} \tag{4.22}$$

via Equation 4.19. To account for the residual stress parameter α as defined in Equation 4.18, we assume that it is fixed at $P_{R,max}$ implying a value of R, in turn giving an explicit solution for the maximum load. If no residual stress is present in the face sheet, then $\alpha=1$, and the above analysis returns the Steeves and Fleck (2004b) solution for elastic face indentation of a simply supported beam, $P_{0,max}$

$$P_{0,max} = bt\left(\frac{\pi^2 dE_f{\sigma_c}^2}{3L}\right)^{1/3} \tag{4.23}$$

4.2.2 A model for the influence of residual stress on the elastic face indentation collapse of a clamped beam

If we now consider a clamped sandwich beam in bending we may use the above analysis to produce a load versus displacement relationship and collapse load for such a beam. The geometry for a clamped beam is shown in Figure4.1(b). The sandwich beam is under the action of a point load, P, and clamped boundary conditions at both ends. This

gives a linear elastic response with a maximum bending moment at the centre of the beam, resulting in a maximum axial load F_0 in the face sheet

$$F_0 = \frac{PL}{8d} \tag{4.24}$$

Local to the indenter we observe the same behaviour as seen in the simply supported case and thus we use the same formulation of the governing differential equation and its solution given in Equations 4.6 and 4.7 respectively. The new solution takes the form

$$v(x) = B_1 cos(kx) + B_2 sin(kx) + B_3 x + B_4 - \frac{\sigma_c b x^2}{2F} \tag{4.25}$$

Note that k, μ, λ maintain their definitions from Section 4.2.1. We now apply boundary conditions (a)-(e) as before, however we use the new definition of the maximum global bending moment from Equation 4.24 to obtain the coefficients B_1 to B_4.

$$B_1 = \frac{4d}{Lk\beta}\left(\frac{1 - cos\mu - \mu sin\mu}{sin\mu - \mu cos\mu}\right) \tag{4.26}$$

$$B_2 = -\frac{4d}{Lk\beta} \tag{4.27}$$

$$B_3 = \frac{4d}{L\beta} \tag{4.28}$$

$$B_4 = \frac{4d}{Lk\beta}\left(\frac{1 - cos\mu - \mu sin\mu}{sin\mu - \mu cos\mu}\right) + \frac{d\mu^2}{Lk\alpha}\left(\frac{1 + cos\mu}{sin\mu - \mu cos\mu}\right) \tag{4.29}$$

where the coefficient β is given as

$$\beta = \left(1 - \frac{8Rd}{PL}\right) \tag{4.30}$$

The load P, mid span roller displacement $v(0)$, and wavelength λ can be given as a function of the fixed parameter β and variable parameter μ and are all definied as follows. Boundary condition (d), allows us to relate the load P and parameters μ and β. We obtain the following implicit expression

$$\beta^{1/3}P = \left[\frac{8dE_f{\sigma_c}^2}{3L}\left(\frac{sin\mu - \mu cos\mu}{1-cos\mu}\right)^2\right]^{1/3} \tag{4.31}$$

As before, we subsequently obtain an expression for the wavelength λ

$$\beta^{1/3}\lambda = t\mu\left[\frac{dE_f}{3L{\sigma_c}^2}\left(\frac{1-cos\mu}{sin\mu - \mu cos\mu}\right)\right]^{1/3} \tag{4.32}$$

$v(x=0)$ may also be found as $v(0) = B_1 + B_4$ for a range of values of μ

$$v(0) = \frac{8d}{Lk\beta}\left(\frac{1-cos\mu - \mu sin\mu}{sin\mu - \mu cos\mu}\right) + \frac{2d\mu^2}{Lk\beta}\left(\frac{1+cos\mu}{sin\mu - \mu cos\mu}\right) \tag{4.33}$$

We now use the same argument as before and recognise that $v(0)$ increases monotonically from zero as μ increases from zero. The parameter μ reaches a value of π at $P_{R,max}$. The load P thus attains a maximum P_{max} as follows

$$\beta^{1/3}P_{R,max} = bt\left(\frac{2\pi^2 dE_f{\sigma_c}^2}{3L}\right)^{1/3} \tag{4.34}$$

To account for the parameter β, we assume that it is fixed at $P_{R,max}$ implying a value of R, in turn giving an explicit solution for the maximum load. If no residual stress is present in the face sheet, then $\beta = 1$, and the above analysis returns the Tagarielli et al. (2004) solution for elastic face indentation of a clamped beam, $P_{0c,max}$

$$P_{0,max} = bt\left(\frac{2\pi^2 dE_f{\sigma_c}^2}{3L}\right)^{1/3} \tag{4.35}$$

4.2.3 The predicted influence of residual stress on the collapse load for a sandwich beam in bending

Sections 4.2.1 and 4.2.2 outlined the peak collapse load, and load versus displacement response of a sandwich beam in bending subjected to additional axial loads in the face

sheets which were driven by the coefficients α and β. We see from Equations 4.22 and 4.34 that in general terms, we can represent the increase in collapse load as follows

$$\bar{P} = \frac{P_{R,max}}{P_{0,max}} = \frac{1}{n^{1/3}} \tag{4.36}$$

where $n = \alpha$ or β. We define $\bar{R}$ as

$$\bar{R} = \frac{Rd}{P_{0,max}L} \tag{4.37}$$

If we now take Equation 4.36, insert either α or β and rearrange, we obtain

$$m\bar{R} = \bar{P} - \frac{1}{\bar{P}^2} \tag{4.38}$$

where $m = 4$ or 8 for the simply supported or full clamped case, respectively.

Equation 4.38 is plotted for both cases in Figure 4.2. In broad terms, we observe that a significant increase in collapse load is predicted for a sandwich beam with residual tension, regardless of the applied boundary conditions. A clamped beam with residual tension in the upper face sheet is expected to produce an increase in collapse load which is significantly greater than that of a simply supported case for a given $\bar{R}$, as $\bar{R}$ increases. Validation via finite element methods is provided in Section 4.5.

4.2.4 A note on the influence of residual stress on other collapse modes

This chapter deals with the influence of residual stress on the elastic indentation collapse mode only. We neglect the influence of residual stress on the face yield/microbuckling collapse mode for the following reasons. This collapse mode concerns the influence of the compressive or tensile strength of the chosen face sheet. Here we are concerned only with an elastic face sheet of a theoretical infinite strength and this assumption

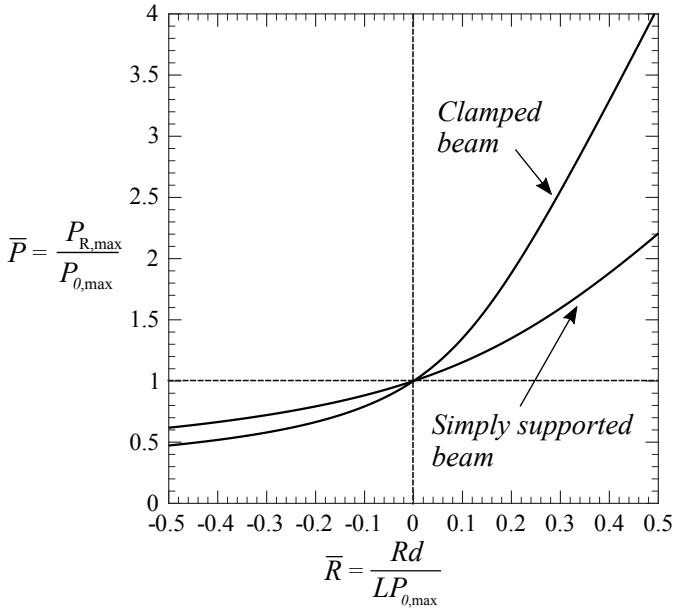

FIGURE 4.2: Influence of residual stress on the peak load of a sandwich specimen in the elastic face indentation mode.

gives scope to explore the elastic indentation collapse mode more thoroughly. The influence of residual stress on the face yield collapse mode is quantified in Chapter 5 with regards to interaction with the plastic indentation collapse mode. In order to quantify its interaction with the elastic indentation collapse mode, further study will be required.

We also neglect to account for the influence of residual stress on the core shear collapse mode and its interaction with the elastic indentation mode. Residual stress within the core of a sandwich beam can cause a significant reduction in the collapse load due to earlier yielding of the core during bending. The reader is directed to Section 5.2.3 where we quantify such knockdowns in performance. Given that the elastic indentation mechanism involves yielding of the core, we find that despite the core yielding, the beam will still approach an elastic indentation collapse. Thus it is clear that there is a potential for significant interaction between these modes. Again, due to this potentially complex behaviour we choose to isolate the elastic indentation mode by selecting geometries that fit within the elastic indentation region, at a significant distance from the core shear region on the collapse mode map. This proves to be a useful approach given the successful validation of the models proposed in previous sections. This will be shown in Section 4.5.

4.3 Collapse mode maps for GFRP facesheets and PVC foam core

The remaining sections of this chapter outline a case study in which we choose specific materials to form a sandwich beam system which allows us to probe the implications of the analytical models detailed in the previous section.

4.3.1 Material selection and creation of a collapse mode map

Fibre reinforced composite materials are frequently used as face sheet materials in a variety of industrial applications. We choose an elastic brittle GFRP face sheet and polymer foam core so as to align with these practices. Steeves and Fleck (2004a) carried out material characterisation on a Hexcel Fibredux 7781-914G woven glass-epoxy composite and it is the material properties from their study that we employ here. The measured material properties of the GFRP from their studies were; an elastic modulus $E_f = 30GPa$ and an average measured compressive failure strength $\sigma_f = 350MPa$. The measured in-plane properties of the H200 core were measured as described in Chapter 3. The in-plane elastic modulus of H200 PVC foam was measured as $E_c = 125$ MPa and the compressive strength is $\sigma_{cy} = 3.2$ MPa.

We do not carry out any material characterisation on GFRP or any prestressing or bending experiments on these sandwich panels. The material properties of GFRP were well characterised by Steeves and Fleck (2004a), who also used H200 core in their sandwich beams.

Using these properties, we can thus form a collapse mode map based on the competing modes of collapse (elastic indentation, core shear and face microbuckling) as outlined in Chapter 2. The collapse map is formed by choosing a square matrix within a range of reasonable normalised geometry variables: $\bar{t} = t/c$ and $\bar{c} = c/L$. The collapse load for all potential modes was calculated, i.e. Equations 4.23, 2.15, and 2.10, at each matrix point and the minimum and thus operative mode was found. The collapse mode map for the combination of GFRP face sheets and H200 PVC core in simply supported

and clamped conditions is shown in Figures 4.3 and 4.4 respectively. We note that the elastic indentation and face microbuckling regimes are greater in area in the case of simply supported boundary conditions.

It is instructive to write the normalised residual stress $\bar{R}$ and $\bar{P}$ as a function of $\bar{t}$ and $\bar{c}$, and the various material properties. Subsequently we can plot contours of $\bar{P}$ on the collapse load map for any assumed value of $\bar{R}$ allowing us to view and select the range of geometries available for a given combination of $\bar{R}$ and $\bar{P}$. We combine Equation 4.37 with Equation 4.23, and obtain

$$\bar{R} = \frac{R}{t}\left(\frac{d}{L}\right)^{2/3}\left(\frac{3}{\pi^2}\right)^{1/3}\left(\frac{1}{E_f\sigma_{cy}^2}\right)^{2/3} \tag{4.39}$$

Note that for the sake of brevity, we choose to use the simply supported conditions for this analysis. The following process can be repeated for clamped conditions. If we choose R such that it is limited by the yield strength of the foam i.e. $R_c = c\sigma_{cy}/2$, Equation 4.39 becomes

$$\bar{R}_c = \frac{\bar{c}^{2/3}}{2\bar{t}}(1+\bar{t})^{2/3}\left(\frac{3}{\pi^2}\right)^{1/3}\left(\frac{\sigma_{cy}}{E_f}\right)^{1/3} \tag{4.40}$$

and if we choose R such that it is now limited by the strength of the face sheet i.e. $R_f = \sigma_{fy}t$, then Equation 4.39 becomes

$$\bar{R}_f = \bar{c}^{2/3}(1+\bar{t})^{2/3}\left(\frac{3}{\pi^2}\right)^{1/3}\left(\frac{\sigma_{fy}}{E_f^{1/3}\sigma_{cy}^{2/3}}\right) \tag{4.41}$$

We can then quantify a transition between these Equations 4.40 and 4.41 using the yield-/failure strength of the facesheet and foam, σ_{fy}, and σ_{cy} in combination with Equation 4.44

$$\bar{t}_{trans} = \frac{\sigma_{cy}}{2\sigma_{fy}} \tag{4.42}$$

Now we can relate $\bar{t}$ and $\bar{c}$ to $\bar{P}$ via Equation 4.38 and plot contours of $\bar{P}$ for $\bar{R} = \{\pm 0.1, \pm 0.2, \pm 0.3\}$ on the collapse mode map as seen in Figures 4.3 and 4.4 for both simply supported and clamped beams respectively. We note that the transition between facesheet and foam governed residual stress for a combination of GFRP and H200 PVC foam is very small ($\bar{t}_{trans} = 0.0046$) and we conclude that, for this particular combination of materials, it is only necessary to include the foam governed contours on the collapse mode map in the case of simply supported conditions, i.e. Equation 4.40. Face sheet governed contours are included in the case of the clamped beam as shown in Figure 4.4.

4.3.2 The influence of residual stress on the collapse mode map

The collapse mode map for a GFRP facesheet and H200 PVC foam with $-0.4 \leq \bar{R} \leq 0.4$ is shown in Figures 4.4 and 4.4 for a simply supported and clamped beam respectively. We observe that once $\bar{R} > 0$ the elastic indentation region shrinks due to the raised collapse load for elastic indentation. The converse is true if $\bar{R} < 0$.

We observe that as residual stress increases, the area of possible elastic indentation collapse shrinks, whilst the contours of $\bar{P}$ also move accordingly and stay within this area. We can conclude that the presence of residual stress and its associated collapse mode contours and trajectory of boundaries give significant insight into the areas of the collapse load map that facilitate increased energy absorption of sandwich panels in bending.

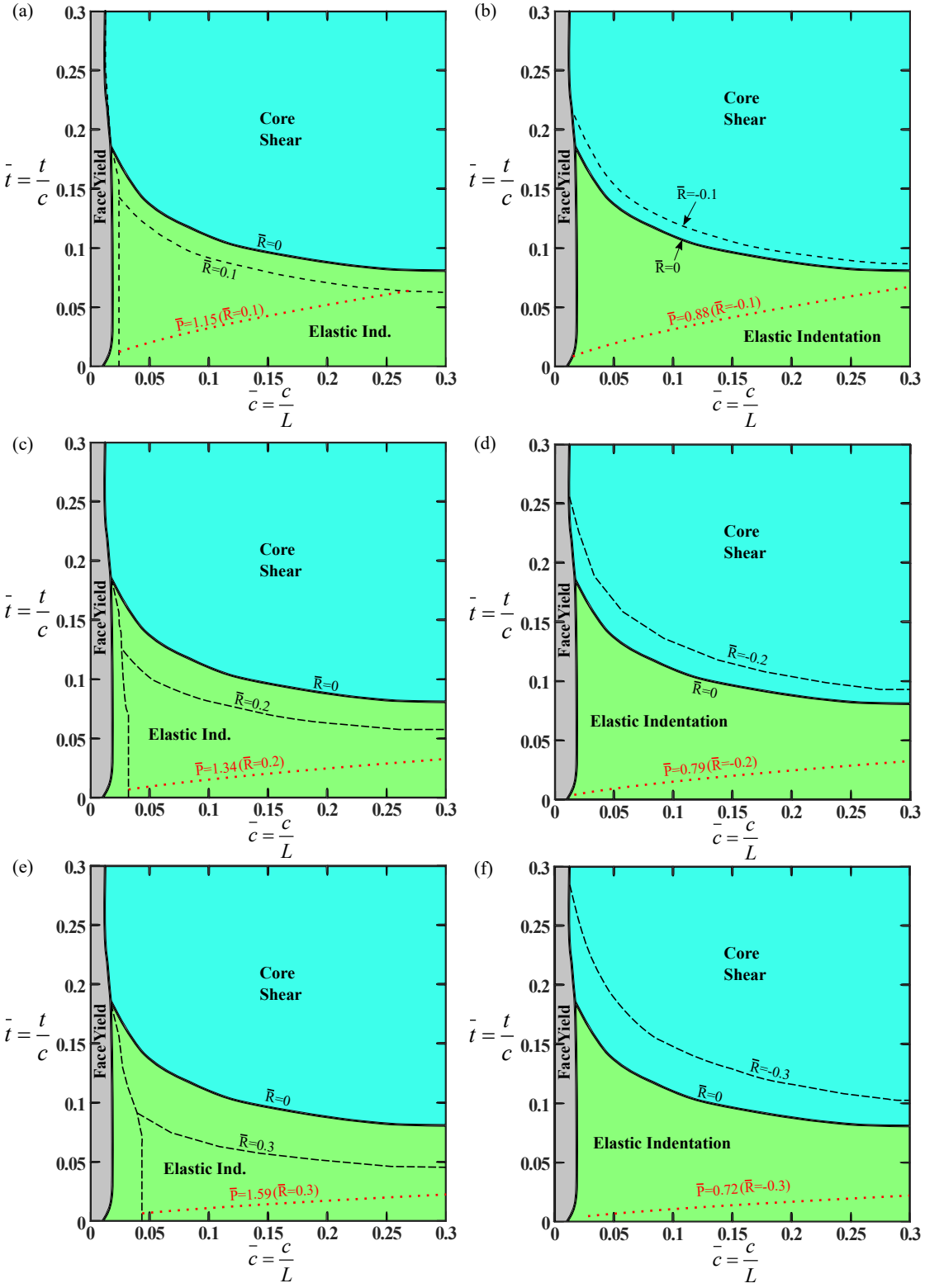

FIGURE 4.3: The collapse mode map for a simply supported beam with GFRP face sheets and H200 PVC foam core. The change in map boundaries due to the presence of residual stress is shown for (a)-(b) $\bar{R} = \pm 0.1$ (c)-(d) $\bar{R} = \pm 0.2$ and (e)-(f) $\bar{R} = \pm 0.3$. The corresponding contour for $\bar{P}$ is shown in each case.

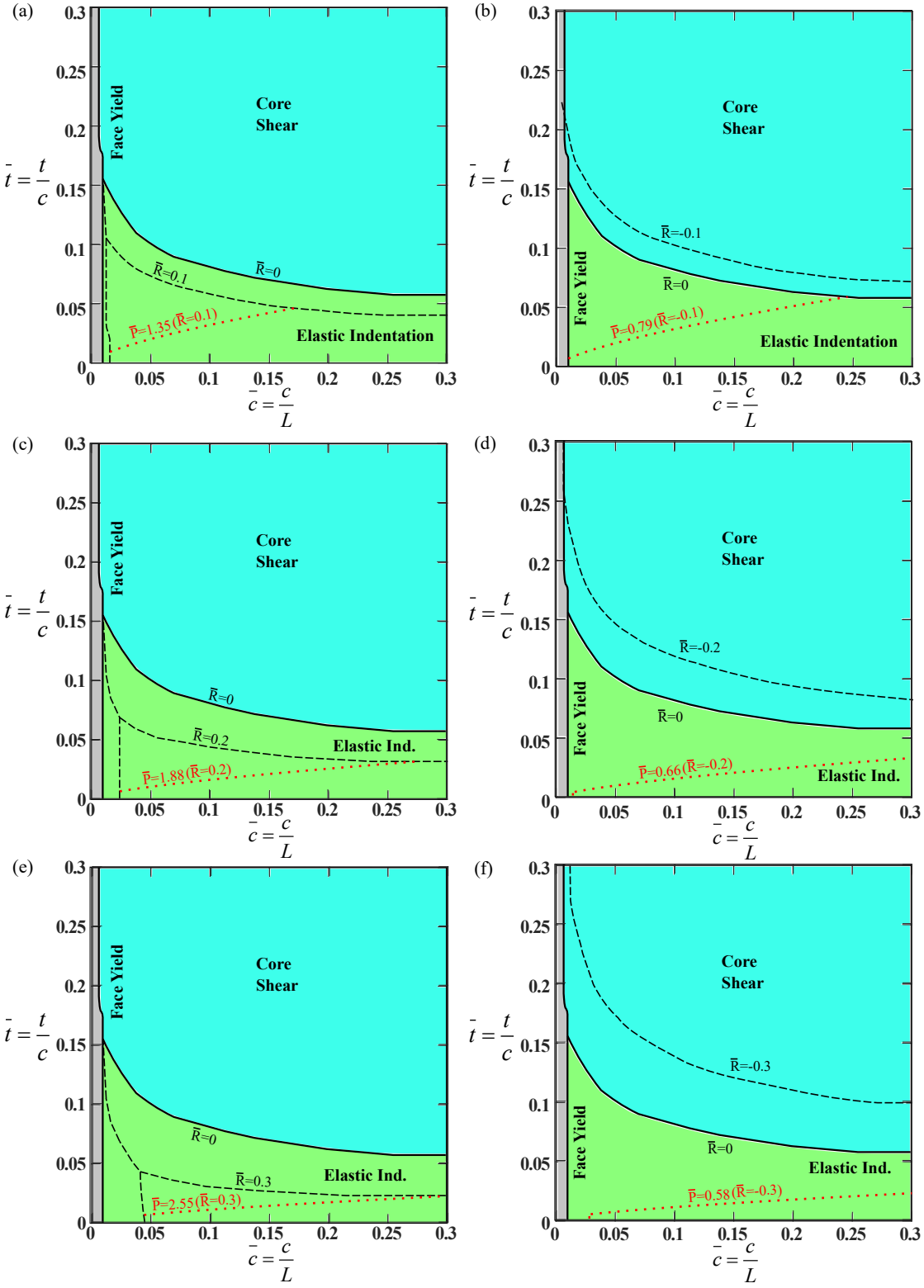

FIGURE 4.4: The collapse mode map for a clamped beam with GFRP face sheets and H200 PVC foam core. The change in map boundaries due to the presence of residual stress is shown for (a)-(b) $\bar{R} = \pm 0.1$ (c)-(d) $\bar{R} = \pm 0.2$ and (e)-(f) $\bar{R} = \pm 0.3$. The corresponding contour for $\bar{P}$ is shown in each case.

4.4 Finite element methods for sandwich beams in bending under the action of residual stress

4.4.1 Geometry and material models

In the remaining sections of this chapter we outline numerical simulations that validate the analytical model provided in Section 4.2 and provide further insight into the behaviour of sandwich beams under bending subjected to residual stress. We will now outline the finite element methods used. Quasi-static finite element simulations were performed using the finite element analysis package ABAQUS/Explicit (v6.14). Figure 4.1 shows the geometry and loading for the three-point bending of the sandwich beams. The beam is supported between the span by rigid cylindrical rollers of radius $r = 9.5mm$, and is indented by a circular roller of diameter $D = 1mm$. The contact between rollers, supports and the beam surfaces is assumed to be frictionless. The mesh comprises of 20 four-noded quadrilateral plane strain elements (designated CPE4R in ABAQUS/Explicit) through the thickness of the facesheet and about 100 elements through the core thickness with suitable additional refinement at the indenter and at the support rollers. Perfect adhesion was assumed between the face sheets and foam core. A symmetric half model was employed in the FE study with the bottom edge of the core fixed and the roller prescribed with a vertical downward velocity. The punch velocity in the FE calculations was chosen to be sufficiently small to ensure negligible inertial effects in order to simulate quasi-static conditions. Figure 4.5 shows the finite element model as described above and also shows the presence of residual stress, for which the numerical methodology will be discussed in Section 4.4.2.

The face sheet was a glass fibre reinforced plastic (GFRP) modelled as an elastic solid with an elastic modulus of $E_f = 30$ GPa and Poisson's ratio of $\nu_f = 0.3$, as mentioned previously. The PVC foam properties were specified with an elastic modulus $E_c = 125$ MPa and Poisson's ratio $\nu_c = 0.3$. The measured nominal stress versus strain response is given in Figure 4.6 (a). The post-yield behaviour of the foam was modelled using the crushable foam model in ABAQUS which allows for a dissimilar response of the

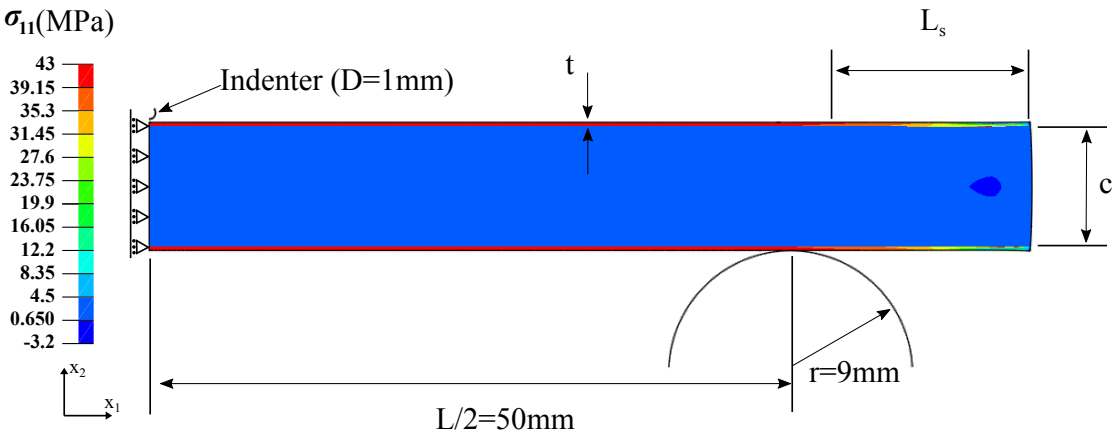

FIGURE 4.5: Residual stress state in the facesheets and core at the end of the pre-stressing step.

foam in tension and compression; a detailed description of the constitutive model is given in Appendix A. The assumed true uniaxial compressive response of the foam is plotted in Figure 4.6 (b); this curve is a smooth spline fit of the measured response in uniaxial compression (at a strain rate of $10^{-4}s^{-1}$) upon excluding the stress peak at the onset of yield. A perfectly-plastic response is assumed for foam under tension via a constant parameter k_2 as explained in Appendix A. For a choice of $k_2 = 2.2$, the uniaxial tensile yield strength from the FE simulation agrees with the measured uniaxial tensile strength (of 4.7 MPa) to within 3%, and this value is employed in all the FE simulations. Failure of GFRP and PVC was not included in the FE model. Rate sensitivity was also neglected for both GFRP and PVC.

4.4.2 FE prestressing procedure

The role of residual tensile stress in the facesheets on the collapse load of sandwich beams in simply supported and clamped bending was explored via a two-step FE analysis in ABAQUS. In the first step of the analysis, the facesheet is thermally loaded to a temperature T inducing a stress σ_{fR} in the facesheet of magnitude

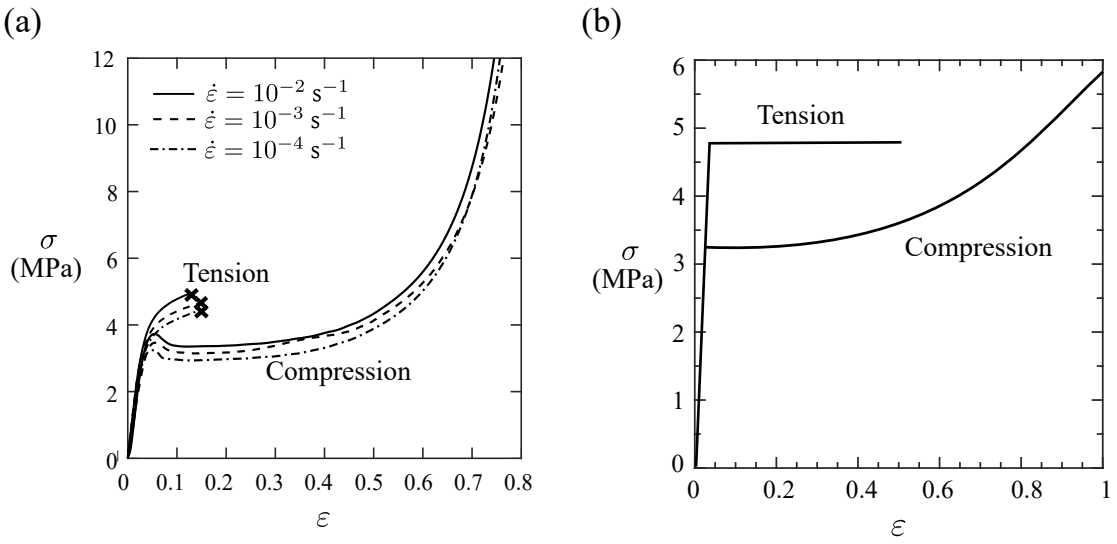

FIGURE 4.6: (a) Measured stress versus strain response for H200 PVC foam in both tension and compression (b) The input stress versus strain response for FE simulations.

$$\sigma_{fR} = \frac{E_f \alpha_T T}{1 + \frac{E_f}{E_c}\frac{2t}{c}} \tag{4.43}$$

Equilibrium dictates that there is a stress σ_{cR} in the core of magnitude

$$\sigma_{cR} = \frac{2t}{c}\sigma_{fR} \tag{4.44}$$

where α_T is the coefficient of linear thermal expansion of the facesheet. We present Equations 4.43 and 4.44 without proof, however this is addressed in Chapter 5. $\alpha_T T$ is required as an input to the finite element model in order to simulate the prestress in the face sheet. We calculate this by using Equation 4.43 and selecting a desired value of σ_{fR}. Note that the maximum tensile residual stress in the facesheet is limited by the core compressive strength, σ_{cy}, and the thickness of the facesheets, t and core c according to Equation 4.44, as $\sigma_{fR,max} = \sigma_{cy} c/2t$. Figure 4.5 shows an example of the stress state in the facesheets and core at the end of the thermal stressing step for a case where the facesheet contains a uniform tensile residual stress of $\sigma_{fR} = 43$ MPa exists in the facesheet and a uniform compressive residual stress 3.2 MPa exists in the core, both outside the shear lag region 20 mm. The shear lag region is estimated as $L_s = t\sigma_{Rf}/\tau_{cy}$ where τ_{cy} for H200 PVC foam is 2.7 MPa. In the case of the simply supported beam, the

length of the overhang, H, is chosen such that $H > L_s$ to ensure a uniform residual stress state within the span prior to bending. In the case of the clamped beam, the clamped conditions are applied following the thermal stressing procedure and it is assumed that $L/2 - \lambda >> L_s$ to ensure that the elastic collapse mechanism occurs within an area of uniform tensile residual stress in the face sheet.

In the second step of the analysis, a frictionless contact is established between the indenter, the supporting stationary rollers, and the beam. The indenter is then displaced vertically at a velocity small enough for the inertial effects to be negligible so as to simulate the quasi-static bending response of the sandwich beam.

4.5 Finite element analysis of the influence of residual stress on the collapse of sandwich beams

We now present a series of finite element simulations that probe the relationship between the relative increase in collapse load $\bar{P}$ and the applied, dimensionless residual stress $\bar{R}$ as described by Equation 4.38 and represented in Figure 4.2 for both simply supported and clamped boundary conditions. FE simulations explored $\bar{R}$ values of $-0.4 < \bar{R} < 0.4$ in intervals of $\bar{R} = 0.1$. The resulting value of $\bar{P}$ was measured and compared with the corresponding analytical value.

The following methodology was used to choose geometry and the subsequent levels of residual stress needed to validate the analytical model. First, a value of $\bar{R}$ was fixed, and then the geometry was chosen in accordance with Equation 4.40 where a value of $\bar{t}$ was calculated for a fixed value of $\bar{c} = 0.1$ in all simply supported and clamped cases. The value of σ_{Rf} was then calculated based on Equation 4.44, given $\bar{t}$ and σ_{cy}. Finally, the value of $\alpha_T T$ was calculated using Equation 4.43 and used as input to the GFRP material model in ABAQUS/Explicit. The FE procedure, as described in Section 4.4, was then carried out for beams that had (a) no residual stress, (b) a tensile residual stress in the face sheets and compressive residual stress in the core, and (c) a compressive

TABLE 4.1: Geometry and residual stress values for numerical simulations (SS=simply supported, C=clamped)

Mode	$\bar{R}$	$\bar{t}$	$\bar{c}$	t (mm)	c (mm)	L (mm)	σ_{fR} (MPa)	$\alpha_T T$
SS	± 0.1	0.034	0.1	0.34	10	100	± 43	0.025
SS	± 0.2	0.017	0.1	0.17	10	100	± 86.5	0.026
SS	± 0.3	0.012	0.1	0.12	10	100	± 133.63	0.028
SS	± 0.4	0.0086	0.1	0.086	10	100	± 172.94	0.029
C	± 0.1	0.025	0.1	0.25	10	100	± 64	0.027
C	± 0.2	0.0125	0.1	0.125	10	100	± 128	0.029
C	± 0.3	0.0083	0.1	0.083	10	100	± 192.71	0.03
C	± 0.4	0.0062	0.1	0.062	10	100	± 258.27	0.032

residual stress in the face sheets and tensile residual stress in the core. The geometry, and numerical details for each case is provided in Table 4.1.

4.5.1 Results and discussion

4.5.1.1 Simply supported beam results

The load versus indentation responses for the simply supported beams outlined in Table 4.1 with residual stress level in the range $-0.4 \leq \bar{R} \leq 0.4$ are shown in Figure 4.7. In broad terms, we observe excellent agreement between the FE simulations and the expected change in collapse load between the cases with and without residual stress. The analytical model described in Section 4.2 for a point load, implies that a peak load is reached and then softening occurs as indentation proceeds. In Figure 4.7 (a) we observe this behaviour for all three cases of $\bar{R} = 0, \pm 0.1$. However the remaining cases in Figure 4.7 (b)-(d) show a hardening response, or at least a plateau in the load versus displacement response. We can trace this behaviour to the following. As $\bar{R}$ increases we have chosen t such that it is decreasing. Thus the ratio t/D is also decreasing which promotes increasing contact area between the roller and facesheet. If we analyse the maximum principal stress along the length of the beam, midway through the facesheet thickness, we observe that the increased contact area promotes significant levels of membrane tension in the facesheet following initial collapse. We now consider an example where

where both types of collapse occur in tandem; the softening response of initial collapse is not suppressed but then geometric hardening occurs subsequently. Consider the case in Figure 4.7 (d) when $\bar{R} = -0.4$, we clearly see two stages of collapse: initial collapse with a softening response dictated by the analytical model (Section 4.2) and the presence of significant compressive maximum in-plane principal stresses (σ_1) in the face sheet (see Figure 4.8 (a)), which is marked as (A) ($v = 0.15$ mm) on the load versus displacement response. The softening reaches a minimum as the indentation proceeds and we then observe increased indenter contact and subsequent geometric hardening leading to tensile stretching which can be seen in Figure 4.8 (b) and indicated as point (B) ($v = 1$mm) on the load versus displacement response.

We note that the elastic indentation models of the present chapter do not incorporate the presence of a residual stress in the core (which is not the case for the finite element models). A residual stress in the core may cause earlier yielding of the foam and thus would directly affect the elastic bending and collapse of the beam. This may contribute to the more compliant finite element load versus displacement responses observed in Figure 4.7, however it is not immediately clear the extent to which it affects the collapse load given the agreement between finite element and analytical models.

Despite the significant geometrical effects, as described, we observe that the relationship between a prescribed residual stress $\bar{R}$ and a resulting change in collapse load $\bar{P}$ holds, as described by Equation 4.38. The sensitivity of collapse load to $\bar{R}$ is given in Figure 4.10 and the FE predictions broadly agree with theory. We note that this increase in $\bar{R}$ and subsequently the collapse load gives a significant increase in energy absorption, i.e. the area under the load versus displacement curve.

4.5.1.2 Clamped beam results

We present the load versus displacement responses in Figure 4.9 for the full range of clamped beams in bending as outlined in Table 4.1. Initial collapse is accurately predicted when $\bar{R} \leq 0$ and it is clear that the prediction for $\bar{R} > 0$ is not adequate. The FE results for $\bar{P}$ against prescribed $\bar{R}$ are given in Figure 4.10 and compared with the analytical response of 4.38 and confirm this conclusion. However, we observe a small rise

in collapse load when a tensile residual stress is present, comparable to that of the simply supported case. If we again analyse the maximum principal stress along the length of the beam, midway through the facesheet thickness, we see that face sheet bends and collapses elastically, but then gives way to membrane stretching (a) due to the clamped boundary conditions, (b) increasing contact area between the indenter and face sheet, and (c) the presence of a tensile residual stress. This inhibits the potential for increasing the collapse load of the sandwich panel in the presence of residual stress. In summary, rather than inhibiting the influence of the axial compressive force in the facesheet due to global bending (as in the simply supported case) we discover that the beam rapidly transitions into a stretching mode and the tensile residual stress contributes and adds to this behaviour. The converse is true in the case of the compressive residual stress, we see a delay in the membrane action and a reduction in expected collapse as predicted by the analytical model. We also note that energy absorption is significantly increased when a tensile residual stress is present after initial collapse; the deep indentation membrane response of a prestressed beam maintains a raised loading response relative to that of the case absent a residual stress.

4.6 Concluding remarks

This chapter focused on the effect of residual stress on the collapse behaviour of sandwich panels with elastic face sheets and foam core in flexure, under both simply supported and fully clamped configurations. An analytical description predicting the influence of an additional axial load in the face sheets was provided and indicated that significant changes in collapse load may occur as a result. The analytical model expands upon the models of both Steeves and Fleck (2004b) and Tagarielli et al. (2004). This model was then used to form a collapse load map for a sandwich beam system comprising GFRP (elastic) facesheets and PVC foam (rigid-perfectly-plastic) core in which the influence of residual stress was included. This new collapse mode map showed contours of the relative change in collapse load due to the presence of residual stress as well as the trajectory of the boundaries of this map under the influence of changing residual stress.

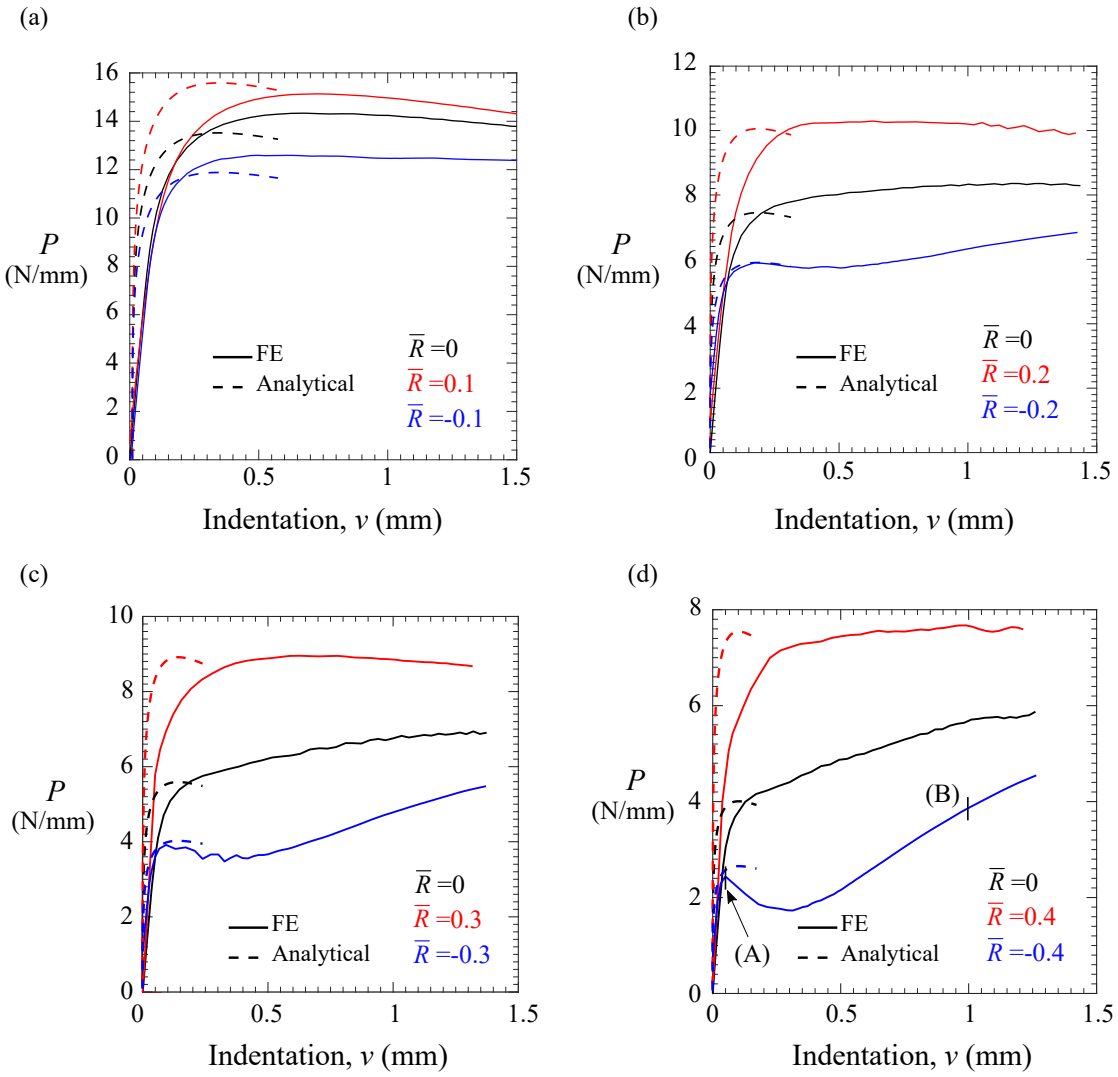

FIGURE 4.7: Load versus displacement for the four simply supported (SS) cases as outlined in Table 4.1. A reference sample, $\bar{R} = 0$ is included in each case.

A series of numerical simulations were carried out, which successfully validated the analytical model in the case of a simply supported beam for both tensile and compressive residual stresses in the face sheet. We observed significant potential for increase in collapse load and thus energy absorbed by a sandwich beam specimen. Conversely, it is clear that compressive residual stresses in the face sheet promote elastic indentation collapse and impacts negatively on the collapse load and energy absorption characteristics of a beam. The FE simulations also demonstrated the significant role that facesheet thickness/indenter size ratio plays on the energy absorption characteristics under deep indentation at depths greater than the facesheet thickness. We found that the numerical simulations for a clamped case validated the model where compressive residual stresses

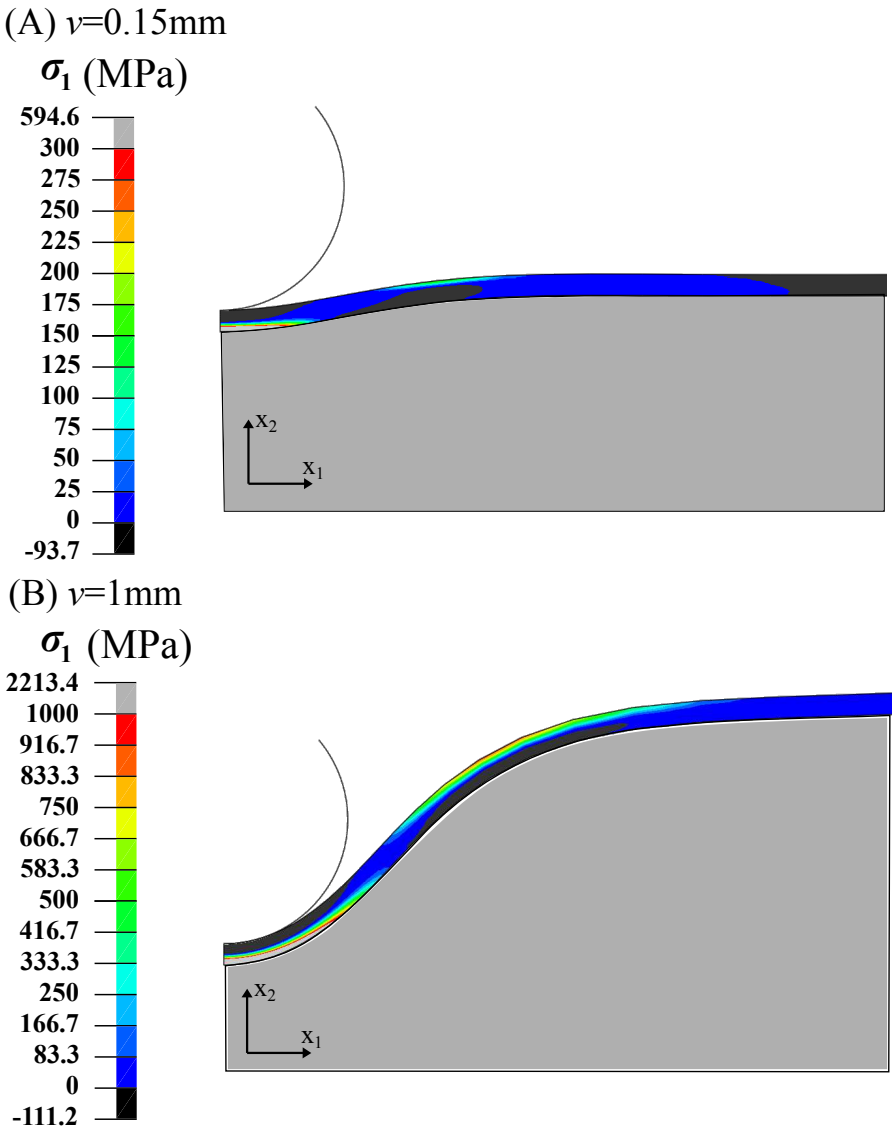

FIGURE 4.8: Finite element principal stress contours showing the increase in contact area as indentation proceeds from (A) $v = 0.15mm$ to (B) $v = 1mm$.

were concerned. However, we observed that tensile residual stresses did not produce the expected increase in collapse but instead promoted membrane stretching, and alternatively produced significant increases in energy absorbed as a result.

The elastic indentation models described in this chapter consider the bending of a face sheet which is supported by a uniformly distributed load. This distributed load is defined by the yield strength of the foam. If a residual stress is present in the core then earlier yielding of the foam will occur, which will directly influence the calculated collapse load. A model for the influence of residual stress on the first yield of the core is

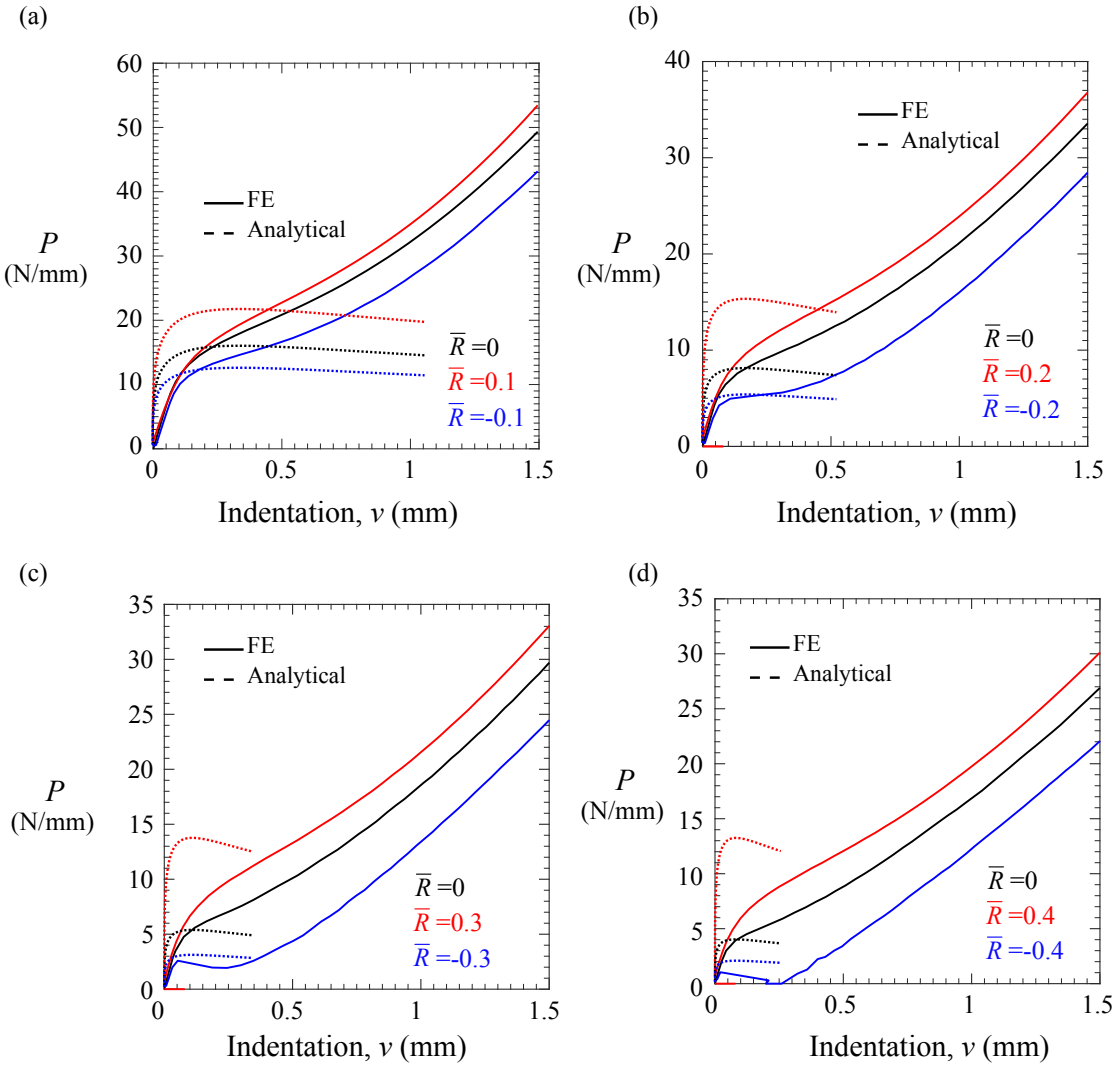

FIGURE 4.9: Load versus displacement for the four clamped (C) cases as outlined in Table 4.1. A reference sample, $\bar{R} = 0$ is included in each case.

presented in Section 5.2.3. If the core yield model was coupled with the elastic indentation models of the present chapter then a more accurate representation of the collapse behaviour would be obtained. The absence of such a calculation is the main limitation of the residual stress-elastic indentation collapse model, and provides a source of future work.

The study presented in this chapter has given insight into the behaviour of sandwich beams under the action of residual stress and has provided new potential design tools for the industrial end user of sandwich panels which allows greater energy absorption and collapse loads for the same weight. However, there are significant caveats that must be noted, and addressed in future studies. First, the present study has shown theoretical

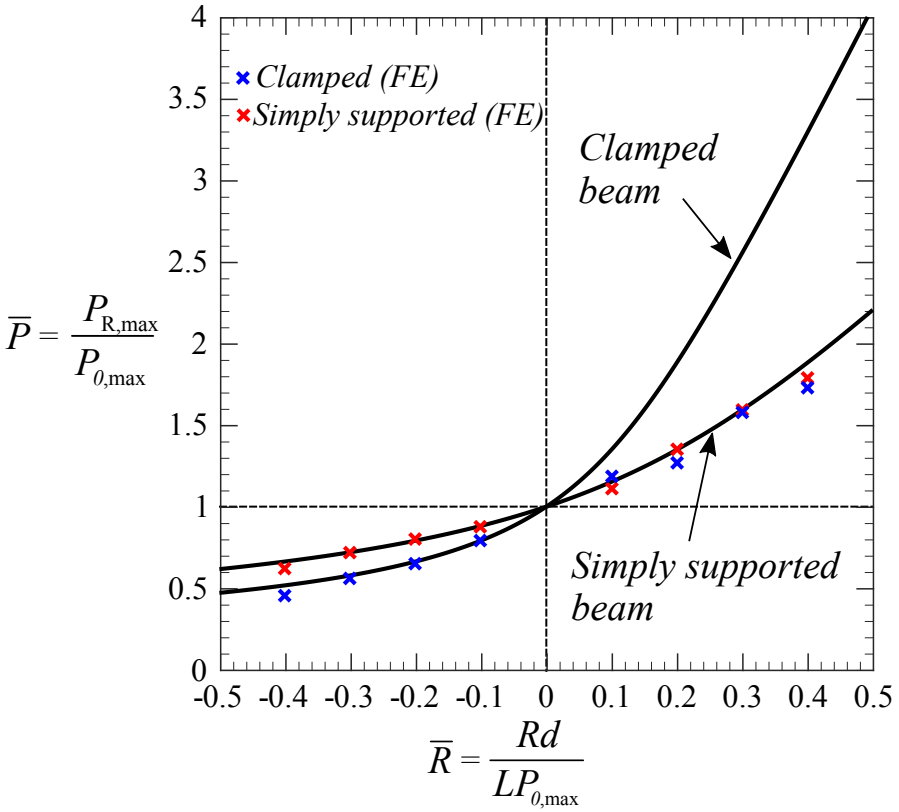

FIGURE 4.10: Finite element validation of Equation 4.38; the relationship defining the influence of residual stress on the elastic indentation collapse mode.

and numerical analysis only. Experiments are required in order to provide further insight into the behaviour described in preceding sections. Second, we have not provided any feasible, practical method for inducing residual stresses in a sandwich panel of such materials. This issue is discussed in more detail in the following chapter. The failure of the facesheet or foam has not been included in our analysis and this has the potential to limit the effectiveness of mechanisms described within this chapter.

Chapter 5

The influence of residual stress on the elastic limit and collapse of sandwich beams with elasto-plastic face sheets

Summary

The influence of residual stress on the elastic limit or first yield is initially explored by the formulation of analytical models and subsequently numerical models and experiments. We find that the elastic limit of a sandwich beam in bending is exceeded by the occurrence of three competing mechanisms: i) yield of the face sheets via global bending of the sandwich structure, ii) yield via indentation, i.e. local bending of the face sheet and simultaneous yield of the core adjacent to the indenter/point load, and iii) yield via shearing of the entire cross section of the core. Models are presented for all three mechanisms. These three mechanisms are closely related to the three collapse mechanisms (core shear, indentation, and face yield/microbuckling). We subsequently discuss the effect of residual stress on these collapse modes and postulate that there is indeed no effect of a residual stress field due to the fact that they are full plastic collapse modes and are formulated as upper bound calculations. The remainder of the chapter details an experimental implementation of residual stress in sandwich beams

that comprise elasto-plastic face sheets and core, and the resulting effects on the elastic limit and plastic collapse. The experimental sandwich beam comprises polycarbonate face sheets and H200 PVC foam core. The limitations of the experimental method are discussed whilst the analytical models are validated for a number of sandwich beams using experiment and finite element methods. The experiments also give insight into the post-collapse behaviour of the sandwich beams and the final failure mechanisms.

5.1 Introduction

The elastic behaviour of sandwich beams has been thoroughly documented, see for example the works of Plantema (1966), Allen (1969), and Zenkert (1995). Once the elastic limit is exceeded, failure will occur in the case of an elastic-brittle face sheet or the beam will proceed to full plastic collapse. Both Steeves and Fleck (2004a,b) and Tagarielli et al. (2004) have considered the indentation collapse of a sandwich beam when the face sheets remain elastic whilst the core yields. This form of collapse was considered in detail in Chapter 4. The plastic collapse of the sandwich panel, core and face sheets, occurs via three competing mechanisms (core shear, plastic indentation, and face yield) and has been covered by both Allen (1969) and Ashby et al. (2000) in which they employ upper bound models to describe these collapse behaviours. There is a noteworthy gap in this literature; the elastic limit or first yield of sandwich beams in bending that precedes full plastic collapse. We aim to address this gap in the present chapter from the perspective of residual stress and its influence on the yield/fracture of the sandwich panel.

Chapter 4 demonstrated that the collapse behaviour of a sandwich panel in bending can be significantly altered when residual stress is present in the face sheets. We realise that the upper bound behaviour of sandwich beams will not be influenced by residual stress. However, we aim to extend our analysis of the first yield of face sheets to incorporate the influence of residual stress on the first yield. The aim of such analysis is to probe the potential for increased/decreased energy absorption due to a residual stress field,

introduced into the sandwich beam by design or via manufacturing defects. For example, if a thermoplastic sandwich panel is manufactured in one step via the combined solid and foam extrusion process then there is the potential for the presence of residual stress present in the face sheets and foam due to thermal gradients in the component during cooling and solidification. We employ an analytical, experimental and numerical analysis on elasto-plastic face sheets (polycarbonate) and elastic-perfectly plastic core (polyvinyl chloride foam).

In summary, we aim to address the following research questions in the present chapter.

1. Can we quantify the elastic limit for sandwich beams in bending?
2. Does a sandwich beam reach the elastic limit via differing mechanisms?
3. Is it feasible to experimentally introduce residual stress into a sandwich beam specimen and are there limitations?
4. Is it possible to quantify the influence of residual stress on the first of yield of the sandwich panels?
5. How is the failure of sandwich panels influenced by the presence of residual stress?

5.2 An analytical description of the influence of residual stress on the first yield and collapse modes of a sandwich beam in three-point bending

5.2.1 First yield via global bending and the influence of residual stress

Consider a sandwich beam in three-point bending, as shown in Figure 5.1, of depth b (into the page) and span L, comprising two face sheets of thickness t and a foam core

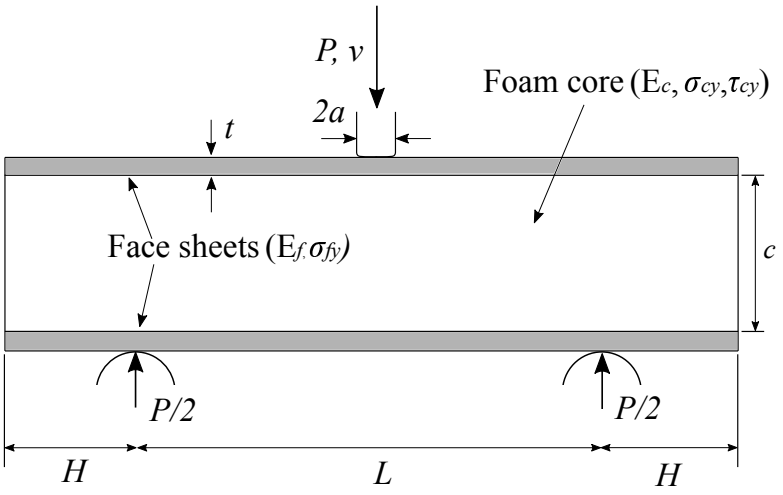

FIGURE 5.1: Geometry and loading for three-point bend

of thickness c. The second moment of area of the beam is given as $I_f = bt(t+d)^2/2$. The beam is loaded by a flat-bottomed punch of width $2a$. We define the apparent span as $L' = L - 2a$. The maximum moment M_{max} occurs at mid-span and the resulting maximum bending stress ($\sigma_f = M_{max}y/I_f$) in the beam occurs at the outer fibres in the face sheet (which has a cross-sectional area, $A_f = bt$) at an approximate distance $y = (t+c)/2 = d/2$ from the neutral axis (centre of the cross-section). In addition to the axial stress due to bending at the outer fibre of the beam, we now apply an additional uniform axial residual stress, $\sigma_{fR} = R/A_f$, in the face sheet. Equilibrium dictates, that at $y = d/2$ the total stress, σ_f in the face sheet is given as follows

$$\sigma_f = \frac{M_{max}d}{2I_f} + \frac{R}{A_f} \tag{5.1}$$

Under an applied moment $M_{max} = PL'/m$ ($m = 4 or 8$ for simply supported or clamped conditions respectively), the face sheet will attain first yield when the total stress σ_f reaches the material yield strength σ_{fy}. The load at first yield P_{fyR} may then be found by rearranging Equation 5.1

$$P_{fyR} = \frac{mbtd}{L'}(\sigma_{fy} - \sigma_{fR}) \tag{5.2}$$

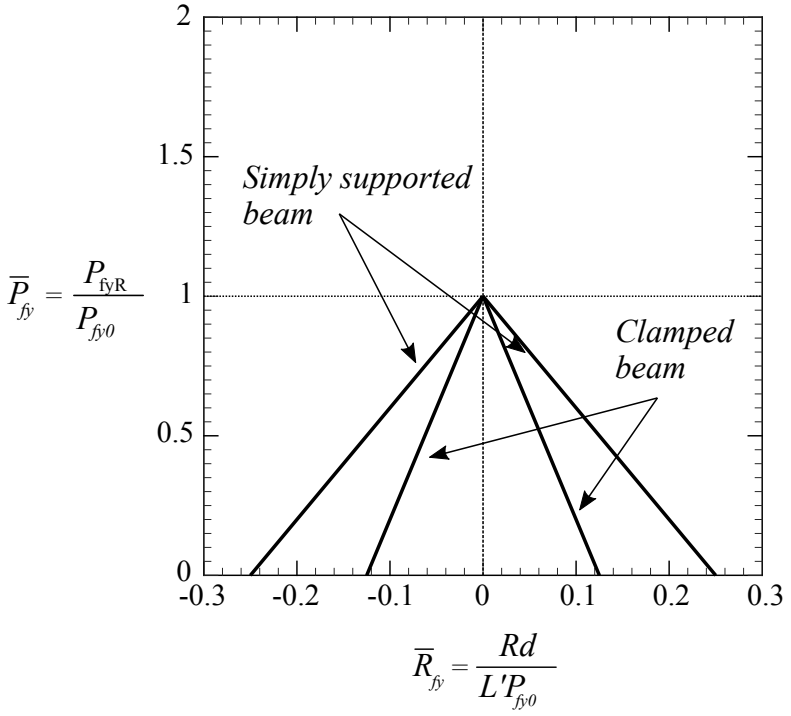

FIGURE 5.2: Predicted change in first yield load relative to the upper bound collapse load as a function of applied residual stress.

The resulting behaviour is that of a linear relationship between the collapse load P_{fyR} and the applied residual stress σ_{fR} in the face sheet. If we now normalise the first yield Equation 5.2 by the collapse load 2.12 we obtain a prediction of $\bar{P}_{fy}$, the change in load at which the elastic limit is exceeded, as a function of the dimensionless residual stress $\bar{R}_{fy} = Rd/L'P_0$

$$\frac{P_{fyR}}{P_{fy0}} = 1 - m\frac{Rd}{L'P_{fy0}} = 1 - m\bar{R}_{fy} \tag{5.3}$$

Figure 5.2 shows the change in collapse load $\bar{P}_{fy}$ obtained due to presence of residual stress (tensile or compressive) in the face sheet for any given set of material properties and sandwich geometry. We observe that if a residual stress is present in the face sheet, then, regardless of directionality, the load at which the elastic limit is exceeded will reduce.

We must now consider three scenarios in order to locate the point of first yield in the beam.

i) $\sigma_{fR} = 0$**:** if the face sheet material possesses the same uniaxial stress versus strain behaviour in tension and compression then both face sheets will yield simultaneously.

ii) $\sigma_{fR} > 0$**:** the lower, tensile face sheet will attain yield earlier whilst the upper, compressive face sheet will be protected from yield.

iii) $\sigma_{fR} < 0$**:** the upper, compressive face sheet will attain yield earlier whilst the lower, tensile face sheet will be protected from yield.

There are more complex scenarios where the tensile and compressive response of the face sheets are different from one another, however for the sake of brevity we list the three scenarios above. In general, once one of the face sheets yields, the remaining face sheet will proceed to the yield point whilst the core will begin to approach yield across the entire cross-section of the specimen. Once this occurs, the beam has reached full plastic collapse and the upper bound behaviour is detailed by Ashby et al. (2000) and described by Equation 2.12.

The above analysis assumes an elastic-plastic face sheet such as aluminium alloy or polycarbonate (as used in this study) which is typically used in sandwich beam construction. Now consider a face sheet that is made from an elastic-brittle material such as ceramics, GFRP or CFRP. It is clear that the analysis detailed in this section holds. We can predict the response of the beam to residual stress, the load, and location of failure. The beam however does not transition to full plastic collapse and instead is likely to fail catastrophically, or via other mechanisms that are beyond the scope of this analysis.

5.2.2 First yield via localised indentation and the influence of residual stress

We now identify another mode by which a sandwich beam may reach the elastic limit: localised indentation of the face sheet, and the mechanism is described as follows. The face sheet bends elastically local to the indenter and subsequently attains the yield

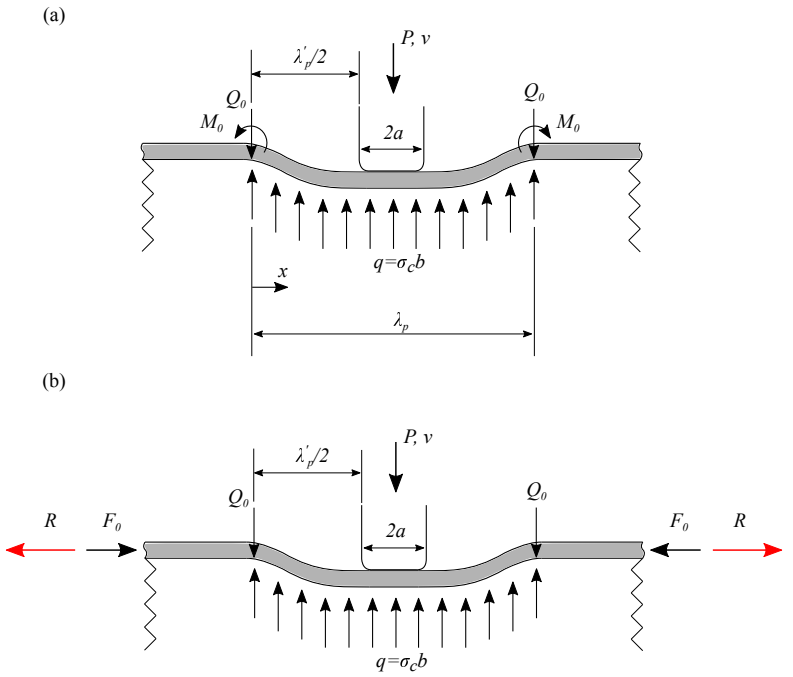

FIGURE 5.3: Loading of face sheet and foam foundation (a) without global bending present as seen in Soden (1996) and (b) the present case where global bending of the sandwich beam is present.

strength of the material upon sufficient displacement of the indenter. The face sheet is supported by foam that has undergone yield (local to the indenter) and serves to act as a perfectly-plastic foundation given the plateaued post yield behaviour of the foam itself. This mechanism has been identified by Soden (1996).

However we recognise that this localised mechanism is occurring in tandem with the action of a bending moment to the whole sandwich beam via three-point bending. In order to model such behaviour we treat the upper face sheet as an elastic beam in bending supported by a plastic foundation (as described), which is coupled via superposition, with a uniform compressive load in the face sheet due to the global bending moment. Now consider an additional uniform axial stress, compressive or tensile, in the face sheet due to the presence of a residual stress field. These three stresses may be superimposed and are described in detail later in the section.

In order to proceed with a solution to predict the elastic limit load, we choose to extend the Soden (1996) solution to account for a flat bottomed indenter. Soden (1996) predicted the load versus displacement response of an elastic beam on rigid plastic foundation subjected to point load as described by Equation 2.2, and the bending stress at

which the beam fractures or attains yield σ_f as

$$\sigma_f = \frac{9P^2}{16b^2t^2\sigma_{cy}} \tag{5.4}$$

Now consider the same mechanism as shown in Figure 5.3 with the elastic beam undergoing a load P. In this case the load is applied via flat bottomed indenter of width $2a$. The beam is supported by the rigid plastic foundation given as $q = \sigma_{cy}b$, whilst the reaction forces Q_0, and moments M_0 ensure that the face sheet remains attached. The distributed load q acts over a plastic zone length λ_p and we also define the region outside the indenter as $\lambda_p^{'} = \lambda_p - 2a$. We apply Euler beam theory to determine the displacement v_0 at the beam midspan

$$v_0 = \frac{\lambda_p^{'3}}{192E_fI_f}\left(P - 2ab\sigma_{cy} - \frac{b\sigma_{cy}\lambda_p^{'}}{2}\right) \tag{5.5}$$

M_0 is determined by assuming that the slope at the boundaries is zero and is given as

$$M_0 = \frac{(P - 2ab\sigma_{cy})\lambda_p^{'3}}{8} - \frac{b\sigma_{cy}\lambda_p^{'2}}{12} \tag{5.6}$$

Vertical equilibrium dictates that Q_0 is given as

$$Q_0 = \frac{(P - 2ab\sigma_{cy})}{2} - \frac{b\sigma_{cy}\lambda_p^{'}}{2} \tag{5.7}$$

It is clear that the moment, reaction force, and displacement all depend on the size of the plastic zone $\lambda_p^{'}$. If Equation 5.5 is differentiated with respect to $\lambda_p^{'}$ it is found that the plastic zone size has a maximum length $\lambda_p^{'*}$ given as

$$\lambda_p^{'*} = \frac{3(P - 2ab\sigma_{cy})}{2b\sigma_{cy}} \tag{5.8}$$

If Equation 5.8 is substituted into Equations 5.5 and 5.6 then we find that $M_0 = 0$ and that relationship between P and the maximum value of v^* as

$$v^* = \frac{27(P-2ab\sigma_{cy})^4}{6144b^3\sigma_{cy}^3} \tag{5.9}$$

Upon rearranging we get

$$P_L = Kbt^{3/4}\sigma_{cy}^{3/4}E_f^{1/4}v^{*1/4} + 2ab\sigma_{cy} \tag{5.10}$$

Here $K = (4/\sqrt{3})(2/3)^{1/4} \approx 2.1$. We now note that the maximum moment occurs at $x = \lambda_p^{'*}/2$ and is given as

$$M_{max} = \frac{3}{32}(P-2ab\sigma_{cy})^2 \tag{5.11}$$

and subsequently the maximum stress at the outer fibres of the face sheet can be determined as

$$\sigma_{max} = \frac{6M_{max}}{bt^2} = \frac{9(P-2ab\sigma_{cy})^2}{16bt^2\sigma_{cy}} \tag{5.12}$$

We can find the load at which a sandwich beam exceeds the elastic limit due to local indentation of the face sheet by considering the stress distribution in the face sheet. The stress distribution in the face sheet may be found by superposition in which we include the stress due to the bending of the face sheet local to the indenter as described by Equation 5.12 (now represented by subscript L), the residual stress $\sigma_{fR} = R/A_f$, and a compressive stress due to the global bending of the sandwich beam (represented by the subscript G). The total stress in the face sheet σ_f is thus given as follows

$$\sigma_f = \frac{M_L y_L}{(EI)_L} - \frac{M_G y_G}{(EI)_G} \pm \frac{R}{A_f} \tag{5.13}$$

Here $y_L = t/2$, $y_G = d/2$, $(EI)_G = E_f bt(t+c)^2/2$, and $(EI)_L = E_f bt^3/12$. This now gives us the following relationship between the elastic limit load P, the applied residual

stress in the face sheet σ_{fR}, and the constituent geometry and material properties of the face sheet and core as described previously

$$\pm\sigma_{fy} = \frac{9(P-2ab\sigma_{cy})^2}{16t^2\sigma_{cy}} - \frac{P(L-2a)}{mdt} \pm \sigma_{R,f} \tag{5.14}$$

Note that the above equation is quadratic in nature and thus has two solutions. We find the roots of the above equation, i.e. solutions for P. The lowest, positive root gives us the elastic limit load. However we must also consider that first yield may occur on the compressive side of the face sheet or on the tensile side. Thus we must solve Equation 5.14 twice; once for a positive yield stress (tension) and a second time for a negative value of yield stress (compression). We compare the two loads obtained and consider the lowest load as being the operative mode and location for first yielding. We note that since the axial load due to the global bending of the sandwich beam is compressive in nature, the first yield is more likely to occur on the compressive side of the face sheet unless a sufficiently high tensile residual stress is present in the beam. In the limiting case of no residual stress, we thus find that first yield always occurs on the compressive side of the face sheet.

It proves difficult to provide a tractable prediction of the relationship between change in first yield load due to the presence of residual stress as was carried out in Section 5.2.1. This is due to the quadratic nature of Equation 5.14 and the heavy dependency on geometry and material properties.

5.2.3 First yield via shearing of the core

The core shear collapse load was first predicted by Allen (1969). Allen (1969) shows that, during elastic bending of a sandwich beam via an applied load P, the core, due to its relatively low stiffness, carries an approximately uniform shear stress across the entire cross-section given by

$$\tau = \frac{P}{2btd} \tag{5.15}$$

Once the beam deflects sufficiently, the core will attain the core shear strength τ_{cy}. This gives the first yield load as

$$P = 2btd\tau_{cy} \tag{5.16}$$

If the beam geometry is chosen to ensure that it operates within the core shear collapse mode then full plastic collapse of the beam will occur via Equation 2.14 or Equation 2.15. If the beam geometry choice implies that full plastic collapse (or elastic indentation collapse) occurs then the beam will first yield via core shear and then proceed to the operative collapse mode.

We now consider the influence of residual stress on the first yield via core shear of a sandwich beam, once again in the knowledge that it does not influence the upper bound, full plastic collapse. The core shear yield mode is driven primarily by the yield strength of the foam. A situation where residual stress is present in the core will ensure that the core yields at lower loads than predicted by Equation 2.15 (when $\sigma_f = 0$) due to the presence of an additional tensile, or compressive axial load due to residual stress. We now quantify this knockdown by beginning with the Deshpande-Fleck yield surface for metal foams (Deshpande and Fleck (2000)). The yield surface for PVC foam is described using the Deshpande and Fleck yield surface as initially developed for metal foams (Deshpande and Fleck (2001)). Subsequently this was shown to be an accurate description for polymer foams provided an elastic buckling cap was included (Deshpande and Fleck (2001)). The yield surface of the foam is taken to be

$$\Phi = \hat{\sigma} - \sigma_{cy} = 0 \tag{5.17}$$

where σ_{cy} is the yield strength of the foam and $\hat{\sigma}$ is the effective stress, defined by

$$\hat{\sigma}^2 = \frac{1}{1+(\alpha_{DF}/3)^2}(\sigma_e^2 + \alpha_{DF}^2\sigma_m^2) \tag{5.18}$$

Here σ_e is the Von Mises effective stress and σ_m is the hydrostatic stress. The parameter α_{DF} describes the aspect ratio of the elliptical yield surface; J2 flow theory is recovered when $\alpha_{DF} = 0$. The present model assumes that the yield surface grows in a geometrically self-similar manner. The plastic strain rate is assumed to be normal to the yield surface such that associated flow prevails. Polymer foams have a zero plastic Poissons ratio, which results in $\alpha_{DF} \approx 2$. Introduce the (x_1, x_2, x_3) co-ordinate system as shown in Figure 5.1 where the x_3 direction is into the page. The stress state within the foam is as follows. A residual tension is present in the x_1 direction and is given as $\sigma_{11} = -2R/c$. The foam is unloaded in the remaining axial directions i.e. $\sigma_{22} = \sigma_{33} = 0$. A shear stress σ_{12} is present due to the applied load in three point bending and is given as $\sigma_{12} = \sigma_{21} = P_R/2c$. All other shear components are zero. Recall that the deviatoric tensor is given as $S_{ij} = \sigma_{ij} - \delta_{ij}\sigma_m$ where $\sigma_m = \sigma_{kk}/3 = -2R/3c$. We then express the Von Mises stress as

$$\sigma_e^2 = \frac{3}{2} S_{ij} S_{ij} = 3\left[S_{12}^2 + \frac{1}{2}\left(S_{11}^2 + S_{22}^2 + S_{33}^2\right)\right] \tag{5.19}$$

Now we find the components of the deviatoric tensor which are all given as follows. $S_{11} = -4R/3c$,$S_{22} = S_{33} = 2R/3c$, and $S_{12} = S_{21} = P/2c$. Combining these with Equation 5.19 gives the following relationship between the Von Mises equivalent stress σ_e, collapse load P_R, and the applied residual tension R

$$\sigma_e^2 = 3\left[\left(\frac{P_R}{2c}\right)^2 + 3\left(\frac{2R}{3c}\right)^2\right] \tag{5.20}$$

We then combine Equation 5.20 and the Deshpande-Fleck yield surface (Equation 5.18) to achieve a relationship between the applied residual stress R, the foam compressive strength σ_{cy}, and the resulting collapse load P_R

$$\sigma_{cy}^2 = \frac{1}{1 + (\alpha_{DF}/3)^2}\left[3\left(\frac{P_R}{2c}\right)^2 + (9 + \alpha_{DF}^2)\left(\frac{2R}{3c}\right)^2\right] \tag{5.21}$$

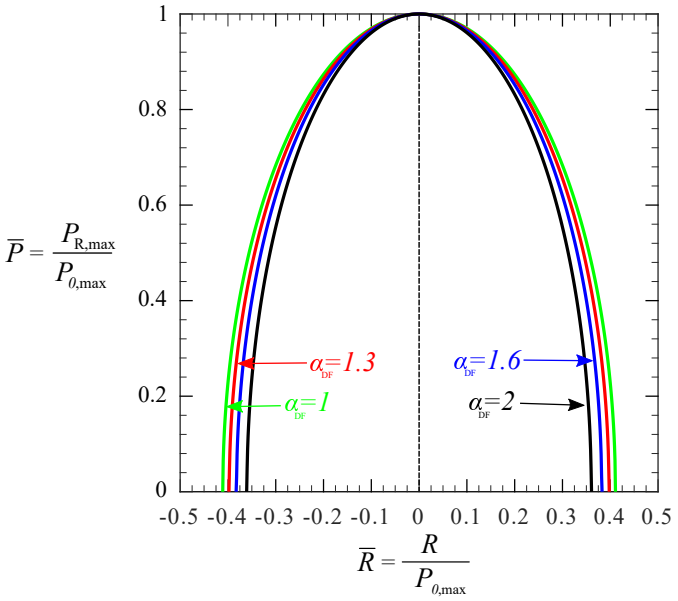

FIGURE 5.4: Influence of residual stress on the peak load of a sandwich specimen in the core shear first yield mode.

When $R = 0$ we obtain the collapse load P_0 with the definition as described by Equation 5.16. If we now rearrange Equation 5.21 and normalise by P_0, we obtain a relationship between the change in collapse load and the applied residual stress which is shown in Figure 5.4 for a number of values of α_{DF} and is described by the following equation

$$\frac{P_R}{P_0} = \left(1 - \frac{(9+\alpha_{DF}^2)}{3}\left(\frac{4R}{3P_0}\right)^2\right)^{1/2} \tag{5.22}$$

5.3 Experimental behaviour of an elasto-plastic sandwich beam in three-point bending subjected to residual stress

5.3.1 Analysis of the experimental procedure for prestressing

It is instructive to quantify the expected residual stress present in a specimen prior to a three-point bend experiment. Here we present a simple analytical description of the chosen experimental prestressing procedure. In this study, we aim to bring a sandwich panel into a state of equillibrium with a residual stress field present, comprising a tensile stress in the face sheets and a compressive stress in the core. This is illustrated in Figure 5.5 and achieved via the following steps

(i) The foam and both face sheets are unbonded and unstressed ($\sigma_c = \sigma_f = 0$).

(ii) A tensile stress, σ_{f0} is applied to the face sheets, where $\sigma_{f0} < \sigma_{fy}$. The foam core remains unstressed and unbonded ($\sigma_c = 0$).

(iii) The unstressed core is bonded between the face sheets. The face sheets remain at σ_{f0} for a period of Δt whilst the adhesive cures.

(iv) The load is released on the bonded sandwich structure. In the process of reaching a state of equilibrium, the stress in the face sheet reduces to σ_{fR} via a change in strain $\Delta\varepsilon$ which results in a compressive stress of σ_{cR} in the core.

$\Delta\varepsilon$ describes the loss in tensile load in the face sheet due to the mismatch in Young's modulus of both core and face sheet materials. This loss is a consequence of the chosen experimental methodolgy in this study. $\Delta\varepsilon$ may be expressed as

$$\Delta\varepsilon = \frac{\Delta\sigma_f}{E_f} = \frac{\Delta\sigma_c}{E_c} \tag{5.23}$$

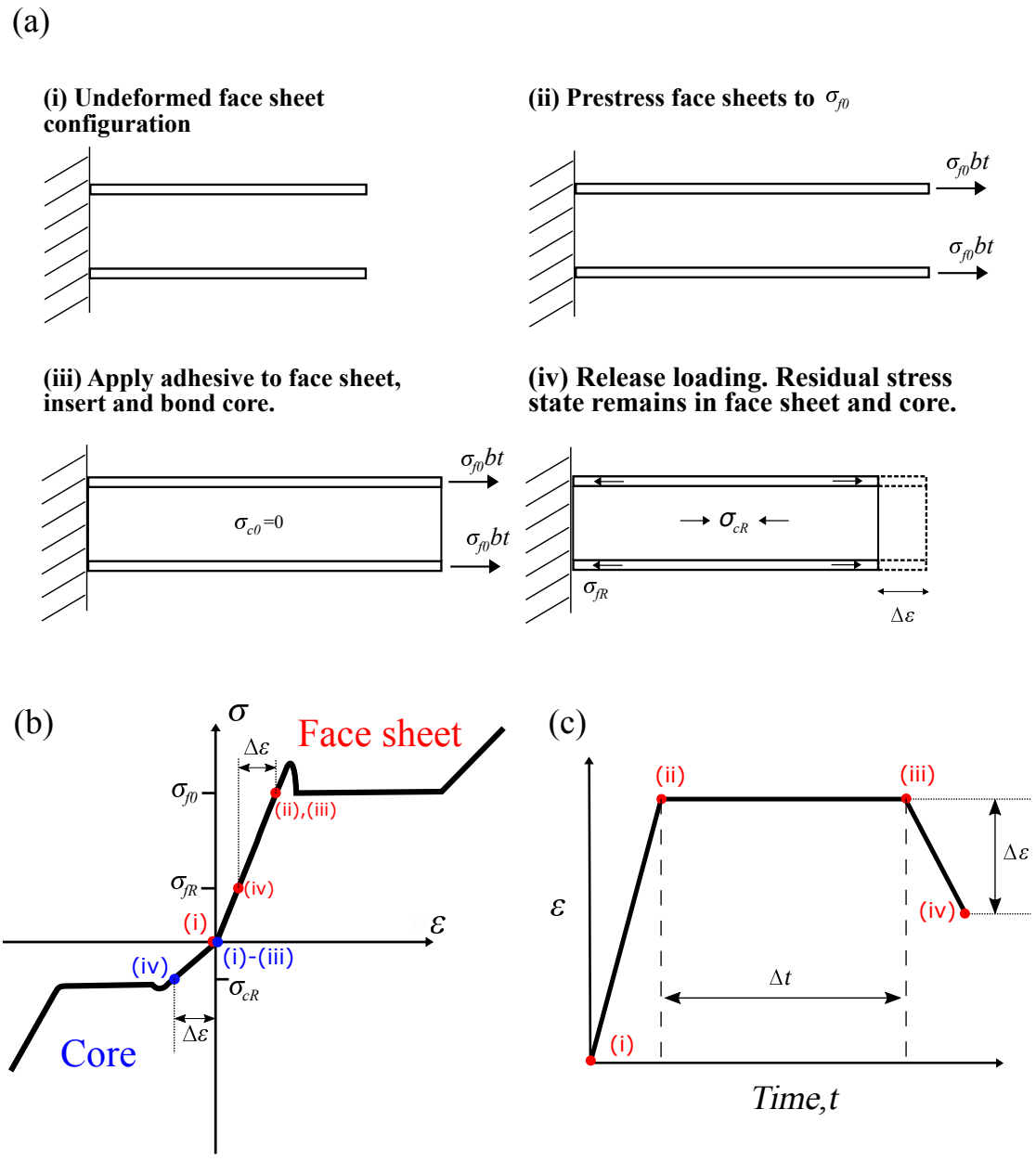

FIGURE 5.5: (a) Schematic of experimental prestress procedure. (b) Stress and strain state in face sheet and core during and after the experimental prestress procedure. (c) Strain state in the face sheet as a function of time.

where E_f and E_c are the Young's modulus of the face sheet and core respectively. $\Delta\varepsilon$ is the change in strain during unloading between state (iii) and (iv). As a result, the stress in the foam and the face sheets at the final state (iv), may be given as follows

$$\sigma_{fR} = \sigma_{f0} + \Delta\sigma_f \tag{5.24}$$

$$\sigma_{cR} = 0 + \Delta\sigma_c \tag{5.25}$$

Equilibrium of the foam and face sheets in the final state B dictates that

$$2t\sigma_{fR} = c\sigma_{cR} \tag{5.26}$$

Equating Equations 5.23 - 5.26 enables the prediction of the change in strain of the sandwich beam between state (iii) and (iv) as a function of the initial load in the face sheet and material Young's modulus, face sheet thickness, t, and core thickness, c

$$\Delta\varepsilon = -\frac{\frac{2t}{c}\frac{\sigma_{f0}}{E_f}}{\frac{2t}{c} + \frac{E_c}{E_f}} \tag{5.27}$$

In addition to this, the final stress induced in the face sheet may also be given as follows

$$\sigma_{fR} = \frac{\sigma_{f0}}{2\frac{E_f}{E_c}\frac{t}{c} + 1} \tag{5.28}$$

If the core was prestressed in compression whilst the face sheets were simultaneously prestressed in tension and subsequently bonded then there would be no loss in residual stress. In practice it is difficult to apply a compressive load to the core due to its length; column buckling is likely to occur. A more practical, but not ideal, method has been described in general above and the detailed experimental procedure will be described in Section 5.5. This methodology is inspired by the prestressed steel reinforced concrete used in civil engineering applications.

5.3.2 Limitations on material selection due to experimental methodology

The general conclusion from the analysis in Section 5.3.1 is that the chosen experimental prestressing method does not produce the same level of residual stress state as that of the ideal case. This places limits on material selection for face sheet and core materials. If we assume that the desire is to place the sandwich beam in the maximum possible residual stress state, then we assume that we load a material to its elastic limit (ε_f). We now take Equation 5.29 and normalise

$$\hat{\varepsilon}_L = \frac{\Delta\varepsilon}{\varepsilon_f} = -\frac{1}{1+\frac{c}{2t}\frac{E_c}{E_f}} \tag{5.29}$$

This equation gives a design space for a sandwich beam in terms of the constituent geometry and stiffness properties with the goal of minimising $\hat{\varepsilon}_L$. The relationship between $\hat{\varepsilon}_L$ and t/c for a variety of Young's modulus mismatches ($\bar{E} = E_f/E_c$) is shown in Figure 5.6. It is clear that as the mismatch in Young's modulus increases, the allowable t/c space in which a small loss in residual stress occurs becomes increasingly limited.

Consider the GFRP and H200 PVC foam from Chapter 4. The modulus mismatch is approximately $\bar{E} = 200$ and thus severely limits the maximum residual stress in the face sheet to $0 < \hat{\varepsilon}_L < 0.3$ for values of $t/c < 1$. Thus we find that the loss in tension $\Delta\varepsilon$ is large for a GFRP face sheet prestressed to approximately its failure load. The loss in tension is in fact approximately equal to the pretension applied for a significantly large range of t/c resulting in no induced residual stress in the sandwich structure. It must be noted that geometry plays a role, but in this case the stiffness of the material is so high that the loss in tension is a dominant factor. If, in contrast, we choose a PC face sheet and H200 foam core, ($\bar{E} \approx 15$), we find that, for most geometries, the efficiency is higher than the GFRP and H200 sandwich panel, and it is indeed possible to achieve much lower losses, with the loss in residual stress exceeding $\hat{\varepsilon}_L > 0.5$. We conclude that, when using the present methodology of applying a residual stress to a sandwich

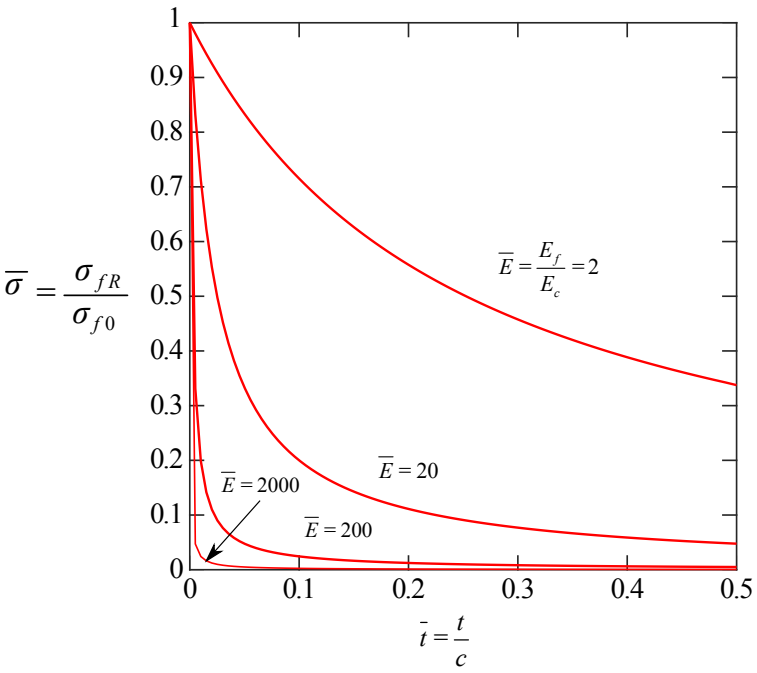

FIGURE 5.6: Loss of residual stress during the experimental prestress procedure for a variety of E_f/E_c

panel, a system comprising PC face sheets and H200 foam core is more practical than the GFRP/PVC foam combination.

5.4 Material characterisation and design of experiments

A typical three-point bend experimental setup is shown in Figure 5.1. First yield and collapse mode maps may be constructed for a given set of face sheet and core materials using the equations outlined in Section 5.2. We form a collapse mode map based on the competing modes of collapse (elastic indentation, core shear and face microbuckling) as outlined in Chapter 2 and a first yield map (face yield, indentation, and core shear) in the same manner based on the equations in Section 5.2. The collapse/first yield map is formed by choosing a square matrix within a range of reasonable normalised geometry variables: $\bar{t} = t/c$ and $\bar{c} = c/L$. The collapse/yield load for all potential modes was calculated at each matrix point and the minimum and thus operative mode was found.

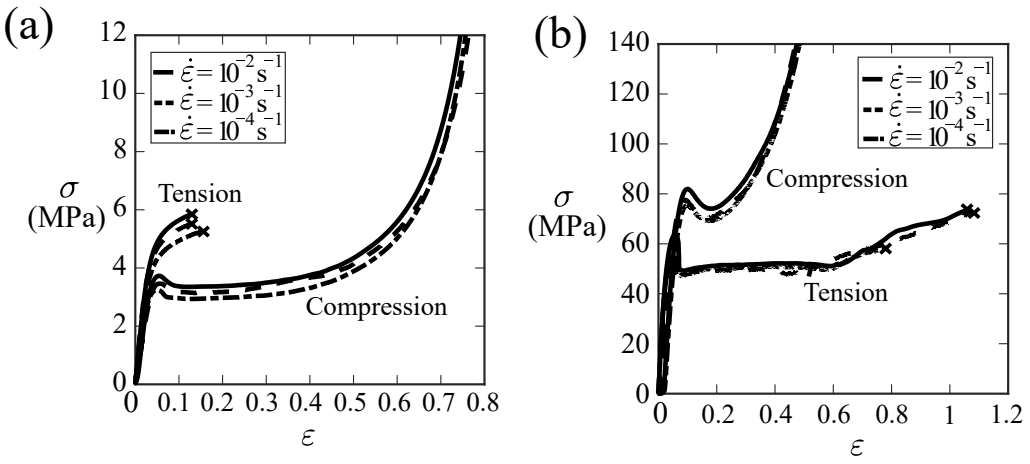

FIGURE 5.7: Nominal tensile and compressive stress strain relationships with strain rates in the range to for (a) Divinycell H200 foam and (b) Lexan Polycarbonate.

The materials used within this study were Lexan 9030-112 polycarbonate face sheets and Divinycell H200 PVC foam core, for which the appropriate properties were measured (as described in Chapter 3). The polycarbonate face sheet properties are as follows: $\sigma_f = 52MPa$, and $E_f = 2.45GPa$. The Divinycell H200 core properties are: $\sigma_c = 3.17MPa$, $E_c = 125MPa$ and $\tau_c = 2.7MPa$. The nominal tensile, and compressive stress-strain curves associated with PC face sheets, and H200 foam core are shown in Figure 5.7.

The constituent properties were then used to form the collapse mode maps shown in Figure 5.8 for both a flat punch ($\bar{a} = 0$), and for a roller ($\bar{a} = 0.025$). The points A-F highlighted in Figure 5.8 indicate the experimental points that are probed. Table 5.1 and 5.2 outline the experimental geometries for each of these points. It is important to highlight that we do not probe the core shear response. The geometries required for such a specimen require extremely thick face sheets with little separation due to very thin cores. The structure thus deviates from the traditional idea of a sandwich beam and we exclude this particular mode from our experimental and finite element analysis, and leave for future work.

TABLE 5.1: Details of the sandwich beam geometry for each three point bending experiment using a flat indenter with $\bar{a} = 0.025$ for each representative mode of collapse, face yield, elastic indentation, plastic indentation. Note that the overhang length, L_0, is 50mm in each case and that $R = 19mm$ for cases A and D, and $R = 4mm$ for case C.

Case	Collapse mode	$\bar{t}$	$\bar{c}$	t (mm)	c (mm)	L (mm)	2a (mm)	σ_{fR} (MPa)
A	FY	0.1	0.04	1	10	250	10	16
B	PI	0.05	0.2	1	20	100	4	28
C	PI	0.1	0.4	1	10	25	1	16

TABLE 5.2: Details of the sandwich beam geometry for each three point bending experiment using a cylindrical indenter of diameter D for each representative mode of collapse, face yield, elastic indentation, plastic indentation. Note that the overhang length, L_0, is 50mm in each case and that $R = 19mm$ for cases A and D, and $R = 4mm$ for case C.

Case	Collapse mode	$\bar{t}$	$\bar{c}$	t (mm)	c (mm)	L (mm)	2a (mm)	σ_{fR} (MPa)
D	FY	0.1	0.04	1	10	250	10	16
E	PI	0.05	0.2	1	20	100	4	28
F	PI	0.1	0.4	1	10	25	1	16

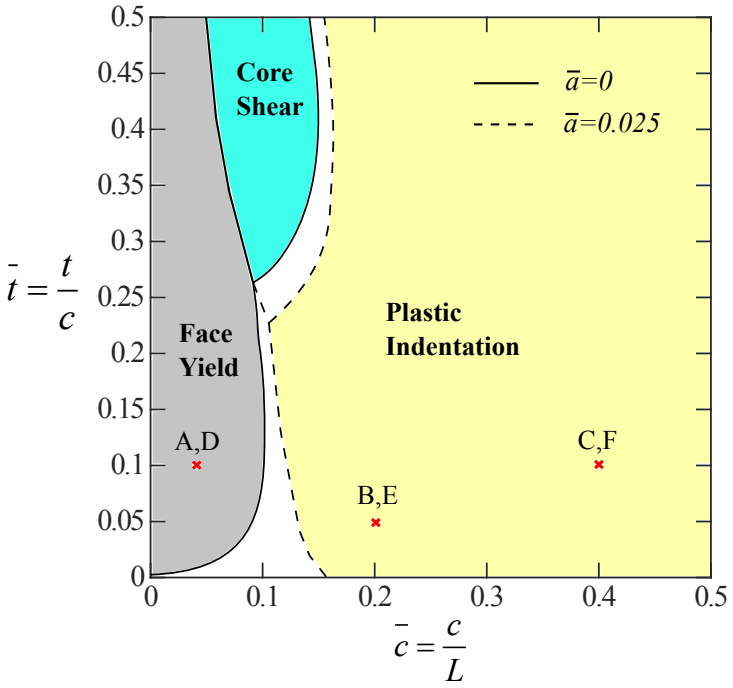

FIGURE 5.8: Collapse mode map for a sandwich beam made from Divinycell H200 foam core and Lexan PC face sheet under three-point bend, with a cylindrical ($\bar{a} = 0$) and flat indenter geometry ($\bar{a} = 0.025$).

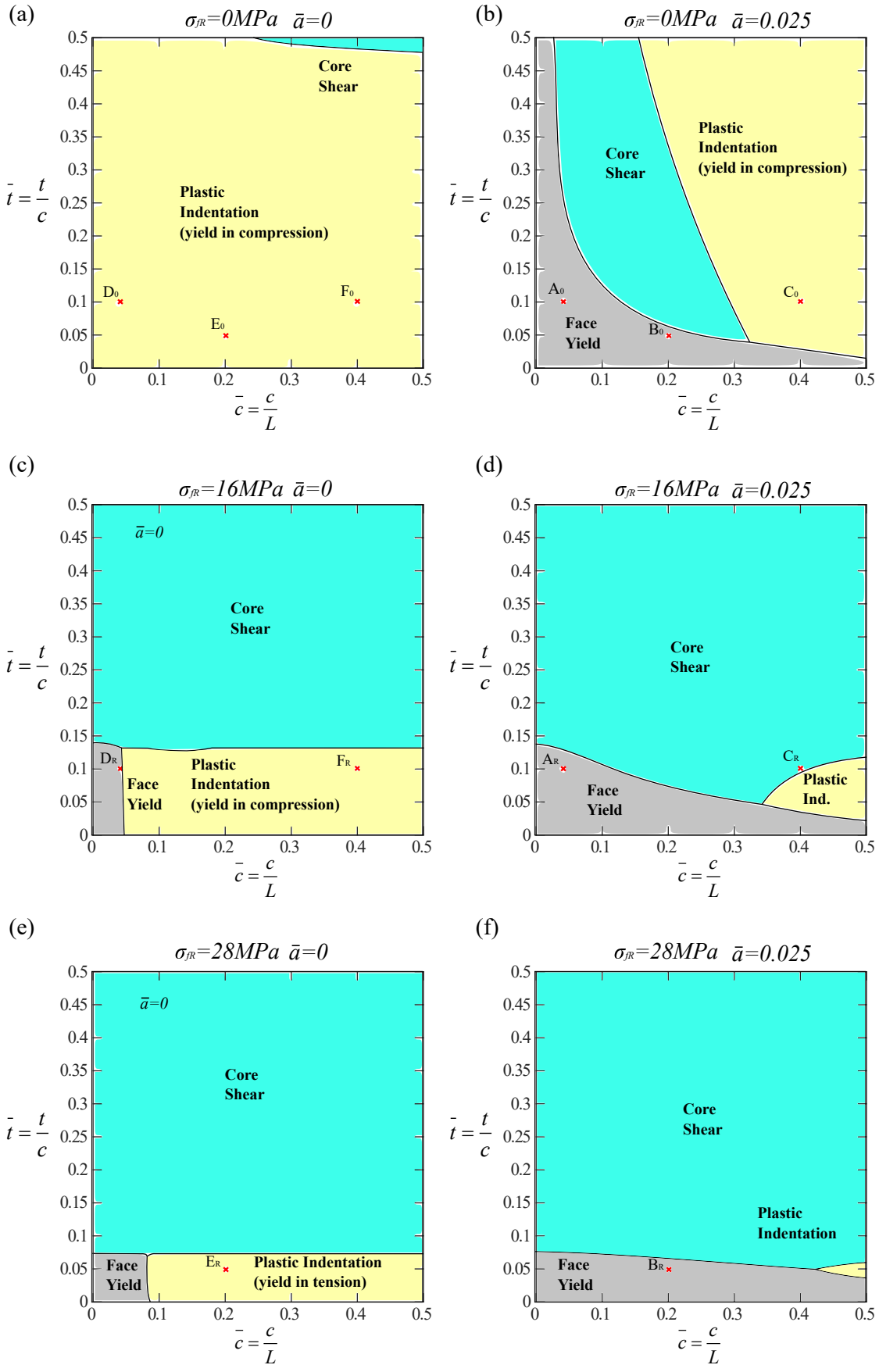

FIGURE 5.9: First yield mode map for a sandwich beam made from Divinycell H200 foam core and Lexan PC face sheets under three-point bend, with (a), (c), (e) a cylindrical indenter geometry ($\bar{a} = 0$) and (b), (d), (f) a flat indenter geometry ($\bar{a} = 0.025$). Residual stress levels, σ_{fR}, vary in each case.

5.5 Experimental procedure

5.5.1 Specimen preparation and prestress procedure

Two polycarbonate dogbones were manufactured and clamped together in the assembly shown in Figure 5.10. The assembly was placed in a screw driven Instron tensile testing machine and then the PC sheets were stretched simultaneously. Once they were stretched to a load corresponding to the yield point of the PC, the Instron was set to hold the assembly at a fixed displacement. Subsequently Loctite 401, low viscosity and fast curing, cyanoacrylate adhesive was spread on both faces of the polycarbonate. The foam core was then inserted between the face sheets and the assembly was subsequently clamped and allowed to cure for 30 minutes before unloading. A strain gauge (FLA-6-11 manufactured by Tokyo Measuring Instruments Lab.) with a maximum strain limit of 5% was placed in the centre of one of the face sheets and enabled the measurement of strain during prestressing, the loss in strain within the curing interval and finally the change in strain, $\Delta\varepsilon$ during and after unloading of the sandwich beam. Once unloading was complete, the assembly was removed from the Instron and the ends were removed using a band saw, leaving only the prestressed three point bend specimen. The strain gauge was used to ensure that the residual stress remained after the cutting procedure.

5.5.2 Three-point bend procedure

The three-point bend test was carried out immediately after the prestressing procedure. The support rollers were 19mm (or 4mm in case C and F) in diameter and all tests were carried out at a crosshead speed of L/100 mm/min. Two indenters were used: a flat indenter ($2a/L = 0.025$), and a cylindrical indenter with $D/L = 0.025$ (as with the flat indenter). Digital image correlation was used to measure the extent of indentation, i.e. the displacement of the top face sheet relative to the displacement of the bottom face sheet. The images taken during this procedure were also used to assess the collapse mode.

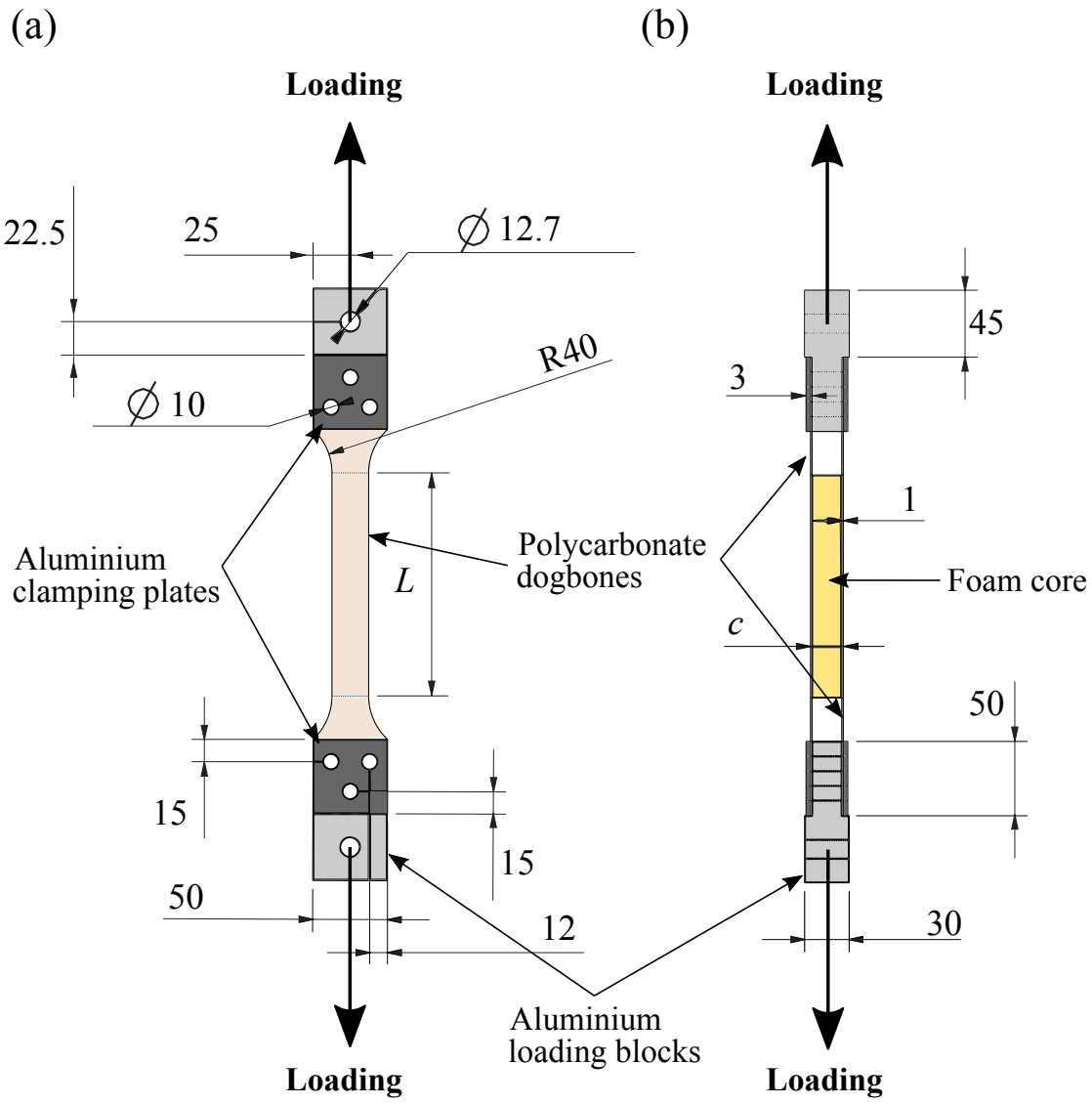

FIGURE 5.10: (a) Front and (b) side view of the experimental setup for prestressing a sandwich beam. Note that the foam core is only inserted in step (iii) as described in Section 5.3.1. All dimensions are in millimetres.

5.6 Finite element methods

The analytical models of Section 5.2 are validated via both experiment and finite element simulations. The finite element methodologies for carrying out a three point bend test on a sandwich beam whilst subjected to a residual stress field are outlined in Section 4.4 of Chapter 4. We use the same methodologies in this chapter. However, we now use PC face sheets and H200 PVC foam. The material model for the H200 foam is outlined in Appendix A. The material model for the PC face sheet is described as follows. The PC face sheet was modelled as an isotropic, rate-independent, Von Mises

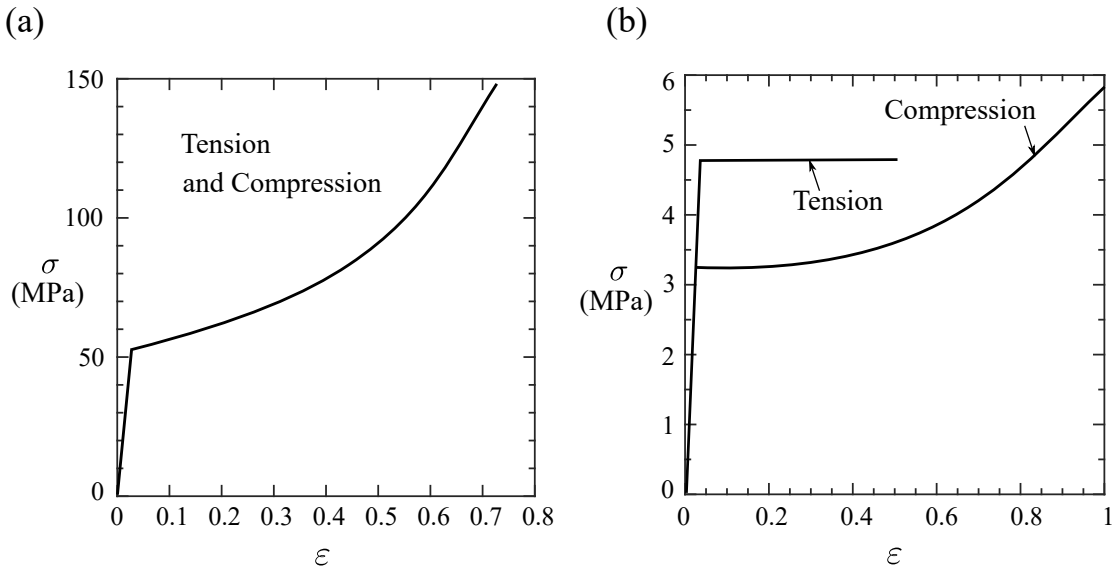

FIGURE 5.11: Uniaxial true stress versus logarithmic strain responses for the FE simulations: (a) PC face sheet and (b) PVC H200 foam core.

solid with a true stress versus true strain response as shown in Figure 5.11. This curve is derived from the measured response of PC face sheet in uniaxial tension (at a strain rate of $10^{-4}s^{-1}$) upon assuming a bi-linear fit for the post-yield nominal stress versus nominal strain data of Figure 5.7. The elastic modulus and Poisson's ratio are taken as $E_f = 2$ GPa and $\nu_f = 0.3$, respectively, based on the measured values in uniaxial tension. Failure and rate sensitivity of PC was not included in the FE model.

5.7 Results and discussion

5.7.1 Experimental prestressing procedure

We note that once the loading of the face sheets is complete and the Instron is set to a fixed displacement, the face sheet exhibits viscoelastic stress relaxation. This results in a loss of approximately 20% of applied prestress. An example of the face sheet strain history during prestressing is given in Figure 5.12. It is evident that the strain remains constant during the curing interval with some small fluctuations which were unavoidable due to clamping of the specimen. In addition some error may be present here due to a thermal strain component from heat released during curing of the adhesive. Although

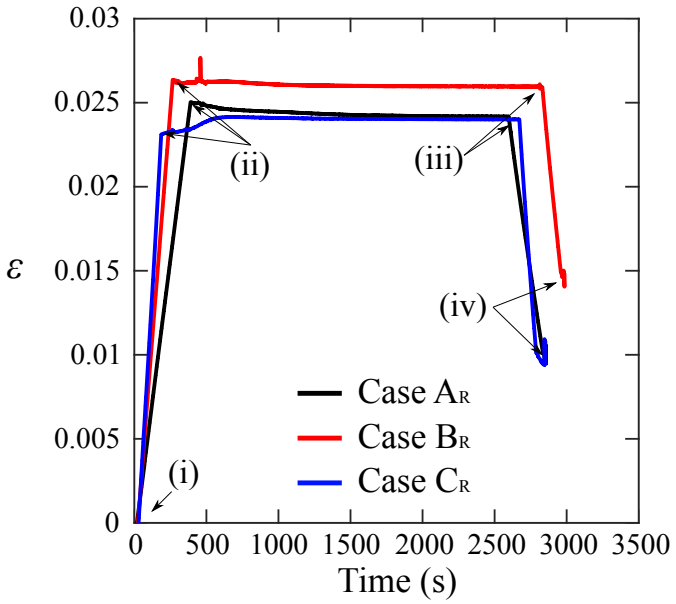

FIGURE 5.12: Strain versus time on one of the PC face sheets during the experimental prestress procedure. Each step during the prestressing procedure is illustrated in Fig.5.5 and is as follows. (i) Face sheet and foam are undeformed, (ii) face sheets have been stretched to σ_{f0}, (iii) adhesive has been applied, foam has been inserted, and adhesive cured, (iv) fully cured sandwich structure has been unloaded

after 30 minutes of curing these effects will have dissipated and the specimen will have reached thermal equilibrium. Subsequently, once unloading is complete there is a small loss in strain which results from creep of the foam, adhesive and polycarbonate. This creep was monitored over a 24 hour period and it was found that it reached a steady state after approximately 30 minutes with the same strain level measured 1 day later.

5.7.2 First yield via global bending

5.7.2.1 Finite element results

Here we validate the relationship given by Equation 5.3 and shown in Figure 5.2. We choose a single geometry that lies within the face yield mode of first yield and collapse and then subject it to varying magnitudes of residual stress fields in the face sheets. The geometry and residual stress values are given in Table 5.3. The first yield load is measured by the load at which the Von Mises equivalent stress exceeds the yield strength of the material.

TABLE 5.3: Geometry and residual stress levels for the numerical validation of the analytical model for first yield via global bending

Geometry: t=1mm, c=20mm, L=200mm, $\bar{t} = 0.05$, $\bar{c} = 0.1$, $2a = 10mm$							
$\bar{R}$	0	0.05	0.1	0.2	-0.05	-0.1	-0.2
σ_{fR} (MPa)	0	8.684	14.87	22.88	-8.684	-14.87	-22.88

A sample of the load versus displacement response for a specimen as described in Table 5.3 with residual stress levels of $\bar{R}_{fy} = \{0, 0.1, -0.1\}$ is given in Figure 5.13(a). Furthermore, in Figure 5.13(b), we provide the finite element predictions for the full range of simulations carried out to predict the change in first yield load as predicted by Equation 5.3. It is clear that the finite element results are in broad agreement with Equation 5.3 and a reduction in first yield load is observed regardless of whether the stress is compressive or tensile. The load versus displacement response of Figure 5.13(a) shows that little change in the final collapse load occurs as predicted whilst overall energy absorbed (i.e. area under the curve) is reduced due to the presence of residual stress.

Figure 5.13(c) shows the location (in grey) of first yield for (i) a specimen with no residual stress present, and as expected both face sheets yield simultaneously which is immediately followed by buckling of the upper face sheet due to compressive yielding of the PC. This is indicated in Figure 5.13(a) as softening following the peak load which is linked with the loss in cross-section of the beam following buckling. In Figure 5.13(c) (ii) and (iii), as expected, we observe a switch in location of yield to the bottom face sheet when a tensile residual stress is present and the upper face sheet when a compressive residual stress field is present, whilst the opposite face sheet in both cases remains elastic. Note that when a compressive residual stress exists, there is a small drop in the load at which buckling occurs relative to the other specimens due to the fact that the beam reaches this load more readily due to an additional compressive load in the face sheet.

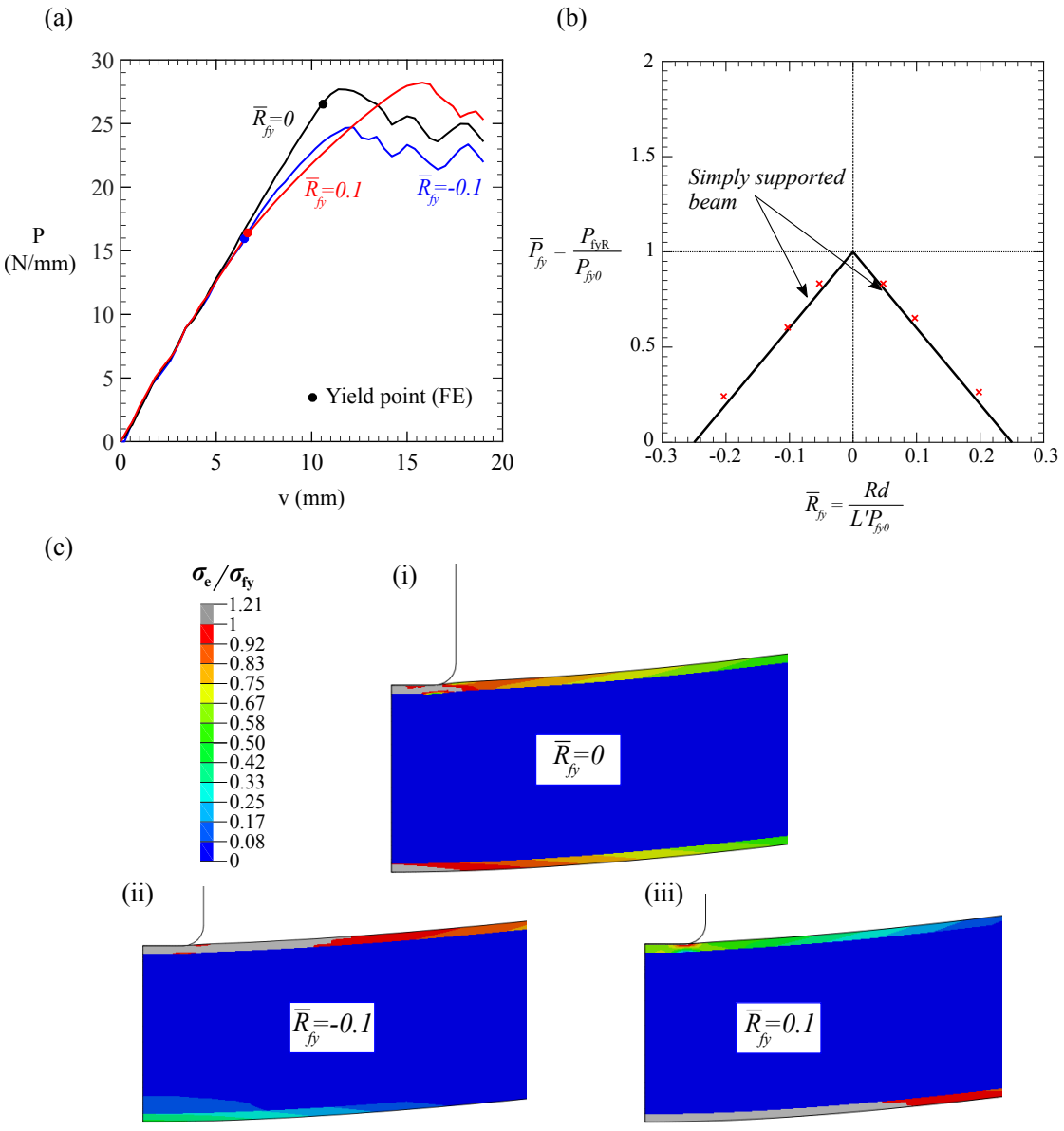

FIGURE 5.13: Comparison of the experimental, finite element, analytical load versus indentation responses for a prestresseed and non-prestressed face yield specimen (a) flat indenter, (b) cylindrical indenter $D = 10mm$

5.7.2.2 Experimental results

The load versus displacement response of the experimental points for a flat punch A_0 and A_R and a cylindrical indenter D_0, and D_R, as defined in Tables 5.1 and 5.2 are given in Figures 5.14(a) and (b). In general, we achieve excellent agreement between experiment, finite element, and analytical models for the elastic and collapse response of the sandwich beam. Due to experimental constraints, it was not possible to obtain first yield information from the experiments, and we rely on first yield data from the

corresponding finite element models. As expected, we observe very little change in the collapse load despite the presence of residual stress. An elevation in collapse load is observed in cases A_0 and A_R relative to D_0 and D_R due to the use of a flat punch which is as predicted.

The final failure of the specimen is observed to change based on the shape of the indenter and the level of residual stress. If a flat punch is used then we find that immediately after collapse (the peak load), failure occurs on the tensile side of the beam which is shown in Figure 5.14(c). Crack initiation occurs within the foam due to its low ductility ($\varepsilon_f \approx 0.16$). The face sheet alone must carry the load and thus the strain in the face sheet increases rapidly resulting in fracture and catastrophic failure of the beam itself. This failure mode occurs irrespective of the residual stress level. In contrast, if a cylindrical indenter is used, two different failure modes will occur. When there is no residual stress present, case D_0, the upper face sheet will begin to buckle when collapse occurs (as shown in Figure 5.14(d)), and as described in Section 5.7.2.1. If a tensile residual stress is present such as in case D_R, then we observe the tensile face to fail as described above (Figure 5.13(e).

5.7.3 First yield via local indentation

We now validate the relationship between first yield load/location and applied residual stress via finite element models accompanied by experimental analysis. Firstly, the load versus displacement response for cases B_0, B_R, E_0 andE_R are presented in Figures 5.15(a) and (b). We observe excellent agreement between experiment, finite elements and analytical model (collapse load for plastic indentation). The first yield maps in Figures 5.9(a) and (e) indicate that the beam should yield via localised indentation when loaded by a cylindrical roller (E_0 and E_R). However they also show that there is a transition between two types of localised indentation: yield on the compressive side of the upper face sheet when there is no residual stress, and yield on the tensile side of the face sheet when a residual stress is present. This transition is observed as expected and the location of yield is confirmed in the finite element contours of Figures 5.15(c) and (d). The collapse mode map shown in Figure 5.8 indicates that the final collapse mode

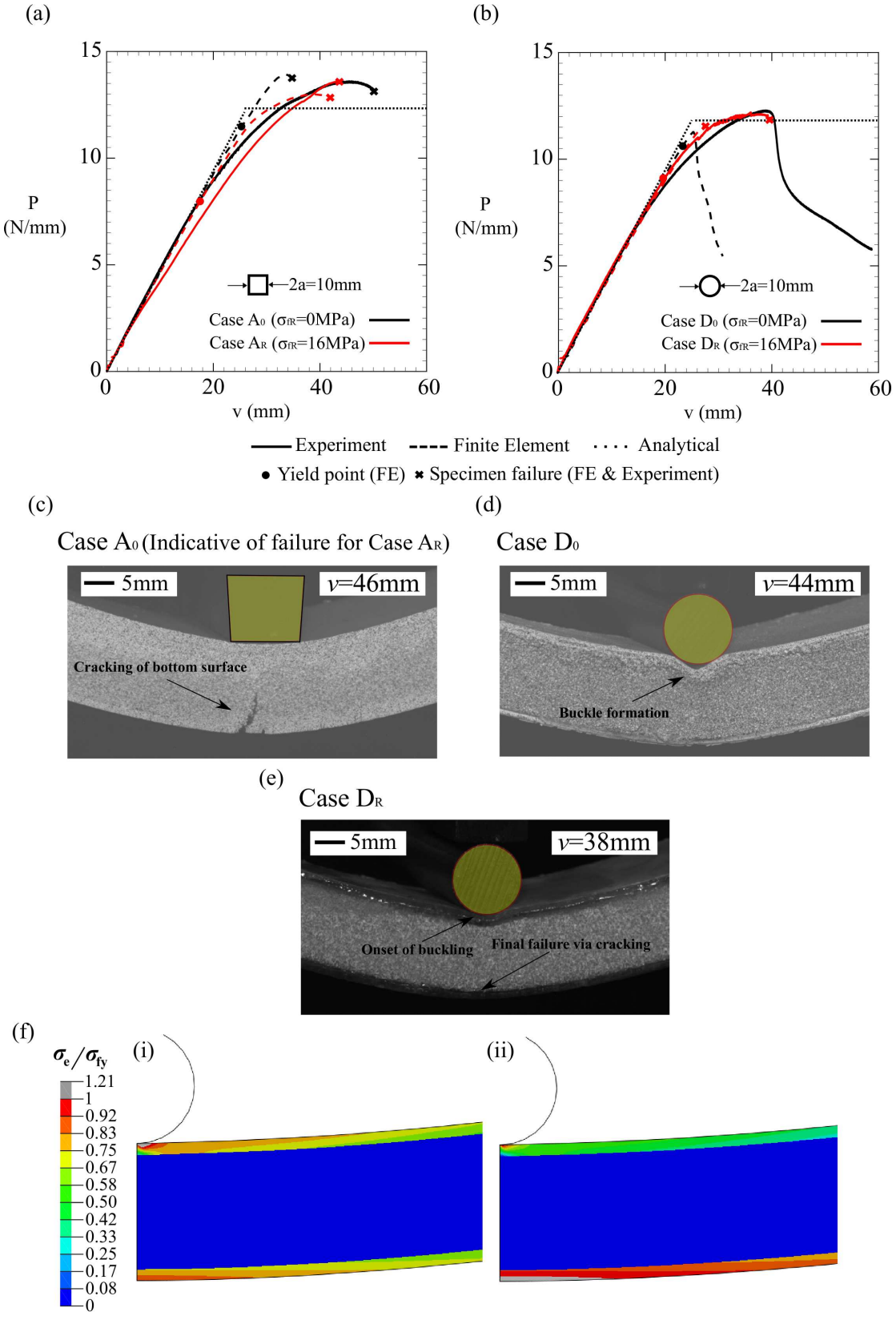

FIGURE 5.14: Comparison of the experimental, finite element, analytical load versus indentation responses for a prestresseed and non-prestressed face yield specimen (a) flat indenter, (b) cylindrical indenter $D = 10mm$

is plastic indentation, this is the case for both cylindrical roller and flat punch as shown Figures 5.15(e) and (f).

The load versus displacement response for cases C_0, C_R, F_0 andF_R are shown in Figure 5.16(a) and (b). Broad agreement is found between experiment, finite element and analytical models. In all cases, the first yield mode is via localised indentation whilst the final collapse mode is in the plastic indentation region as confirmed by the plastic hinge formation observed during experiments (see Figure 5.16(c) and (d)). The results of finite element and experiments all conform to this prediction. Like the cases B_0, B_R, E_0 and E_R, we observe a reduction in load at which first yield is exceeded when residual stress is present. Likewise we confirm the predictions made by Equation 5.14. In the cases C_0, C_R, F_0 andF_R we do not observe specimen failure. This is based on the fact that the strain in the tensile face sheet is limited due to the thin core used whilst the tensile residual stress level is low. Contrary to this we observe failure in B_R, and E_R due to a thicker beam and the presence of a large residual stress.

5.8 Concluding remarks

This chapter has analysed the elastic limit of sandwich beams, the three competing mechanisms that govern first yield/fracture, and the full plastic collapse of the sandwich beams, all from the perspective of an applied residual stress field. We have described analytical models for the first yield loads and an experimental, and numerical approach for applying a residual stress to a sandwich beam and its subsequent effect on the yield, collapse and post-collapse behaviour.

The analytical models predict that the presence of residual stress, regardless of the mode, causes a reduction in the yield behaviour of the beam, i.e. a beam will always reach the elastic limit at a lower load due to the presence of a residual stress in the face sheets or core. This is confirmed by finite element simulations on a sandwich beam comprising PC face sheets and PVC foam core. The analytical models allow us to form a map indicating the operative elastic limit mode, akin to that of the collapse mode maps of Chapter 4. We observe that these maps vary significantly depending on the level of

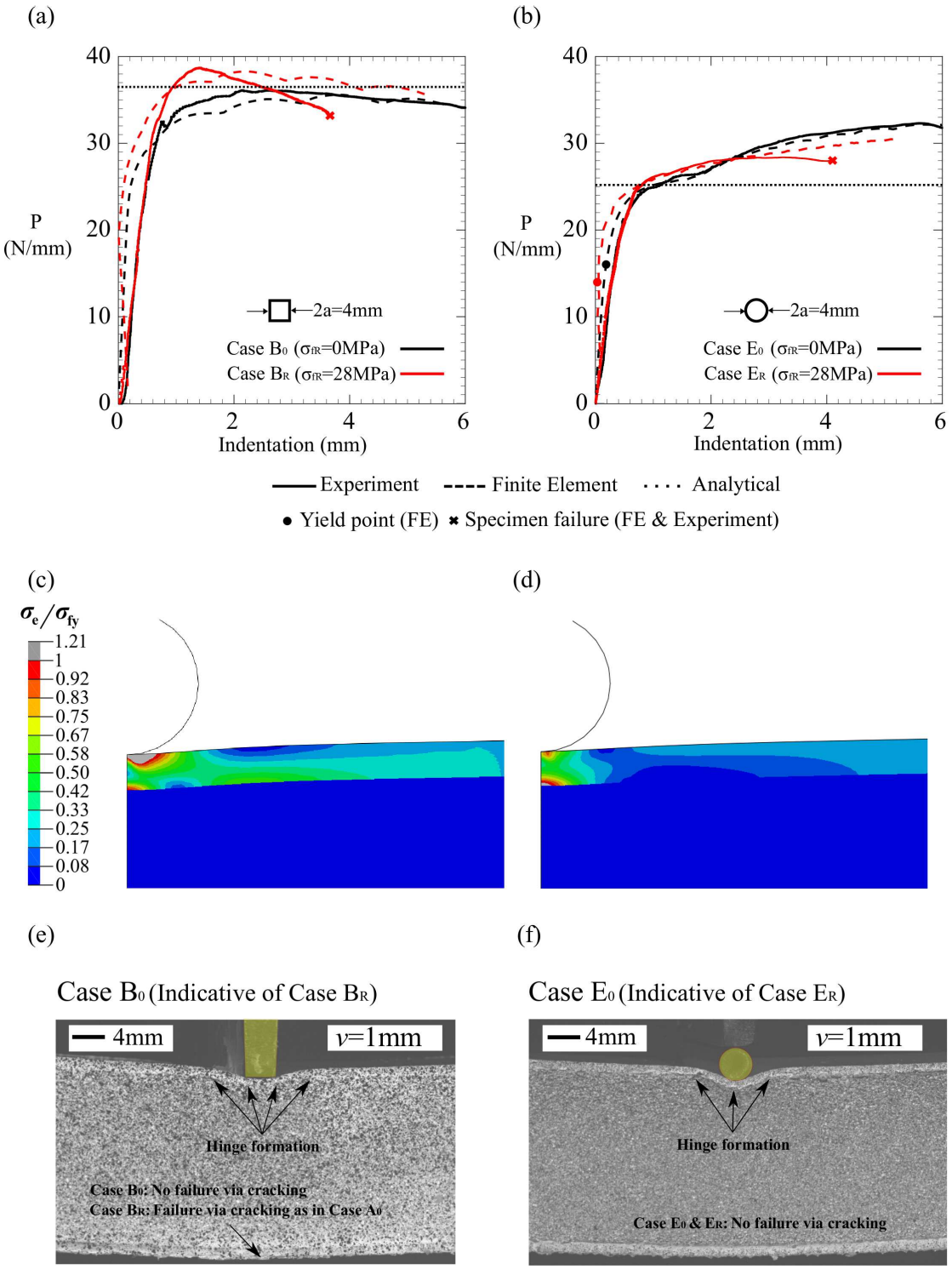

FIGURE 5.15: Comparison of the experimental, finite element, analytical load versus indentation responses for a prestresseed and non-prestressed elastic indentation specimen (a) flat indenter, (b) cylindrical indenter $D = 4mm$, and (c) cylindrical indenter $D = 19mm$.

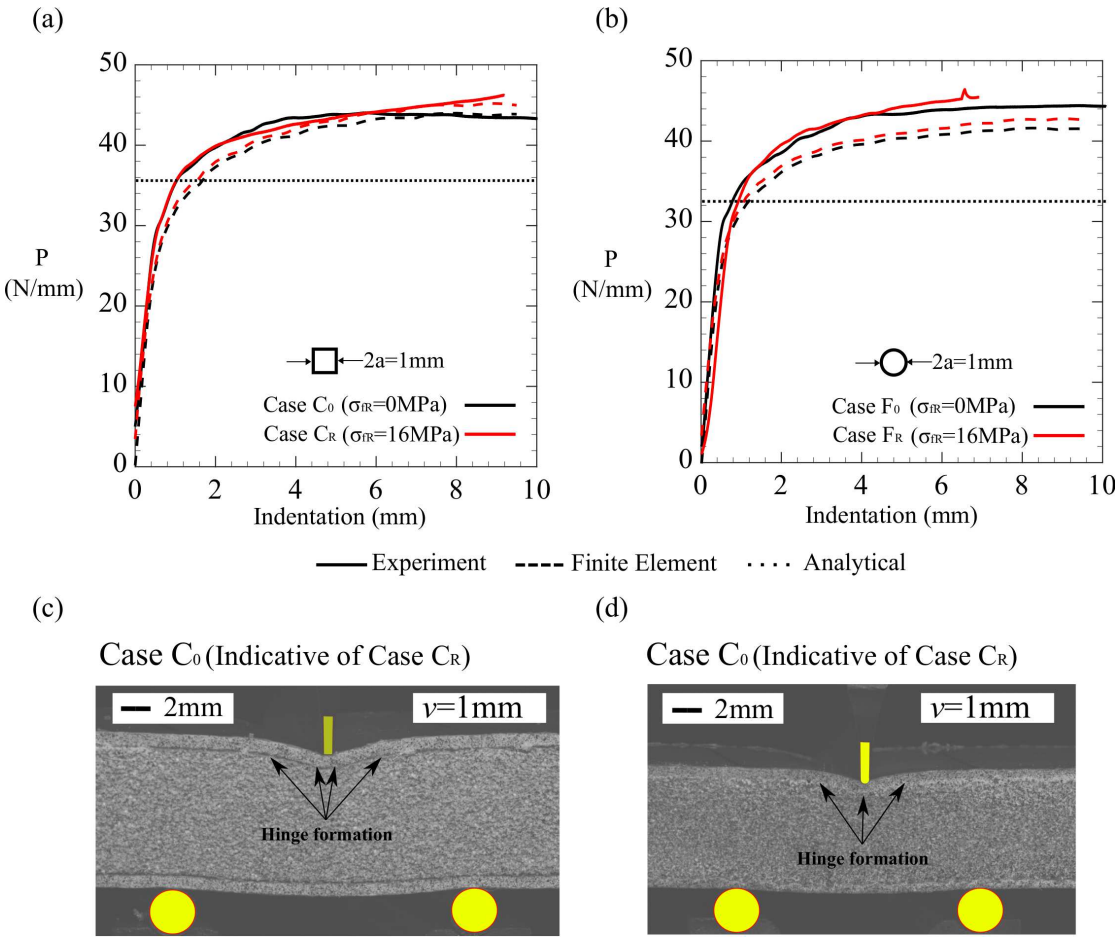

FIGURE 5.16: Comparison of the experimental, finite element, analytical load versus indentation responses for a prestresseed and non-prestressed plastic indentation specimen (a) flat indenter, (b) cylindrical indenter $D = 1mm$

residual stress present, and the shape and size of the indenter used during the three point bend experiment. There was difficulty in measuring the first yield of the sandwich beam during experiments; we observe that it is indeed possible to apply a residual stress to a sandwich panel and observe its effects on the peak collapse load, collapse behaviour and post-collapse and final failure. In lieu of experimental evidence we rely on finite element simulations to successfully validate the numerical models presented in this chapter.

The local indentation via first yield model described in this chapter considers the bending of a face sheet which is supported by a uniformly distributed load. This distributed load is defined by the yield strength of the foam. As with Chapter 4, if a residual stress is present in the core then earlier yielding of the beam will occur, which will directly

influence the calculated first yield load. If the core yield model (Section 5.2.3) was coupled with the first yield indentation model of the present chapter then a more accurate representation of the first yield load and first yield maps (shown in Figure 5.9) would be obtained. This is the main limitation of the present chapter, and provides a source of future work.

We have provided novel insight into the behaviour of sandwich panels under the action of residual stress whilst predicting the load and mechanism at which a sandwich beam exceeds the elastic limit. This is useful to the design engineer because it provides them with tools to predict either the onset of permanent deformation to the sandwich beam (if elastic-plastic face sheets are used) or the failure of sandwich beams (if elastic-brittle face sheets are used).

Part II

The indentation response of layered foam composites

Chapter 6

Indentation of a layer on foam substrate

Summary

The plane strain indentation response of a polycarbonate (PC) face sheet adhered to a polyvinyl chloride (PVC) foam substrate (on rigid foundation) is measured. Part I of this study considers the indentation of the bi-layer when it is resting on a rigid foundation and uses experimental and numerical methods to probe the deep indentation and final failure of such a configuration. The deformation mode involves foam crushing, and membrane stretching of the PC layer at large indenter displacements; this is quantified using optical strain measurement techniques. The bottom corners of the foam substrate lifts off its underlying support when the foam layer is sufficiently thin. Peak load is dictated by tensile failure of the foam on the bottom of the bi-layer. Finite element simulations suggest that a deep foam core prevents this lift-off and results in a greater load carrying and energy absorption capacity. Part I acts as a basis for Part II where the indentation response is considered for a bi-layer when it is rigidly attached to the foundation. The effects of indenter size and shape (flat-bottom punch versus cylindrical roller) and of specimen length upon the collapse response and failure mechanisms are also explored. The deformation response is modelled by finite element simulations and,

together with the observations, a simplified analytical model is synthesised. The model assumes elastic membrane stretching of a face sheet on an elastic, perfectly-plastic foam foundation, and includes the role of shear lag between face sheet and foam substrate. The study ends with a comparison of the indentation response for a face sheet on foam substrate with that of a sandwich beam in 3-point bending. It is found that membrane stresses do not develop in the face sheet for the case of 3-point bending, and consequently the indentation response has negligible hardening post yield. An analytical model is developed to give direct insight into this alternative collapse mechanism.

6.1 Introduction

Polymeric foams typically exhibit a low ductility in tension (of only a few percent), but a high ductility in compression due to the formation of crush bands (Andrews et al. (1999); Gaitanaros and Kyriakides (2015); Jang and Kyriakides (2009)). The indentation strength of polymeric foams is comparable to their uniaxial yield strength due to the volumetric compressibility of the foam, and the indentation strength is only mildly sensitive to the indenter geometry, see (Andrews et al. (2001); Flores-Johnson and Li (2010); Olurin et al. (2000); Onck et al. (2001)). For the practical application of foams to design for protective, energy absorbing packaging and for crash mitigation, it is desirable to enhance the indentation resistance of a foam substrate by the addition of a suitable face sheet.

The combination of a foam core and a stiff, strong face sheet commonly arises in sandwich construction: two stiff and strong face sheets are separated by a lightweight foam core. Sandwich panels are commonly used in flexural applications due to their low mass yet high stiffness and strength in bending. The early stage of plastic collapse of sandwich panels occurs by one of at least three competing mechanisms: face yield, core shear, and indentation (Ashby et al. (2000); Steeves and Fleck (2004b)). The present experimental and theoretical study gives additional insight into the indentation mode of collapse, and addresses the case where indent depths exceed the face sheet thickness

such that the face sheet undergoes membrane action prior to failure. This regime is of high practical significance; yet it has received little attention in the literature.

Our primary study is concerned with the plane strain indentation response of a single PC face sheet bonded to a PVC foam substrate upon a rigid foundation. PC is chosen due to its high tensile strength and ductility, and it finds common use in impact-resistant transparent components such as masks for eye protection. Our study complements the experimental investigation of Mohan et al. (2007): they observed a significant elevation in the axisymmetric indentation strength of a metallic foam due to the presence of a stainless steel face sheet.

Part I

Part I of this study considers the indentation response of a PC/H80 PVC foam bi-layer when it is **resting** on a rigid foundation and uses experimental and numerical methods to probe the deep indentation and final failure of such a configuration.

6.2 Experimental methods

The specimens consisted of Diab Divinycell H80 PVC closed cell foam core and a Lexan 9030-112 polycarbonate top sheet, bonded together by Loctite 401 low viscosity and fast curing, cyanoacrylate adhesive. The nominal compressive stress-strain curves of the foam and tensile stress-strain curves of the PC were measured and are shown in Figures 6.1(a) and (b), respectively. The responses are found to be relatively independent of strain rate in the range $10^{-4}s^{-1}$ to $10^{-2}s^{-1}$. The face sheet thickness was $t = 1$mm, the foam foundation thickness was $c = 50$mm, and both were of width $b = 25$mm. The overall specimen length was $L = 150$mm; the test setup is shown in Figure 6.1(c). The Aramis 3D Digital Image Correlation (DIC) system produced by GOM GmbH was used to visualise the strain field on the specimen during an indentation experiment. Prior to testing, a white spray paint base coat was applied to the

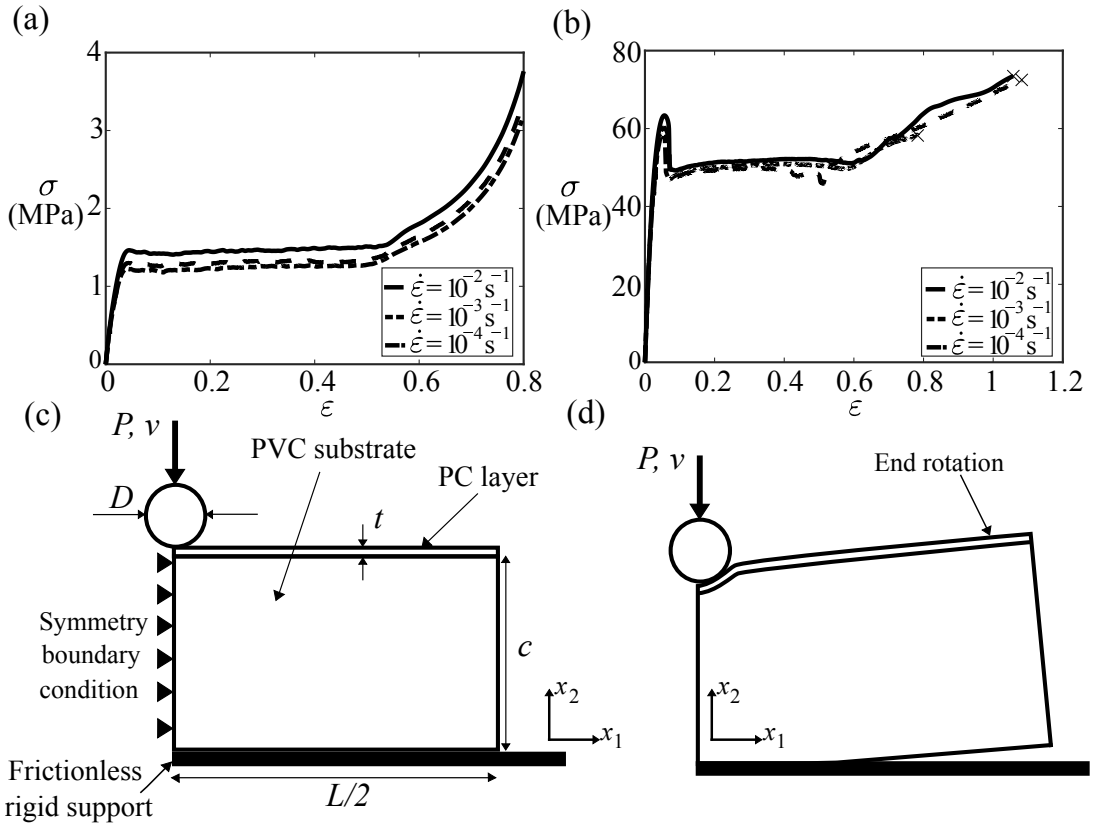

FIGURE 6.1: (a) Nominal uniaxial compressive stress strain response for Divinycell H80 foam. (b) Nominal uniaxial tensile stress strain response for Lexan PC. (c) Numerical and experimental test geometry. (d) Schematic of specimen rotation during indentation.

specimen followed by a fine black speckle pattern. The images taken during the experiments were correlated using the GOM Correlate software. The specimen was placed on a rigid, PTFE coated platen within a screw driven tensile test machine. A silver steel cylindrical roller of diameter, $D = 2$mm and length $b = 25$mm, was used to indent the specimen at a cross-head displacement rate of 1mm/min. In addition, an indentation test was conducted on a foam substrate absent the PC layer. This was done for comparison purposes and all other experimental parameters were held fixed.

6.3 Numerical methods

The finite element (F.E.) package ABAQUS was used to predict the indentation response of the foam-PC bi-layer. A symmetrical 2D model with 4-node CPE4R plain strain elements was used. The post yield behaviour of the foam was implemented using the

crushable foam model in ABAQUS and the constitutive model for H200 PVC foam as described in Appendix A is adapted for H80 PVC foam. The PC face sheet yield surface was modelled using J2 flow theory. Both constitutive models for the face sheet and foam were calibrated using experimental uniaxial data, with the initial stress peak in PC stress strain curve neglected.

The indentation tests were modelled as follows. Frictionless contact was assumed between the specimen and the underlying rigid support. Likewise, the rigid roller was taken to be frictionless. The finite element idealisation is summarised in Figure 6.1(c). An additional F.E. study was conducted to explore the effect of foam depth and face sheet length upon the indentation response such that $t = 1$mm, $L = 1000$mm and $c = 1000$mm.

6.4 Results and discussion

Both measured and predicted load versus displacement curves are given in Figure 6.2(a). Consider first the polycarbonate/foam bi-layer; the initial response, up to a deflection of the thickness of the PC layer, is characterised by elastic bending of the face sheet, and elastic and plastic crushing of the foam core as described by Soden (1996). Subsequent indentation gave plastic crushing of the foam, and a combination of bending and axial stretching of the face sheet. The foam specimen (absent a PC face) is shown for comparison; it has a much lower load carrying capacity.

Introduce the (x_1, x_2) co-ordinate system as shown in Figure 6.1(d). Contours of strain components $(\varepsilon_{11}, \varepsilon_{22})$ from the DIC observations and F.E. simulations are compared in Figure 6.3. In broad terms, there is excellent agreement between prediction and observation. The PC face sheet is in a membrane state except directly below the indenter where it acquires the same curvature as that of the indenter. The foam directly beneath the indenter (and PC layer) acquires a large tensile strain component $\varepsilon_{11} \approx 0.4$ and a large crushing strain $\varepsilon_{22} \approx -1.8$. The experiments (and F.E. simulations) revealed that the outer bottom faces of the foam substrate lifted off from the rigid support, as sketched

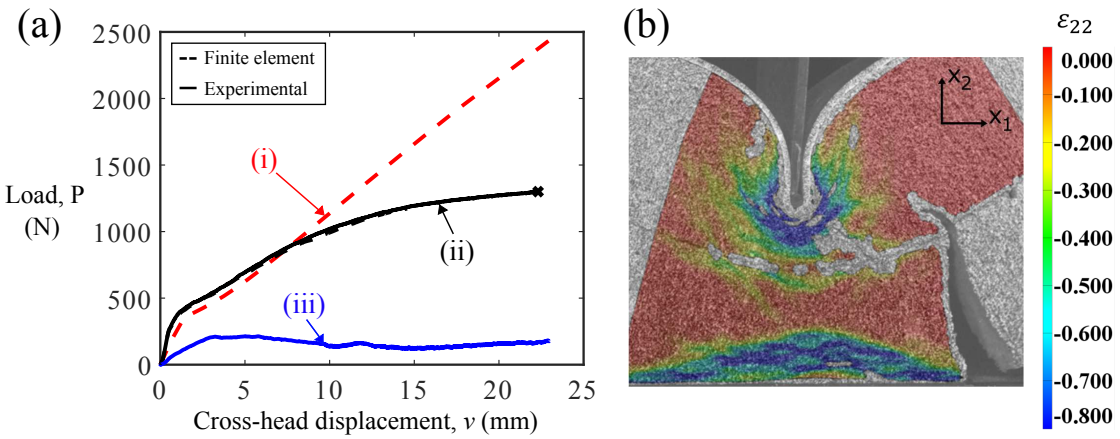

FIGURE 6.2: (a) Load versus displacement response for (i) PC layer and large foam substrate, (ii) PC layer and small foam substrate, and (iii) foam only. (b) DIC true strain contours (2-direction) showing failure mechanism of PC layer and small substrate.

in Figure 6.1(d). This may be explained as follows. The PC face sheet acquires the curvature of the roller indenter, and the underlying foam bends in a compatible manner. The hinging action results in eventual tensile failure of the specimen, with a crack initiating at the bottom of the specimen adjacent to the hinge and propagating up through the specimen, see Figure 6.2(b). The finite element model adequately captures both the load displacement response and the deformation profile, when compared to experiments. As a reference case, the case of a very large foam depth and large face sheet length was considered. Figure 6.2(a) shows a comparison of the indentation response for the small and large specimens. It is clear that the initial stiffness of the small foam specimen ($c = 50$mm and $L = 150$mm) exceeds that of the larger specimen, due to the fact that it is a thinner foam core. Membrane action of the PC face sheet develops for the large foam core and the indentation load increases with depth, see Figure 6.2(a). In contrast, the small foam core is unable to support membrane stress within the PC face sheet, and the alternative mode of lift-off leads to a smaller and saturated value of indentation load.

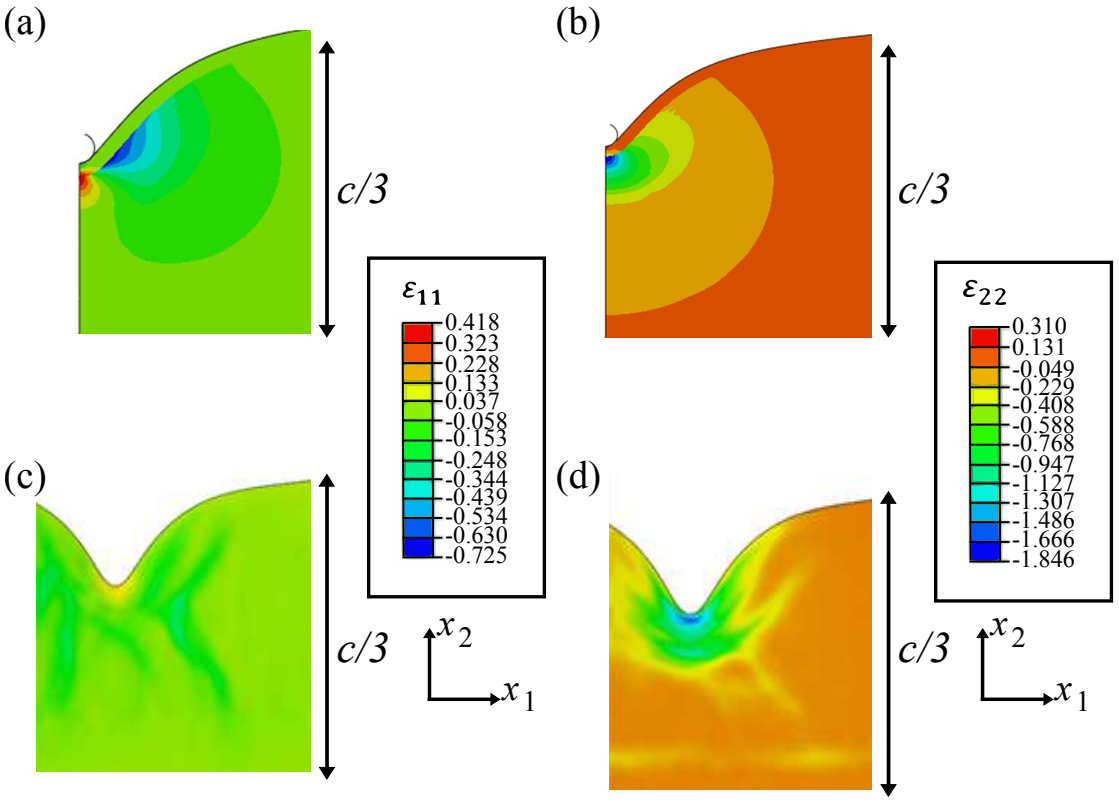

FIGURE 6.3: (a) Finite element predictions of true strain contours (1-direction) at $v =$ 10mm. (b) Finite element predictions of true strain contours (2-direction) at $v = 10$mm. (c) DIC true strain contours (1-direction) at $v = 10$mm. (d) DIC true strain contours (2-direction) at $v = 10$mm.

Part II

Part II addresses the indentation response of a PC/H200 PVC foam bi-layer **attached** to a rigid foundation. This study comprises an exploratory experimental study, accompanying finite element models, followed by an analytical treatment of the deep indentation problem. An analytical model for the deep indentation response of a sandwich beam in three point bending is also formulated and a subsequent comparison with the bi-layer response is given.

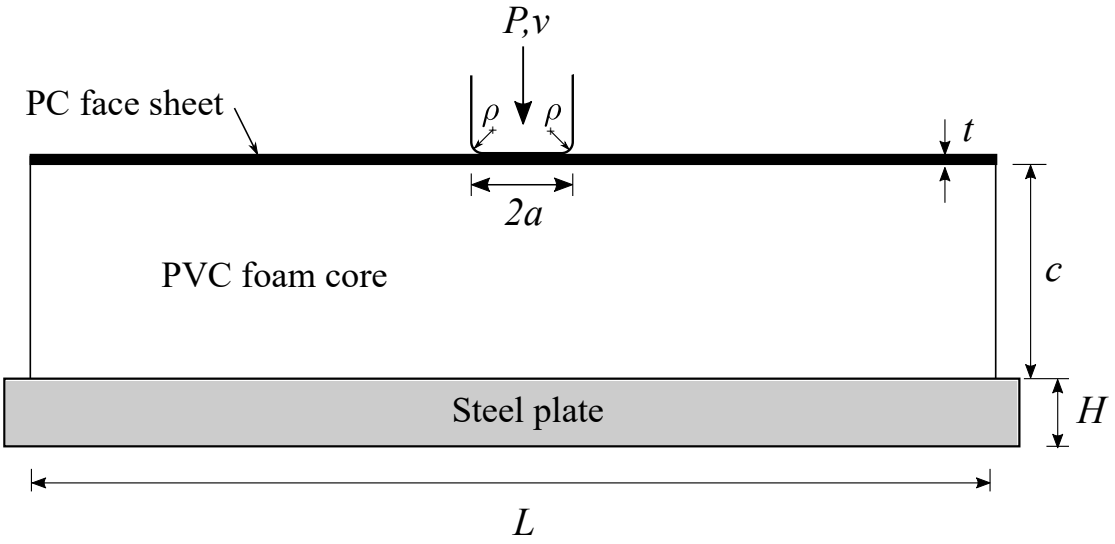

FIGURE 6.4: Geometry and loading in indentation tests.

6.5 Experimental methods

6.5.1 Test methods

The indentation test setup is sketched in Figure 6.4. The specimens comprised a DIAB Divinycell H200 PVC closed cell foam substrate and a Lexan 9030-112 PC top layer, bonded together by a cyanoacrylate adhesive. In all cases, the face sheet thickness was $t = 1$ mm, the foam substrate thickness was $c = 100$ mm; both were of depth $b = 25$ mm into the page. The bottom face of the PVC foam was bonded by the cyanoacrylate adhesive to a steel plate of sufficient thickness $H = 50$ mm that the plate behaves in a rigid manner relative to that of the foam and face sheet. The steel-backed specimens were placed on the loading platen of a screw-driven tensile test machine.

A series of indent tests are listed in Table 6.1, and were performed as follows:

I) An initial basic study whereby the bi-layer (on steel support) was indented by a flatbottom punch of width $2a = 4$ mm with a corner radius $\rho = 0.5$ mm, see Figure 6.4. The indent velocity was $\dot{v} = 0.025 mms^{-1}$, and the overall length of the specimen was $L = 400$ mm, as listed in Table 6.1. Additionally, an indentation test was performed on a foam substrate absent the PC layer to provide insight into the indentation response of a foam layer as the reference case.

II) The effect of indenter size (relative to face sheet thickness) was determined by employing 2 additional flat-bottom punches, of width $2a = 2$ mm and 10 mm, with corner radius $\rho = 0.5$ mm.

III) The sensitivity of indentation response to head shape was explored by performing tests at $\dot{v} = 0.025 mms^{-1}$ and $L = 400$ mm using circular rollers of radius $r = 1, 2, and 5$ mm.

IV) Rate sensitivity was determined by performing additional tests using the flat-bottom punch of width $2a = 4$ mm, and $\dot{v} = 0.0025 mms^{-1}$ and $0.25 mms^{-1}$.

V) The overall specimen length was decreased from $L = 400$ mm to $L = 50$ mm in order to determine the effect of specimen length on the development of membrane action in the facesheet. This test also made use of the flat-bottom punch of width $2a = 4$ mm, and an indent velocity of $\dot{v} = 0.025 mms^{-1}$.

In each case, 3 repeat experiments were carried out on each specimen. A 3D Digital Image Correlation (DIC) system was used to visualize and measure the surface strain field during the indentation tests. Prior to testing, a matt white spray paint base coat was applied to the specimen followed by a black paint to generate a fine black speckle pattern. The white base ensured that any reflections from variation in the texture of the underlying specimen were minimised, thereby allowing accurate tracking of the displacement of each black speckle. Images were acquired at a frequency of 0.33 Hz and a resolution of 4096 x 3072 pixels during the experiments; these images were subsequently used to produce the in-plane strain contour maps using the correlation software of the DIC system.

6.5.2 Test materials

The uniaxial tensile and compressive stress versus strain responses of the PC face sheet and of the PVC foam were measured; these are plotted as nominal (engineering) quantities in Figure 6.5. The initial response of PC is linear elastic with a Young's modulus $E_f = 2$ GPa, at a strain rate of $10^{-4} s^{-1}$. Tensile yield of PC occurs at $\sigma_{fy} = 62$ MPa;

TABLE 6.1: Geometry and experimental details for plane strain indentation tests. In all cases, t = 1 mm, c = 100 mm, andb = 25 mm.

		Specimen	a (mm)	r (mm)	$\dot{v}$ (mm/s)	L (mm)
Basic study	I	Medium punch on PC/PVC foam bi-layer	2	-	0.025	400
		Medium punch on PVC foam layer	2	-	0.025	400
Indenter study	II	Small roller	-	1	0.025	400
		Medium roller	-	2	0.025	400
		Large roller	-	5	0.025	400
	III	Small punch	1	-	0.025	400
		Medium punch	2	-	0.025	400
		Large punch	5	-	0.025	400
Rate study	IV	Low rate	2	-	0.025	400
		High rate	2	-	0.025	400
Length study	V	Short specimen	2	-	0.025	50
		Long specimen	2	-	0.025	400

this is followed by a load drop to 52 MPa and a subsequent drawing of the material (accompanied with mild strain hardening) until tensile fracture occurs at a nominal strain value of $\varepsilon \approx 1.15$. In compression, PC has a yield strength of 81 MPa. A strong strain-hardening behaviour is observed at a nominal compressive strain above 0.2, see Figure 6.5(a).

The nominal stress versus nominal strain response of PVC H200 foam is shown in Figure 6.5(b). The Young's modulus of the foam is $E_c = 125$ MPa, based on the measured

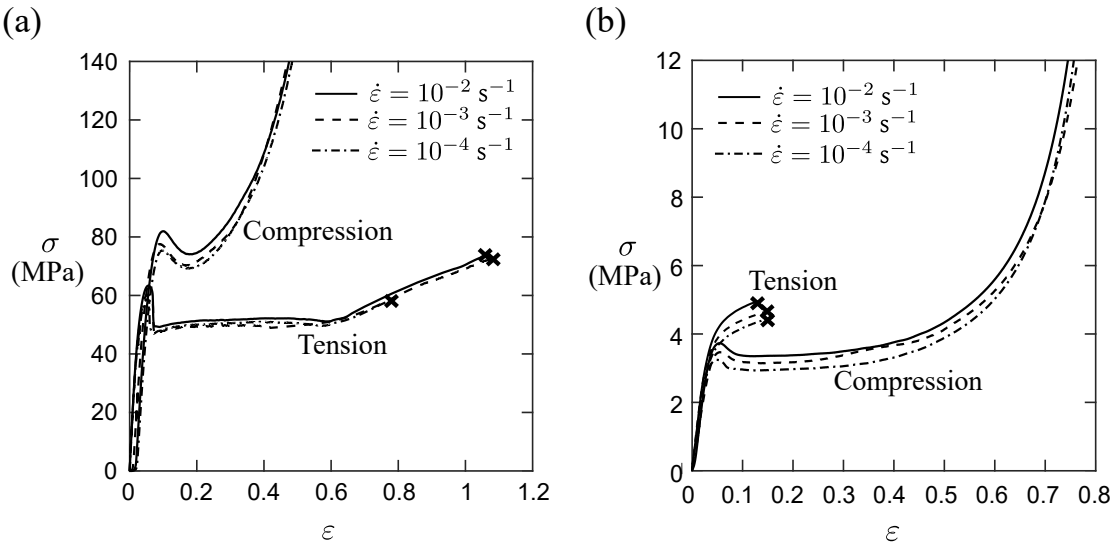

FIGURE 6.5: Nominal tensile and compressive responses for (a) polycarbonate and (b) H200 PVC foam for strain rates of $10^{-4}s^{-1}, 10^{-3}s^{-1}$, and $10^{-2}s^{-1}$. Cross marks indicate failure.

responses at a strain rate of $10^{-4}s^{-1}$. Tensile fracture of the foam occurs at $\varepsilon \approx 0.14$ and at an ultimate tensile strength (UTS) of approximately 4.7 MPa for all values of strain rate shown in Figure 6.5(b). The compressive yield strength of the PVC foam (at onset of yield) is $\sigma_{cy} = 3.2$ MPa, with progressive strain-hardening of the foam evident at nominal compressive strains greater than 0.1. The responses of PC and PVC are only mildly sensitive to strain rate in the range $10^{-4}s^{-1} to 10^{-2}s^{-1}$, see Figure 6.4(a) and (b).

6.6 Finite element analysis

Quasi-static finite element (FE) calculations were performed within ABAQUS/Explicit v6.14 to simulate the indentation response of the PC/foam bi-layer, and to aid interpretation of the experimental results. Thus, it is appropriate to outline the FE analysis prior to reporting the indentation results.

The FE mesh for both the PC face sheet and PVC foam substrate comprised of linear quadrilateral elements in plane strain (type CPE4R). Perfect adhesion was assumed between the face sheet and foam substrate. The loading punch (and roller) were modelled as rigid surfaces, and a frictionless contact was assumed between the punch and the face sheet. A graded FE mesh was employed to provide adequate resolution close to the

punch. The face sheet had 10 elements across its section to capture the bending stress field; a sensitivity study was performed to ensure that this mesh refinement was adequate to give a converged indentation load versus displacement response. A symmetric half model was employed in the FE study with the bottom edge of the core fixed and the loading punch (and roller) prescribed with a vertical downward velocity.

The PC face sheet was modelled as an isotropic, rate-independent, von Mises solid with a true stress versus true strain response as shown in Figure 6.6(a). This curve is derived from the measured response of PC face sheet in uniaxial tension (at a strain rate of $10-4s-1$) upon assuming a bi-linear fit for the post-yield nominal stress versus nominal strain data of Figure 6.5(a). The elastic modulus and Poisson's ratio are taken as $E_f =$ 2 GPa and $\nu_f = 0.3$, respectively, based on the measured values in uniaxial tension. The PVC foam is specified with an elastic modulus $E_c = 125$ MPa and Poisson's ratio $\nu_c = 0.3$. The post-yield behaviour of the foam was modelled using the crushable foam model in ABAQUS which allows for a dissimilar response of the foam in tension and compression; a detailed description of the constitutive model is given in Appendix A. The assumed uniaxial compressive response of the foam is plotted in Figure 6.6(b); this curve is a smooth spline fit of the measured response in uniaxial compression (at a strain rate of $10-4s^{-1}$) upon excluding the stress peak at the onset of yield. A perfectly-plastic response is assumed for foam under tension via a constant parameter k_2 as explained in Appendix A. For a choice of $k_2 = 2.2$, the uniaxial tensile yield strength from the FE simulation agrees with the measured uniaxial tensile strength (of 4.7 MPa) to within 3%, and this value is employed in all the FE simulations. Failure of PC and PVC was not included in the FE model. Rate sensitivity was also neglected for both PC and PVC.

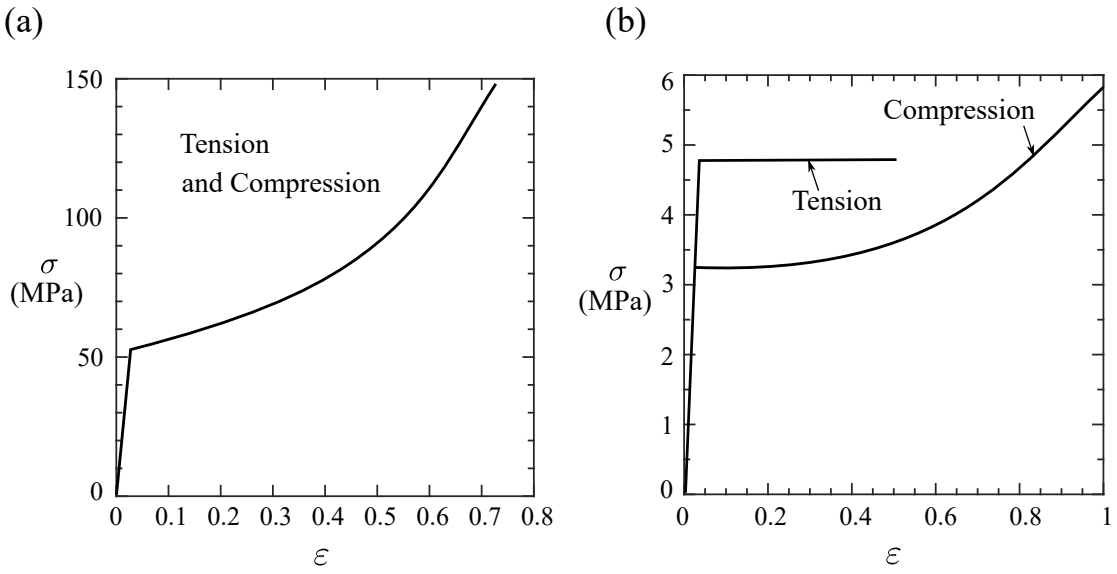

FIGURE 6.6: Uniaxial true stress versus logarithmic strain responses for the FE simulations: (a) PC face sheet and (b) PVC H200 foam core.

6.7 Experimental results and interpretation by finite element predictions

6.7.1 Indentation by flat-bottom punch

The indentation responses are compared in Figure 6.7(a) for a PC/foam bi-layer ($t = 1$ mm, $c = 100$ mm, $L = 400$ mm) and for a foam layer absent the PC top layer; in both cases the flat bottom punch of $2a = 4$ mm was used at an indentation speed of $\dot{v} = 0.025 mms^{-1}$, as listed in the basic study I of Table 6.1. Measurements are displayed in Figure 6.7(a) for the 3 repeat tests and reveal minimal scatter. Predictions from the FE calculations are included in Figure 6.7(a) and they show good agreement with the measured indentation responses for both the bi-layer and the foam layer.

The presence of the PC face sheet has a major effect upon the initial collapse load and the subsequent hardening response, as follows. We shall show below that, for the case of the PC/foam bi-layer, the high hardening rate is due to the development of tensile membrane stresses in the PC layer (first elastic stretching and then plastic stretching). It is less obvious why the indentation of an elastic, almost perfectly-plastic foam substrate (absent a PC top layer) leads to the strong hardening observed in Figure 6.7(a). An

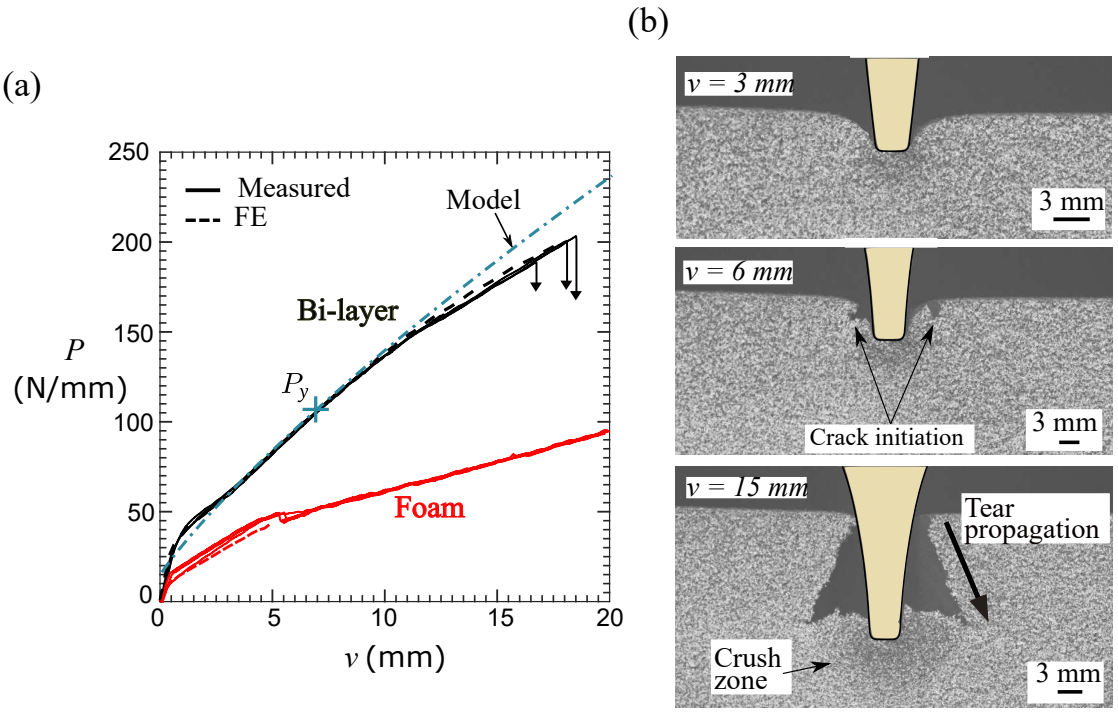

FIGURE 6.7: Indentation response of PC/foam bi-layer and foam layer (Study I): (a) Load versus displacement response and (b) Observed damage progression in the foam.

explanation is found in the fact that the foam cracks into a wedge-shaped crush zone beneath the indenter, see Figure 6.7(b). With increasing indent depth, the width of the crush zone increases in a linear fashion, and, upon assuming a constant magnitude of the local crush strength, the load increases with depth in a linear fashion. The measurements of Figure 6.7(a) support this interpretation. We note in passing that there is a small discontinuous drop in load when a crack nucleates and propagates into the foam at an indentation depth of approximately 5 mm.

The measured load versus displacement response of a representative PC/foam bi-layer is replotted in Figure 6.8(a) from the data of Figure 6.7(a), along with the analytical prediction of Soden (1996) for indentation of an elastic beam on a rigid, perfectly-plastic foundation. There is adequate agreement between the Soden (1996) prediction and the initial post-yield response of the bi-layer. However, this analytical prediction becomes inadequate once $v > t = 1$ mm. We shall now show from DIC measurements and FE calculations that face sheet membrane stresses dominate the indentation response at deep displacements of the indenter relative to the face sheet thickness, and this is the root cause of the strong hardening behaviour.

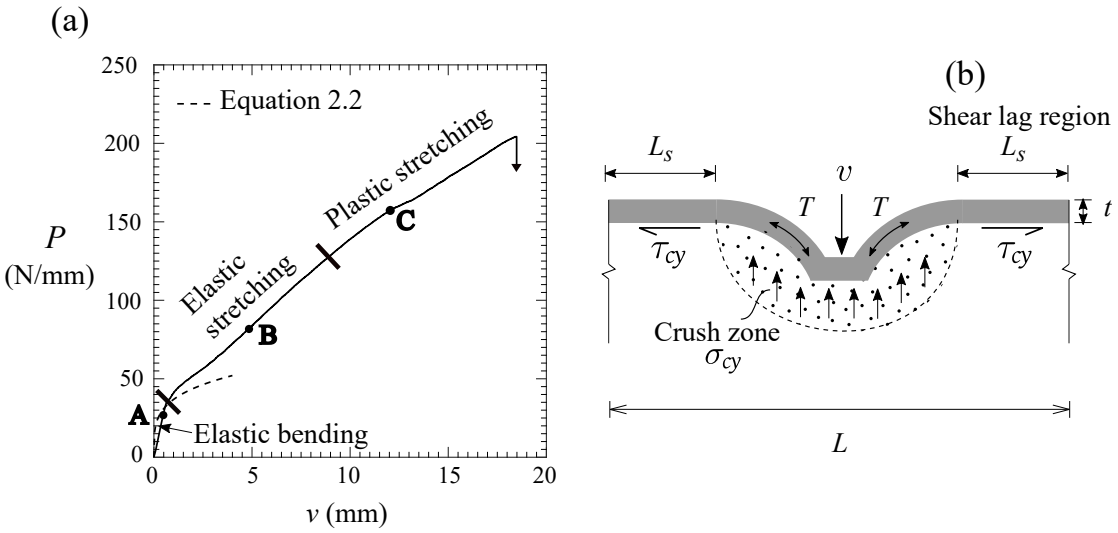

FIGURE 6.8: (a) Indentation response of PC/PVC foam bi-layer (Study I). The boundary between elastic bending and elastic stretching at $v = 0.6$mmand the boundary between elastic stretching and plastic stretching at $v = 8$mm are taken from the corresponding FE solution of Fig. 4a. (b) Stretching of the face sheet during deep indentation.

In order to gain further insight into deep indentation, the distribution of von Mises strain ε_e (logarithmic) within the PC layer is determined by both DIC and FE analysis, for the bilayer specimen of Figure 6.8(a) at 3 stages of indentation: (A) $v = 0.5$ mm, (B) $v = 5$ mm and (C) $v = 12$ mm. These 3 values are marked in Figure 6.8(a) and the strain distributions ε_e are given in Figure 6.9. There is general agreement between the observed contours of strain from DIC and the FE prediction. The following broad remarks can be made from Figure 6.8(a) and Figure 6.9, taken together.

Load case A: At displacements $v >> v = 1$ mm, the face sheet bends elastically with negligible membrane action, whilst the foam compresses in an elastic manner. Under increasing indentation, but $v/t < 1$, the foam substrate yields within a crush zone beneath the punch while the PC face sheet bends elastically, as idealised by Soden (1996). Yielding of the core in the FE simulations occurs at an indentation depth $v = 0.5$ mm, labelled as point A in Figure 6.8(a); the corresponding strain profile in the face sheet is shown in Figure 6.9.

Load case B: When the displacement v is on the order of (or exceeds) the face sheet thickness t, the face sheet stretches elastically in addition to bending (in a plastic manner) while the foam continues to compress in a plastic manner within the crush zone, as

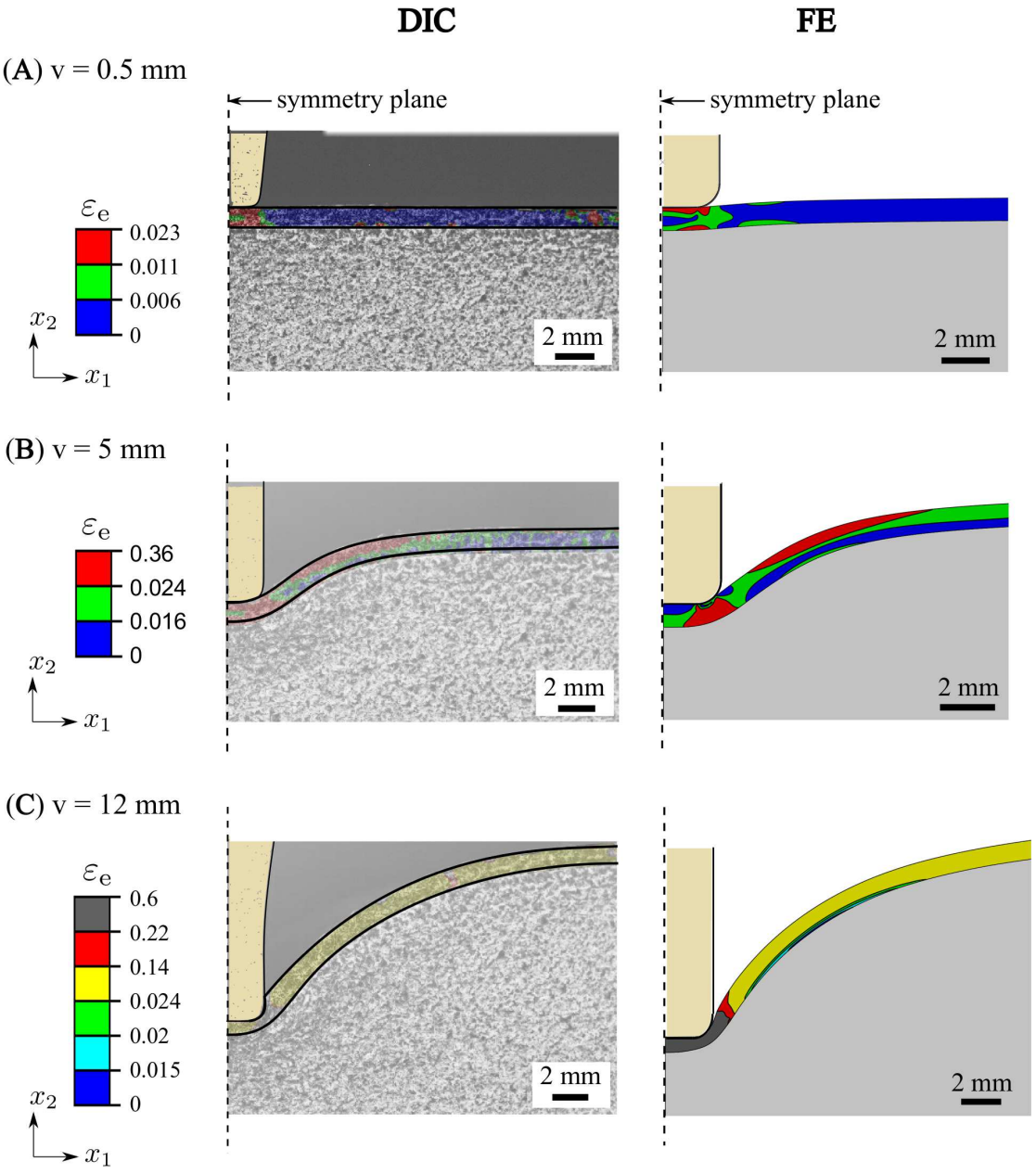

FIGURE 6.9: Contours of von Mises strain in the PC face sheet of the bi-layer at increasing values of indent depth (Study I), at loads A, B, and C as marked in Figure 6.8(a).

sketched in Figure 6.8(b). The strain profile in face sheet at point B corresponding to $v = 5$mm is shown in Figure 6.9. The face sheet has an almost constant curvature adjacent to the indenter and it carries a tensile load of magnitude T, as labelled in Figure 6.8(b).

Load case C: At displacements $v/t >> 1$, the tensile membrane stresses in the face sheet attain yield magnitude. With continued indentation, PC layer undergoes plastic stretching, and the magnitude of the plastic strain increases with increasing v. The deformed profile of the face sheet at point C (corresponding to $v = 12$ mm) resembles that of Figure 6.8(b), except $T = T_u = \sigma_{fy}t$ for this case. The strain profile recorded from the DIC is shown in Figure 6.9 along with the FE prediction. Recall that the logarithmic failure strain of the PC (about 0.76) significantly exceeds that of the foam (about 0.13), and consequently the foam cracks adjacent to the stretched PC layer leading to a drop in the load at $v = 18.5$ mm.

6.7.2 Role of indenter geometry

A comparison of the measured load P versus displacement v response of the PC/foam bilayer is given in Figure 6.10(a) for the flat-bottom punches and circular rollers, at an indentation speed of $0.025 mms^{-1}$; these are cases II and III of Table 6.1. Scatter was minimal and so only a representative P versus v response is shown in Figure 6.10(a). The predictions from the FE calculations are included in Figure 6.10(a) and they show good agreement with the measured response for each case. We note from Figure 6.10(a) that the P versus v responses are almost parallel for the flat-bottom punches and circular rollers, with an increase in load (for a given indent depth) with increasing a/t or r/t. In the flat-bottom punch tests, the peak load is dictated by cracking of the underlying foam, followed by shear-off of the PC from the corners of the punch, see Figure 6.11(a) and (b). The failure mode for the small circular roller is similar to that of the flat-bottom punch, see Figure 6.11(c). In contrast, at high r/t, first failure is by tensile cracking of the foam at the edge of the indentation zone, as shown in Figure 6.11(d). Punch velocity has only a minor effect upon the indentation response (study IV of Table 6.1), as shown

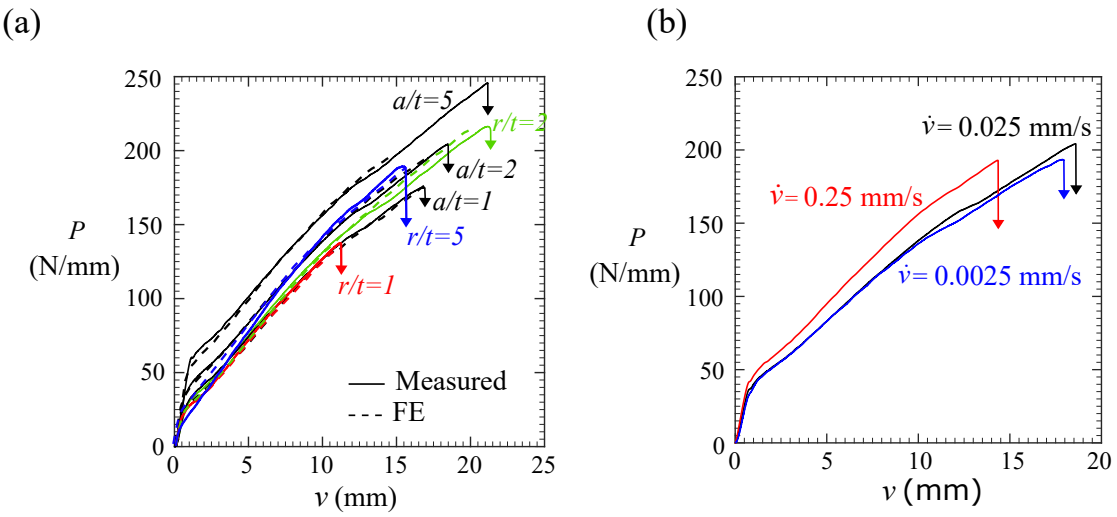

FIGURE 6.10: (a) Load versus displacement response for (i) flat-bottom punch, width $a = t = 1;2;5$ (Study II) and, (ii) cylindrical roller, radius $r/t = 1;2;5$ (Study III) at an indentation speed $\dot{v} = 0.025s^{-1}$, (b) Load versus displacement response for flat punch indentation $(a/t = 2)$ at selected indentation speeds (Study IV).

in Figure 6.4(b) for the flat-bottom punch of $a/t = 2$. This is attributed to the small strain rate sensitivity of both the PC face sheet and PVC foam.

6.7.3 Role of specimen length

The ability to develop membrane stresses relies upon load transfer between the face sheet and core over a shear lag zone adjacent to the crush zone, as sketched in Figure 6.8(b). Assume that the foam exerts a shear traction on the PC face sheet of magnitude equal to the shear yield strength τ_{cy} of the foam. Then, the length of shear lag zone L_s in order to develop a membrane tension T in the PC face sheet equal to its yield value $T_u(=\sigma_{fy}t)$ is $L_s = \sigma_{fy}t/\tau_{cy} = 19$ mm for τ_{cy}. We anticipate that membrane stress is not able to develop to full extent when the semi-length of the bi-layer specimen is much less than this shear lag length. In order to confirm this, tests (of type V in Table 6.1) were performed on specimens of length $L = 50$ mm and 400 mm, using a flat-bottom punch of width $a/t = 2$, see Figure 6.12. The initial indentation response is almost insensitive to the magnitude of L for shallow indents such as $v < 2$ mm. However, at deep indents, such as $v > 5$ mm, the indentation load (at a given indent depth) for a specimen of $L = 50$ mm is significantly below that for $L = 400$mm. An analytical model is now developed,

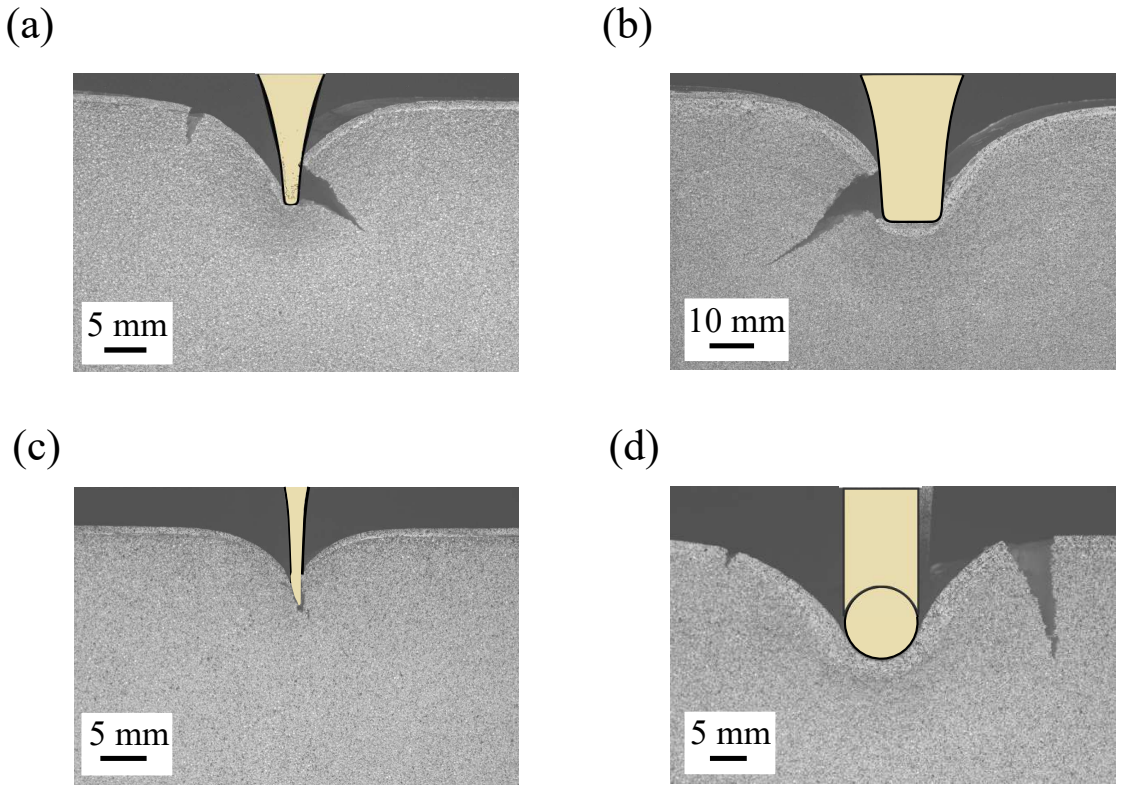

FIGURE 6.11: Observed failure modes in the indentation of bi-layer with flat bottom punches of (a) $a/t = 1$ at $v = 16.7$ mm, (b) $a/t = 5$ at $v = 21.2$ mm, and with cylindrical rollers of (c) $r/t = 1$ at $v = 11.5$ mm and (d) $r/t = 5$ at $v = 15.8$ mm.

based on the existence of the shear lag zone in order to predict the deep indentation resistance of the bi-layer.

6.8 Analytical model

Existing models for the indentation of sandwich beams assume that the indent depth is sufficiently small such that the face sheet behaves in a bending manner with negligible membrane action. In the present study, the indent depth increases to more than the face sheet thickness, and so significant membrane stresses develop in the face sheet: a new model is needed to account for this mode of deformation.

Consider plane strain indentation of a face sheet and underlying foam core by a flat-bottom punch of width $2a$, as shown in Figure 6.13(a). The face sheet is an elastic, perfectly-plastic solid, of plane strain Young's modulus E_f, tensile yield strength σ_{fy}

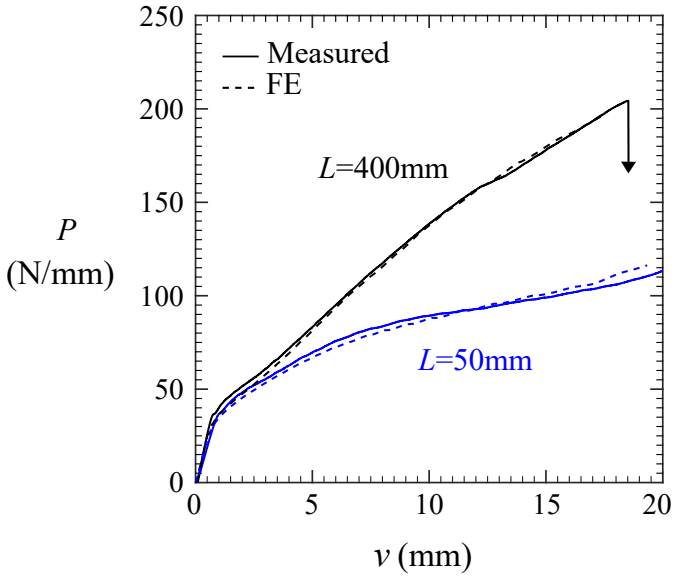

FIGURE 6.12: Effect of specimen length on the indentation response of bi-layer (Study V).

and thickness t. It is perfectly adhered to a semi-infinite foam substrate. The foam core is treated as an elastic, perfectly plastic solid of plane strain Young's modulus E_c , and compressive yield strength σ_{cy}.

The above experiments and FE analysis both suggest the following overall deformation mode. Assume that the face sheet develops a purely membrane state with a line tension (per unit length into the page), $T(x) = \sigma_f(x)t$ where $\sigma_f(x)$ is the tensile axial stress at any location x in the current configuration, see Figure 6.13(b). There are two distinct zones:

1. an outer shear lag zone whereby the tension in the elastic face sheet drops with increasing x by the presence of a shear stress $\tau(x)$ on its lower face (adhered to the elastic foam substrate). This outer zone starts at a distance s from the centre line, see Figure 6.13(b).

2. an inner zone of core crush such that the foam core exerts a compressive normal traction of magnitude σ_{cy} on the underside of the face sheet in the deformed configuration. Since the shear traction of the foam core on the face sheet is negligible in this zone (of width $2s$) the tension $T(x)$ is uniform within this zone, and we

write $T(x) = T_u$ for $a < |x| < s$. Force equilibrium of the membrane dictates that its radius of curvature R is given by

$$R = \frac{T_u}{\sigma_{cy}} \tag{6.1}$$

and we conclude that R is constant. Thus, the face sheet adopts the profile of a circular arc. We shall assume initially that the face sheet is elastic, but later extend our solution to the case where the face sheet yields at an axial tension $T_u = T_y$.

6.8.1 Indentation with elastic stretching of the face sheet

The core crush zone: Consider indentation to a depth v by the flat-bottom punch (of corner radius $\rho << a$). The load P is obtained by invoking vertical equilibrium to give

$$P = 2\sigma_{cy}(Rsin\omega + a) \tag{6.2}$$

Where ω is the inclination of the face sheet adjacent to the punch, as defined in Figure 6.13(a). Geometry dictates that

$$v = R(1 - cos\omega) \tag{6.3}$$

and

$$s = Rsin\omega + a \tag{6.4}$$

It remains to solve for R or equivalently the magnitude of T_u within the core crush zone, recall Equation 6.1. To proceed, we turn our attention to the outer shear lag zone in order to solve for T_u.

Formulation for the outer shear lag zone: The membrane force T_u is resisted by both the face sheet and the underlying elastic core, and gives rise to an inward displacement u

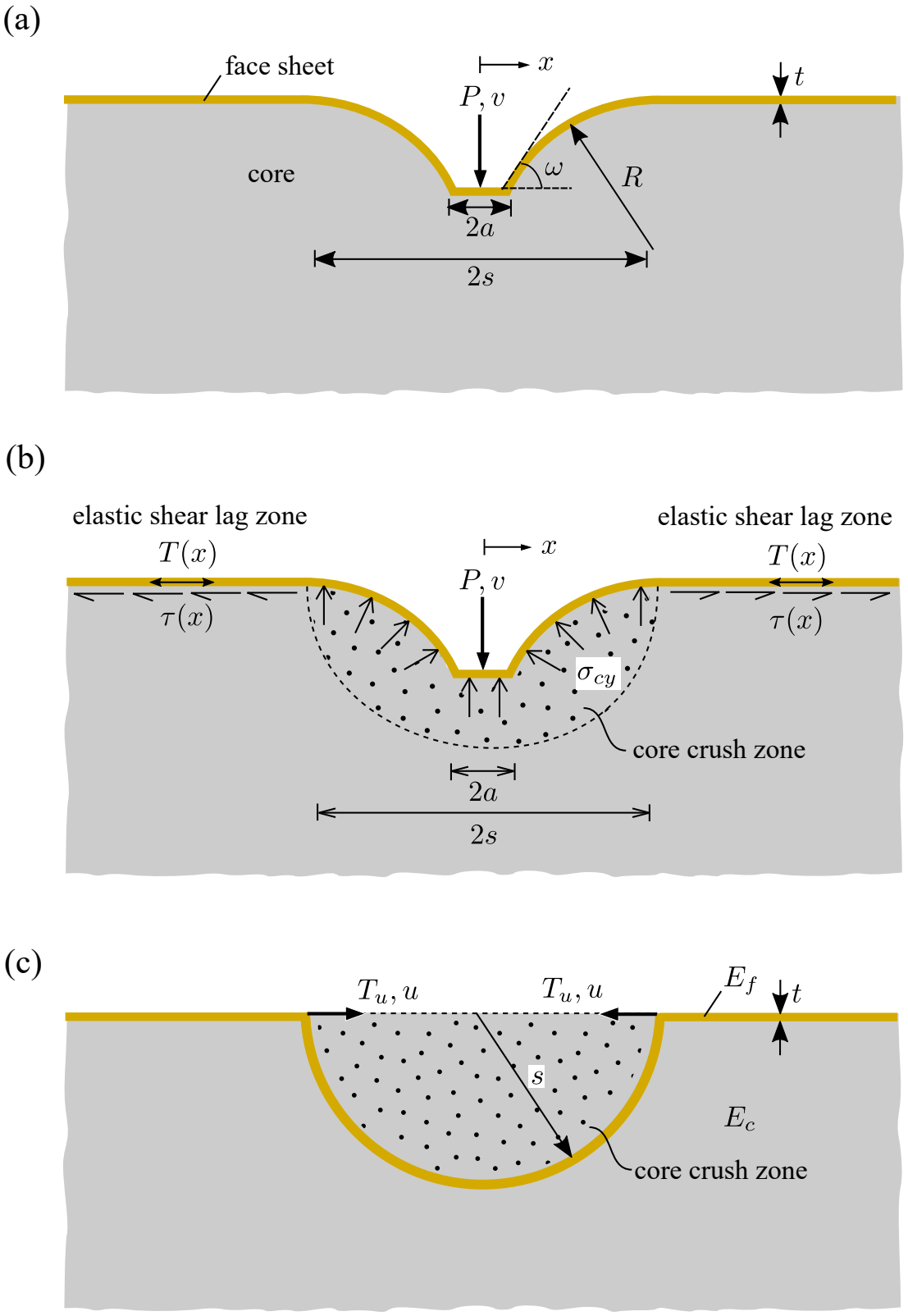

FIGURE 6.13: Indentation of a face sheet attached to a foam core: (a) geometry and loading, (b) stress state in the face sheet and core under the applied loading, and (c) geometry and loading for the subsidiary problem of determining the elastic spring stiffness in the shear lag zone.

at the boundary $x = \pm s$ between core crush zone and outer shear lag zone, see Figure 6.13(c). This subsidiary problem gives us the spring constant k where

$$T_u = ku \tag{6.5}$$

First, we complete our analysis and then we present a finite element solution for the subsidiary problem of evaluation of k. We assume that the face sheet remains bonded to the foam core, with vanishing slip, and that it undergoes negligible straining directly beneath the punch. At any indentation depth v, the face sheet elongates by 2χ over its length, where

$$\chi = \frac{T_u}{E_f t} R\omega + u \tag{6.6}$$

Upon comparing the initial and final configurations, χ is also given by

$$\chi = R\omega - Rsin\omega \tag{6.7}$$

Now, substitute Equations 6.1, 6.5 and 6.7 into 6.6 to obtain

$$\omega - sin\omega = \left(\frac{R\omega}{E_f t} + \frac{1}{k} \right) \sigma_{cy} \tag{6.8}$$

We emphasize that $k = k(s)$, and it is still to be found. Treat ω as the independent variable. Then, R is an implicit function of ω, and iteration is needed to solve Equation 6.8 for R as a function of ω. After obtaining $R(\omega)$ we solve for the load $P(\omega)$ via 6.2, and thereby determine $v(\omega)$. The effective stiffness $k(s)$ is now obtained by solving a subsidiary problem using finite element analysis.

Finite element estimate for the spring stiffness k: The spring stiffness $k(s)$ in the outer shear lag region is estimated from the response of a force dipole of magnitude T_u in the face sheet, separated by a distance $2s$, as shown in Figure 6.13(c). The face sheet

and the core in the outer shear lag region are assumed to behave as elastic solids with plane strain moduli E_f and E_c, respectively. The portion of the core within the crush zone has negligible stiffness and this is accounted for by the removal of a semi-circular portion of radius s from the core, as shown in Figure 6.13(c).

The FE calculations are performed using ABAQUS Standard (v6.14). Symmetry boundary conditions applied to one half of the FE model are shown in Figure 6.14(a). A 2D FE mesh is generated with ten 8-noded biquadratic plane strain elements (type CPE8R) along the thickness of the face sheet. A horizontal displacement u is applied to the vertical edge of the face sheet, and the value of the spring stiffness $k = T_u/u$ is computed for selected values of $E_f t/E_c s$ in the range of 0.1 to 10. A regression analysis for values of core depth $c \geq 10E_f t/E_c$ and specimen length $L \geq 2s + 10E_f t/E_c$ reveals power-law scaling between the spring constant k and $(E_f, E_c, t, s)$of the form

$$k = \beta E_c \left(\frac{E_f t}{E_c s}\right)^{1/3} \tag{6.9}$$

where $\beta = 0.36$, see Figure 6.14(b).

The dipole problem considered above additionally informs us of the length of shear lag zone. The shear traction $\tau(\chi)$ along the face sheet decays quadratically with distance χ in the far-field region($\chi >> s$), see Figure 6.14(c). A regression analysis for $\tau(\chi)$ in this region reveals a power-law scaling with $E_f t/E_c s$ as

$$\frac{s\tau(\chi)}{T_u} = 0.85\left(\frac{s}{\chi}\right)^2 \left(\frac{E_f t}{E_c s}\right)^{2/3} \tag{6.10}$$

We define (arbitrarily) the shear decay length λ as the distance over which the shear traction decays to 1% of T_u/s, such that $\tau(\chi = \lambda) = 0.01T_u/s$. Accordingly, Equation 6.10 gives an estimate for λ as

$$\frac{\lambda}{s} = 9.22\left(\frac{E_f t}{E_c s}\right)^{1/3} \tag{6.11}$$

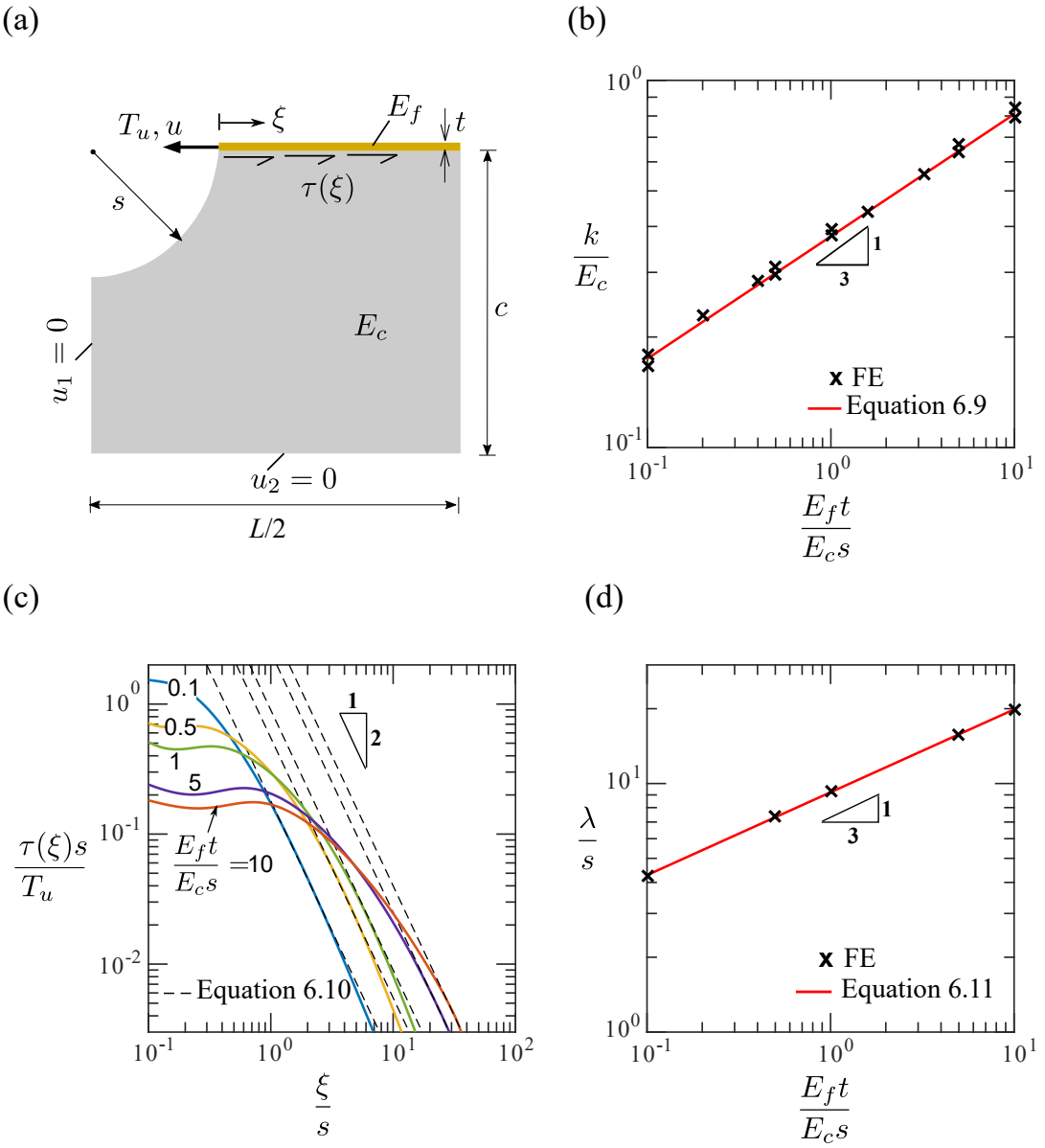

FIGURE 6.14: Force dipole problem: (a) geometry and loading employed in the FE simulation, (b) scaling for the spring stiffness k, (c) shear traction on the bottom layer of the face sheet $\tau(\chi)$; solid lines are FE predictions, and (d) scaling for the shear lag length λ.

The value of λ as obtained from FE simulations for different values of $E_f t/E_c s$ in the range of 0.1 and 10 is plotted in Figure 6.14(d) along with the predicted value 6.11; the agreement is excellent.

6.8.2 Comparison of analytical model with full indentation solution

A comparison of the indentation response from the above analytical model and from the full FE solution is given in Figure 6.15(a), for the case of a PC layer ($t = 1mm$) on a PVC foam substrate indented by a flat-bottom punch of width $2a = 1$ mm . The substrate is of thickness $c = 1$ m and of length $L = 1$ m. We find from Figure 6.15(a) that the P versus v responses are almost parallel, but there is an offset such that the analytical solution is stiffer. This is traced to the elastic compliance of the substrate in the FE model: it contributes an additional displacement Δv in the far-field region of magnitude

$$\Delta v = \frac{P}{2\pi E_c}\frac{3-4\nu_c}{1-\nu_c} ln\left(\frac{c}{\lambda_0}\right) \tag{6.12}$$

as given by the standard Flamant solution [30] for the vertical displacement at a depth c due to a point transverse load P acting on the surface of an elastic solid with plane strain modulus E_c and Poisson's ratio ν_c . The characteristic length λ_0 is taken to be $\lambda_0 = E_f t/E_c$. The predicted response from the model upon accounting for the additional displacement, Equation 6.12 due to a finite core depth is close to the full FE response, see Figure 6.15(a).

Additional comparisons are made in Figure 6.15(b) for the displacement profile of the top layer of the face sheet for $v = 10$ mm and in Figure 6.15(c) for the decay of shear traction along the bottom layer of the face sheet, also for $v = 10$ mm. The face sheet displaces approximately in the form of a circular arc within the core crush zone as predicted by the model, see Figure 6.15(b). The shear traction along the face sheet in the outer shear lag region also shows good agreement with the prediction 6.10, as shown in Figure 6.15(c). It is further seen from Figure 6.15(d) that the extent of the core crush zone s, as assumed in the force dipole problem for the computation of spring stiffness k, is approximately the plastic zone size in the full FE calculation. It appears that the force dipole problem, as depicted in Figure 6.14(a), is adequate to capture the response in the outer shear lag region.

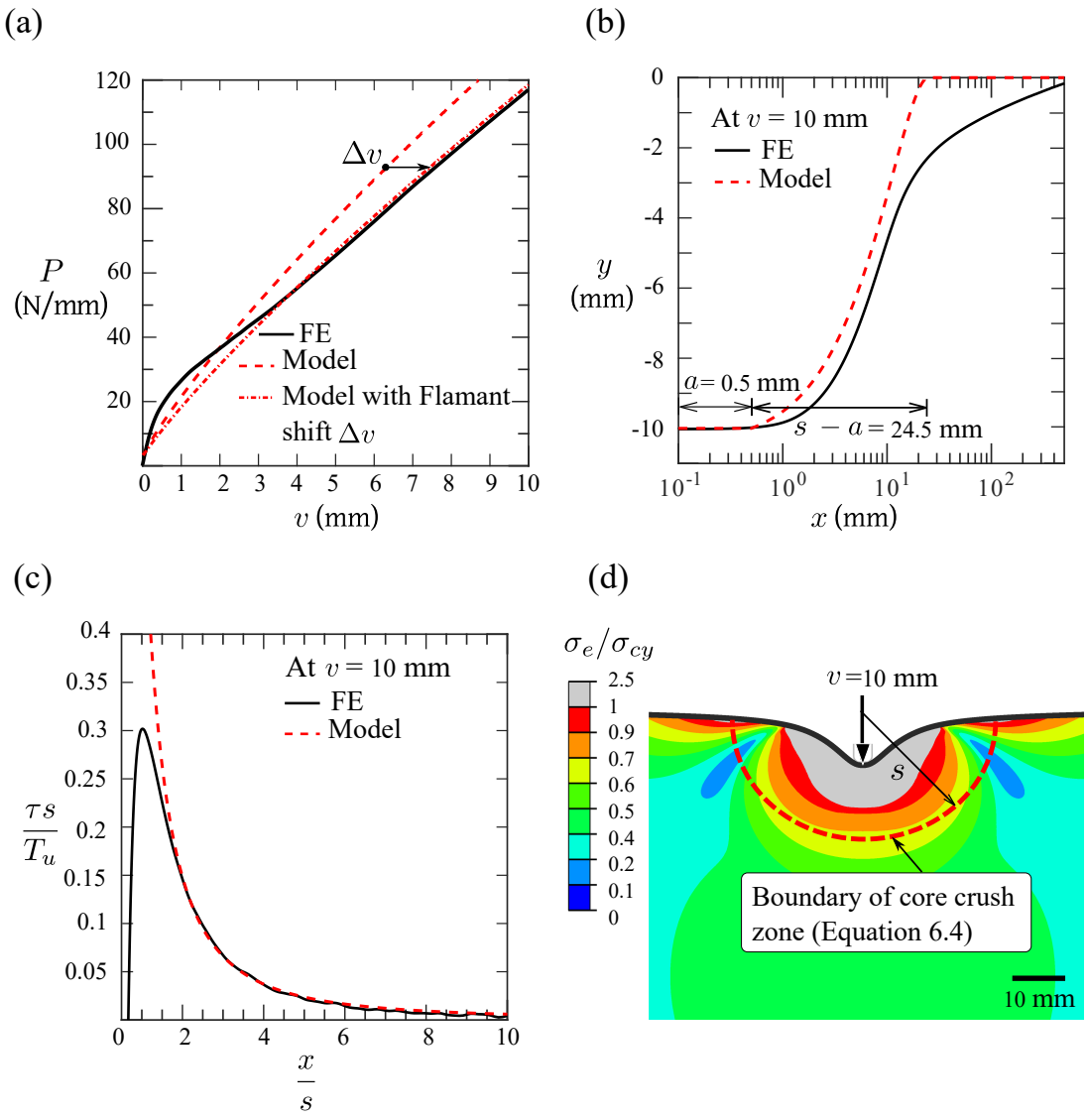

FIGURE 6.15: Comparison of the elastic membrane model with the full FE indentation response (with elastic face sheet): (a) Load versus displacement, (b) displacement profile of the top layer of the face sheet, (c) shear traction on the bottom layer of the face sheet, and (d) contours of the von Mises stress in the foam core; (b)-(d) correspond to $v = 10$ mm.

6.8.3 Plastic stretching of the face sheet

At a sufficiently high load, the tension T_u in the face sheet within the inner zone of core crush attains the yield value $T_u = \sigma_{fy} t$. Consequently, Equation 6.1 becomes

$$R = \frac{\sigma_{fy}}{\sigma_{cy}} t \tag{6.13}$$

and, upon substitution of this value for R into Equation 6.8 and 6.9 along with Equation 6.4 we obtain a characteristic Equation for the critical value of $\omega = \omega_y$ at the onset of plastic stretching of the face sheet as

$$\left(\frac{\sigma_{fy}}{\sigma_{cy}} sin\omega_y + \frac{a}{t}\right)^{1/3} \left(\frac{E_f}{E_c}\right)^{2/3} - \beta \frac{E_f}{\sigma_{cy}} \left[\omega_y \left(1 - \frac{\sigma_{fy}}{E_f}\right) - sin\omega_y\right] = 0 \qquad (6.14)$$

The value of the indentation load at the onset of plastic stretching in the face sheet P_y is obtained by substituting R from Equations 6.13 and ω_y from Equation 6.14 into Equation 6.2 as

$$P_y = 2(\sigma_{fy} t sin\omega_y + \sigma_{cy} a) \qquad (6.15)$$

If the face sheet behaves in an elastic, perfectly-plastic manner, then necking will occur soon after T_u attains the value $\sigma_{fy}t$, and the limit load P_y is given by Equation 6.15. In reality, PC has a sufficiently strong strain hardening characteristic beyond initial yield that it does not fail by necking but by cracking at an axial true strain on the order of 0.7. A more complex analytical model could be developed for the PC in the plastic range but this is beyond the scope of the present study and is of limited value.

The prediction of the above analytical model for the bi-layer geometry (and loading) of the basic study I of Table 6.1 is shown in Figure 6.7(a) to compare with the measured response and the full finite element prediction (including the plastic response of PC face sheet). It is clear from Figure 6.7(a) that the analytical model is in good agreement with measurement and FE prediction up to the yield load P_y as given by Equation 6.15. At higher loads, the analytical model is somewhat too stiff and this is due to the fact that it neglects tensile yield of the face sheet.

6.9 Indentation response of sandwich beam in 3-point bending

Is the indentation response of a bi-layer the same as that for a beam in 3-point bending, for the case where the beam collapses by an indentation mode? This is implicitly assumed to be the case in indentation analysis of sandwich beams. In order to address this question for the case of a PC/foam bi-layer, additional experiments were performed to compare the indentation response of a PC/foam sandwich beam in 3-point bending, with the indentation response of the bi-layer on a rigid support.

A typical 3-point bend geometry is shown in Figure 6.16(a). It comprises two identical PC face sheets of thickness t and a PVC foam core of thickness c. The sandwich beam is of depth b (into the page) and of span L, and it is supported on its span by two circular rollers, each of radius R. Consider indentation of the beam by a flat-bottom punch of width $2a$ (with a corner radius ρ). We choose a geometry such that the beam collapses by plastic indentation. Experiment and FE simulation were conducted on a beam of $L = 66$ mm, $c = 20$ mm, $t = 1$ mm and $b = 25$ mm. Support rollers of radius $R = 9.5$ mm, and a flat bottom punch of width $2a = 4$ mm (with $\rho = 0.5$ mm) were employed. The punch speed was $v = 0.025 mms^{-1}$.

The corresponding bi-layer geometry is given in Figure 6.4: it has the geometry of the basic study I of Table 6.1, such that $t = 1$ mm, $c = 100$ mm and $L = 400$ mm. The load versus displacement responses of both specimens are given in Figure 6.16(b). The initial elastic response of both geometries is similar, with elastic bending of the face sheets and elastic compression of the core directly beneath the punch. Now consider each geometry in turn.

1. For the bi-layer case, the core yields beneath the punch and the face sheet bends elastically as suggested by the Soden solution for small indent depth. Under increasing indent depth, membrane tension develops in the face sheet and this leads to a strong hardening response, as discussed above for the bi-layer problem.

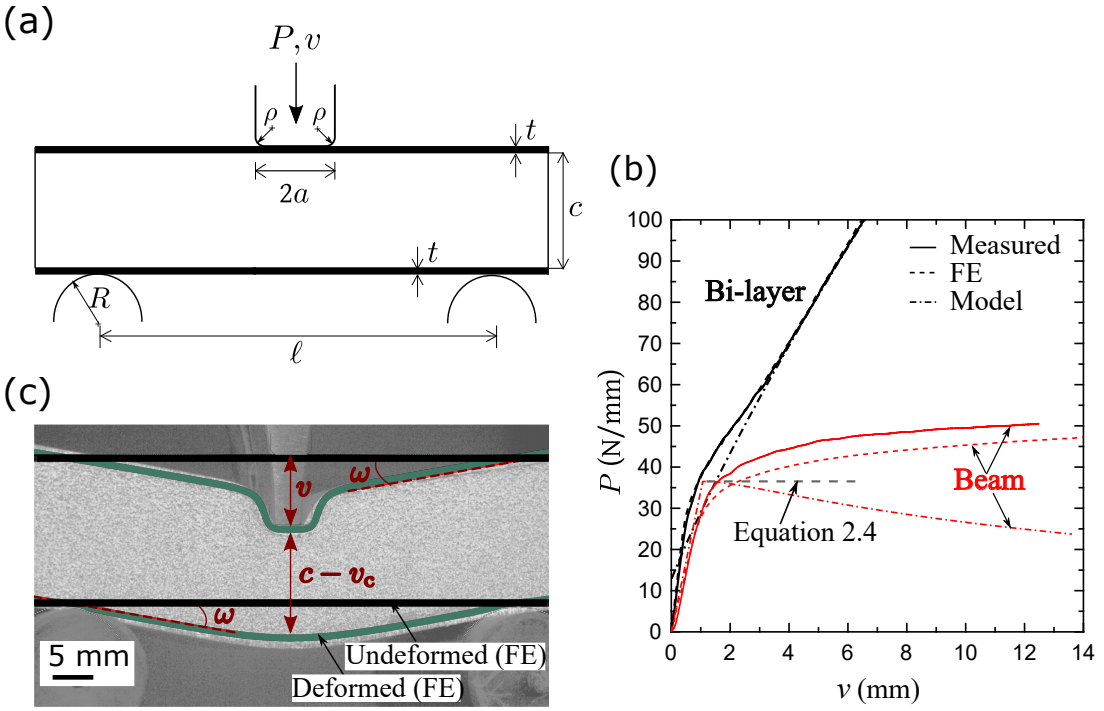

FIGURE 6.16: Indentation response of a sandwich beam under 3-point bending: (a) geometry and loading, (b) load versus displacement response of the PC/PVC beam, and (c) an overlay of the observed deformation profile of the beam in the experiment and the predicted deformation profile from FE, at $v = 10$ mm; only the face sheet deformation from the FE prediction is shown here.

2. For the sandwich beam, plastic collapse is by indentation of the top face sheet as suggested by Ashby et al. (2000), with the formation of plastic hinges adjacent to the punch as shown in Figure 6.17(a). Both experiment and FE analysis reveal that indentation continues in the manner as shown in Figure 6.16(c) for $v = 10$ mm; the measured and predicted deformation profile of the beam are in good agreement. We deduce from Figure 6.16(c) that the post-yield indentation of the beam involves rotation of the two face sheets (by an angle ω) and transverse compression of the core (by an amount v_c), with negligible hardening in the load versus indent depth curve. The FE solution also reveals that membrane tension does not develop in the upper face sheet, consistent with the observation that the load versus indent depth curve is almost flat. This is explained in the following analytical model.

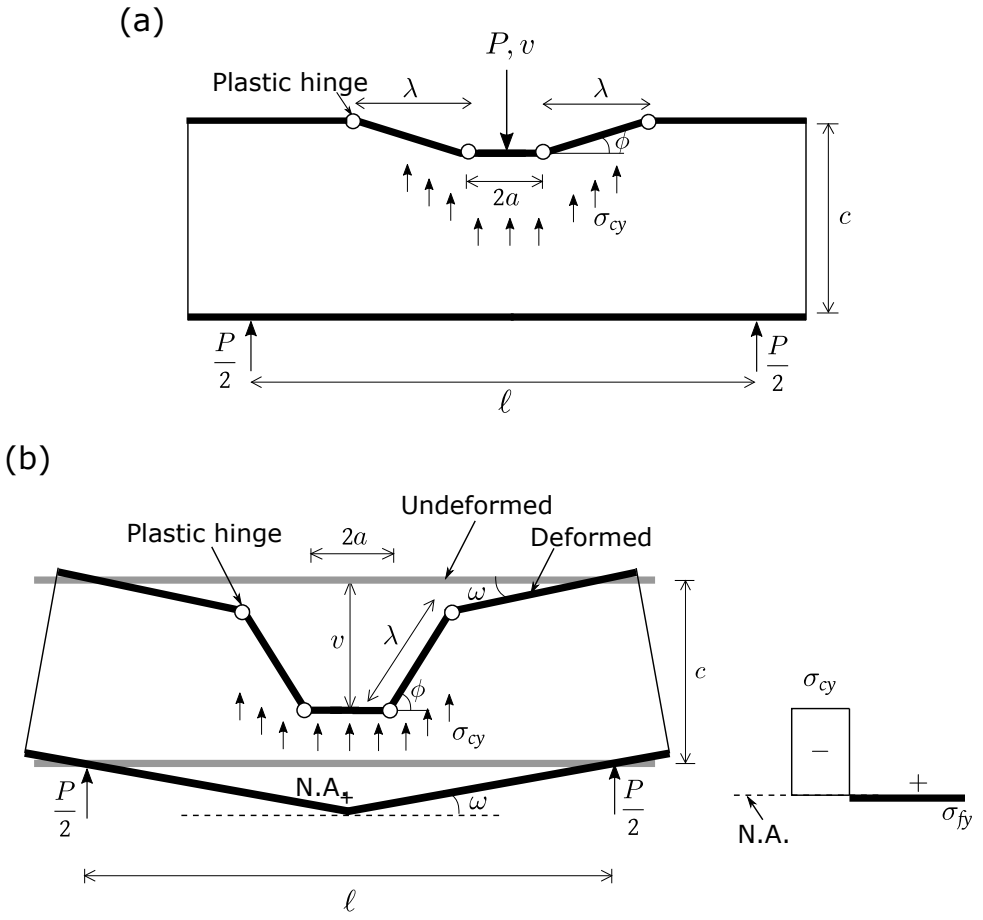

FIGURE 6.17: Indentation collapse of a sandwich beam under 3-point bending: (a) Collapse mode at small punch displacement (Ashby et al. (2000)), (b) assumed collapse mode for finite punch displacement, (c) assumed distribution of the longitudinal stress in the core and bottom face sheet at the mid-span section of the beam. N.A. refers to the Neutral Axis of bending.

6.9.1 Analytical model for 3-point bending response

Consider the sandwich beam of Figure 6.16(a) loaded by a flat-bottom punch (of corner radius $\rho << a$). Assume that the face sheets and core behave as elastic, perfectly-plastic solids of plane strain Young's moduli E_f and E_c, and of yield strengths σ_{fy} σ_{fy} and σ_{cy}, respectively. At small values of punch displacement $v << t$, both the face sheets and core behave in an elastic manner such that the load P increases linearly with v according to Ashby et al. (2000) as

$$v = \frac{PL^3}{48(EI)_{eq}} + \frac{PL}{4(AG)_{eq}} \tag{6.16}$$

where $(EI)_{eq}$ is the equivalent flexural rigidity and $(AG)_{eq}$ is the equivalent shear rigidity of the sandwich beam; these relate to the elastic moduli and cross-sectional dimensions of the beam as

$$(EI)_{eq} = \frac{E_f bt(c+t)^2}{2} + \frac{E_f bt^3}{6} + \frac{E_c bc^3}{12} \tag{6.17}$$

and

$$(AQ)_{eq} = \frac{G_c b(c+t)^2}{2} \tag{6.18}$$

Here, G_c is the shear modulus of the core.

Indentation collapse of the beam occurs when plastic hinges form in the top face sheet (adjacent to the punch) while the underlying core yields in compression, as sketched in Figure 6.17(a). At a small indent depth, the collapse load is that given by Equation 2.4, and the mode is that of Ashby et al. (2000). The outer hinges have a fixed separation λ, where

$$\lambda = t\sqrt{\frac{\sigma_{fy}}{\sigma_{cy}}} \tag{6.19}$$

as discussed by Ashby et al. (2000). The finite element solution suggests that this collapse mechanism evolves into the finite displacement version as defined in Figure 6.17(b), motivated by the observations of Figure 6.16(c). It has the following features. The two segments of the top face sheet, each of length λ, rotate but do not stretch. Directly beneath the punch, the core yields hydrostatically while the bottom face sheet yields in axial tension. The top face sheet carries negligible axial stress. An upper bound calculation is now performed to estimate the collapse response of the beam.

Consider first the top face sheet. Define ϕ as the angle of rotation of each of the 4 plastic hinges in the top face sheet such that

$$\phi = sin^{-1}\left(\frac{v_c}{\lambda}\right) \tag{6.20}$$

where v_c is the core compression at any given value of the punch displacement v, as defined in Figure 6.16(c).

Now consider the neutral axis of bending of the beam section comprising core and bottom face sheet, at the mid-span position. Place the neutral axis at a height z above the outermost fibre of the bottom face sheet. Then, axial force equilibrium on this section dictates that

$$t\sigma_{fy} + (z-t)\sigma_{cy} = [c-(z-t)]\sigma_{cy} \tag{6.21}$$

with solution

$$z = t + \frac{c}{2}\left(1 - \frac{t\sigma_{fy}}{\sigma_{cy}}\right) \tag{6.22}$$

For the sandwich beam under consideration, Equation 6.22 implies that $z \approx t$, and the longitudinal stress state on the cross-section of the beam at mid-span is sketched in Figure 6.17(c).

Kinematic consistency between the face sheets and core implies

$$v = v_c + \frac{L}{2}tan\omega \tag{6.23}$$

for an angle of rotation ω of the beam section about its neutral axis of bending at the midspan section, as sketched in Figure 6.17(b). Equating the horizontal contraction of the core and top face sheet gives

$$ctan\omega = \lambda(1 - cos\phi) \tag{6.24}$$

The indentation load of the sandwich beam is determined by a work calculation along the same lines as that of Ashby et al. (2000). The external plastic work done by load P during an incremental punch displacement δv is

$$\delta W = P\delta v \tag{6.25}$$

This is balanced by the internal plastic work which includes the contribution from two modes of deformation:

1. a *local* mode of deformation involving the rotation of 4 plastic hinges in the top face sheet, each by an angle $\delta\phi$, and transverse compression of the core between the outer hinges by an amount δv_c. The incremental local plastic work δW_L (per unit depth of the beam) is

$$\delta W_L = 4M_{Pf}\delta\phi + (2a + \lambda cos\phi)\sigma_{cy}\delta v_c \tag{6.26}$$

   where M_{Pf} is the plastic moment of the top face sheet section, $M_{Pf} = \frac{1}{4}\sigma_{fy}t^2$ and

2. a *global* mode of deformation wherein the beam section (of core and bottom face sheet) rotates about the neutral axis of bending by an angle $\delta\omega$. The incremental global plastic work δW_G (per unit depth of the beam) is

$$\delta W_G = 2M_P\delta\omega \tag{6.27}$$

   where M_P is the plastic moment of the beam section given by

$$M_P = \frac{1}{2}\sigma_{cy}c^2\left(1 - \frac{v_c}{c}\right)^2 \tag{6.28}$$

   upon ignoring the minor contribution from the top face sheet.

The statement of work balance, $\delta W = \delta W_L + \delta W_G$, reads

$$P\left(\delta v_c + \delta\omega\frac{L}{2}\right) = 4M_{Pf}\delta\phi + (2a+\lambda cos\phi)\sigma_{cy}\delta v_c + 2M_P\delta\omega \tag{6.29}$$

upon using the relations 6.25-6.27. Now define two non-dimensional terms $\bar{v}$ and $\bar{\lambda}$ as

$$\bar{v} = \frac{\frac{v_c}{\lambda}}{\sqrt{1-\frac{v_c^2}{\lambda^2}}} \tag{6.30}$$

and

$$\bar{\lambda} = \lambda\sqrt{1-\frac{v_c^2}{\lambda^2}} \tag{6.31}$$

The indentation load, Equation 6.29, for small ω can be rewritten in terms of $\bar{v}$ and $\bar{\lambda}$ using Equations 6.20, 6.23 and 6.24 along with Equations 6.30 and 6.31

$$P\left(1+\frac{L\bar{v}}{2c}\right) = \frac{4M_{Pf}}{\bar{\lambda}} + (2a+\bar{\lambda})\sigma_{cy} + \frac{2M_P\bar{v}}{c} \tag{6.32}$$

The full P versus v collapse response is obtained from 6.23 and 6.32 upon treating $\bar{v}$ as a free parameter, and this is plotted in Figure 6.16(b) together with the initial elastic response 6.16. We find from Figure 6.16(b) that the simple analytical model gives mild softening in contrast to the plateau in load as observed in the experiment and FE simulation. This is partly attributed to the lack of hardening in both the face sheet and the foam core in the analytical model.

We emphasize that there is a marked contrast between the collapse response of a simply supported beam and an end-clamped beam. For the end-clamped case, membrane tension can develop in the face sheet, as noted by Tagarielli et al. (2004). They compared the response of simply supported and end-clamped beams in 3-point bending, and showed that the end-clamping leads to a hardening curve of indent load versus displacement, and that the hardening is geometric in nature and not material related.

6.10 Concluding remarks

The present study highlights the fact that a PC face sheet significantly elevates the indentation strength of a PVC foam substrate. The foam compresses plastically while the face sheet remains elastic until the indent is much deeper than the face sheet thickness. The increase in indentation load is first due to elastic bending and then due to elastic stretching of the PC face sheet. This is supported by detailed finite element simulations and an analytical model that is based on the idea of load diffusion. Our study also highlights the distinction between the indentation response of a bi-layer on rigid foundation and a sandwich beam in 3-point bending. Although the initial yield load is comparable for the 2 geometries, the subsequent hardening responses differ significantly. Finite element analysis and an idealized analytical model reveal that the lack of hardening in the sandwich beam is due to the low bending strength of the core and bottom face sheet.

Chapter 7

The indentation response of lightweight multilayer foam plates

Summary

A parametric finite element study is performed on the indentation of a thin PC plate attached to a foundation consisting of a high density PVC foam foundation which is in turn attached to a relatively thicker foundation of lower density PVC foam. The purpose of such a hybrid material is to protect a structure underneath the foam foundation, whilst also providing similar indentation resistance at reduced weight. The following dimensionless parameters were varied in the finite element study; indenter diameter/facesheet thickness (D/t), and indenter diameter/high density foam foundation thickness (D/c_1). The plate was 70% lighter than the equivalent reference thin PC plate supported by high density PVC foam only. We observe that the indentation resistance of the hybrid material is similar to that of the reference case whilst doing an excellent job at protecting the underlying structure.

7.1 Introduction

This chapter focuses on the indentation behaviour of lightweight hybrid plates, comprising one or more polymer foam layers with a ductile polymer layer (PC) bonded as a facesheet. Foam sandwich plates are ubiquitous in both natural and man made structures. The purpose of a sandwich plate is generally to provide a lightweight, structurally efficient material that protects an underlying structure or object. For example, the brain is surrounded and protected by the skull bones which is itself a sandwich panel comprising solid bone facesheets and porous, graded bone in between.

It is of great interest in the aerospace industry to protect critical components from impact by sharp or blunt impact. This applies to wing components or in particular the casings of engines where the protection of the turbine fan blades is critical. An additional requirement is that these components remain lightweight in order to reduce fuel costs and the subsequent environmental impact. This study aims to use a system of polymers and polymer foams to enable such behaviour during impact. We aim to reduce the pressure experienced by the underlying component whilst maximising the load experienced by the composite with the overall goal of achieving superior energy absorbtion characteristics. The chapter will present a numerical parametric study which explores the potential for weight reduction and protection for a polycarbonate plate bonded to two varieties of PVC polymer foam. One of high density and one of a density one order of magnitude lower. Additional indentation experiments complemented by X-ray CT scans will be used to validate the numerical study and provide further insight into the deformation and failure mechanisms.

7.2 Designing a hybrid, layered foam system for energy absorption and protection

The desired characteristics of the hybrid foam system to be designed and studied within chapter are as follows:

i) Maximise the energy absorbed by the hybrid material.

ii) Minimise the level of pressure/stress experienced by an underlying surface.

iii) Maximise the load experienced by the the hybrid material.

iv) Minimise the mass of the entire hybrid system.

This chapter presents an initial study towards achieving these goals. To this end, using finite element methods, we generate a large range of energy absorption and pressure level data during quasi-static indentation for a single low mass system with multiple indenter sizes. We subsequently analyse the data and provide insight into the potential for such a hybrid material formulation. Some basic indentation experiments and X-Ray computed tomography analyses are performed to gather further insight and validate the finite element data.

7.3 Finite element parametric study on the quasi-static indentation of hybrid foam plates

7.4 Details of parametric study

Consider a plate of diameter $2r$ (as shown in Figure 7.1) comprising a foam layer of a given relative density $\bar{\rho}_1$ and thickness c_1, a second foam layer of relative density $\bar{\rho}_2$ and thickness c_2, and a solid polymer layer (PC in this case) with a density of ρ and thickness t. The plate undergoes quasi-static indentation, via a blunt, spherical indenter of diameter D. The following parametric study is used to explore the following normalised quantities, D/c_1, and t/c_1 in order to assess their effect on the extent of protection, which is quantified via the measurement of the pressure p_{max} (as shown in Figure 7.1) and the peak load P_{max}.

The materials chosen for this study are as follows. The facesheet is PC, with a Young's modulus, $E_f = 2200MPa$, a yield strength in tension of $\sigma_f = 52MPa$ and a density of

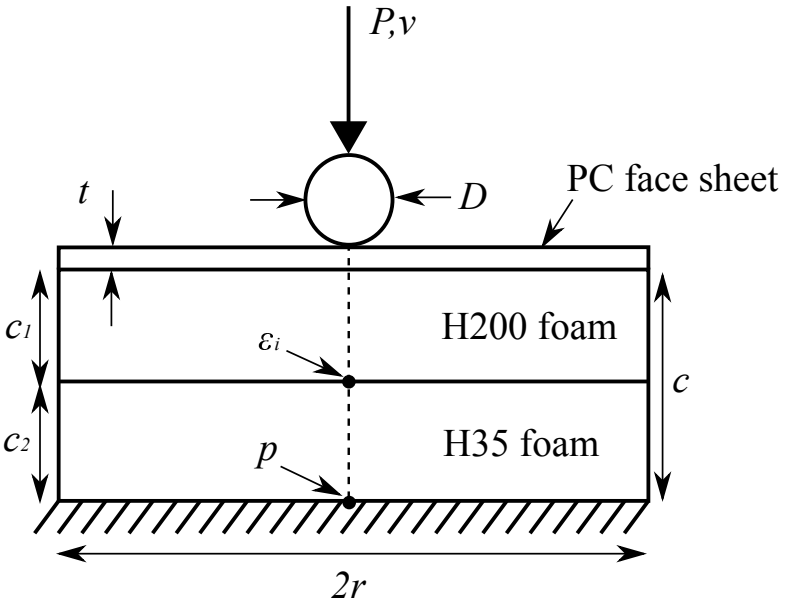

FIGURE 7.1: Hybrid plate geometry.

$\rho = 1500 kgm^{-3}$. We choose two foams, both closed cell PVC foam; (i) Divinycell H35 with $\bar{\rho} = 0.025$, $E_{c1} = 27.8MPa$, and $\sigma_{c1} = 0.43MPa$ and (ii) Divinycell H200 with $\bar{\rho} = 0.14$, $E_{c1} = 143MPa$, and $\sigma_{c1} = 5.1MPa$. Note that the foam properties are chosen to be in the rise direction (z-direction, as described in Chapter 2). We choose to fix $c_1/c_2 = 0.1$, this gives a significant reduction in mass of the entire structure (70% reduction based on a fixed 1mm PC face sheet) and serves as a good basis for achieving the goals (i)-(iii) as described in section 7.2. An outline of the indenter and specimen geometry used for the full set of simulations is detailed in Table 7.1. All simulations were carried out for three instances: (a) The multilayer, hybrid case with thickness c_1 consisting of H200 foam and the layer of thickness c_2 consisting of H35 foam. (b) a reference case where all of the foam material is H35, and (c) a second reference case where all of the foam material is H200. The PC face sheet was fixed at a thickness of $1mm$ for all simulations.

7.4.1 Finite element methods

Quasi-static finite element (FE) calculations were performed within ABAQUS/Explicit v6.14 to simulate the indentation response of the PC/foam sandwich plate. The FE mesh for both the PC face sheet and PVC foam substrate comprised of bilinear quadrilateral

TABLE 7.1: Indenter and specimen dimensions for finite element parametric study.

t/c_1=0, c_1/c_2=0			
D/c_1	c_1 (mm)	D (mm)	r (mm)
0.5	10	5	200
1	10	10	200
2	10	20	200
5	10	50	200
t/c_1=0.02, c_1/c_2=0.1			
D/c_1	c_1 (mm)	D (mm)	r (mm)
0.5	50	25	1000
1	50	50	1000
2	50	100	1000
5	50	250	1000
t/c_1=0.04, c_1/c_2=0.1			
D/c_1	c_1 (mm)	D (mm)	r (mm)
0.5	25	12.5	500
1	25	25	500
2	25	50	500
5	25	125	500
t/c_1=0.1, c_1/c_2=0.1			
D/c_1	c_1 (mm)	D (mm)	r (mm)
0.5	10	5	200
1	10	10	200
2	10	20	200
5	10	50	200
t/c_1=1, c_1/c_2=0.1			
D/c_1	c_1 (mm)	D (mm)	r (mm)
0.5	1	0.5	100
1	1	1	100
2	1	2	100
5	1	5	100

axisymmetric elements (type CAX4R). Perfect adhesion was assumed between the face sheet and foam, and the foam-foam interface. The spherical indenter was modelled as a rigid surfaces, and a frictionless contact was assumed between the rigid surface and the face sheet. A graded FE mesh was employed to provide fine refinement within the regions of contact. The face sheet had 20 elements along its thickness to suitably capture the bending stress field; a sensitivity study was performed to ensure that this mesh refinement was adequate to yield a converged indentation load versus displacement response.

The PC facesheet was modelled as an isotropic rate-independent von Mises solid with a true stress versus true strain response. This curve is derived from the measured response of PC face sheet in uniaxial tension (at a strain rate of $10^{-3}s^{-1}$) upon assuming a bi-linear fit for the post-yield nominal stress versus nominal strain data, based on the measured values in uniaxial tension. The PVC foam is specified with elastic properties as defined above. The post-yield behaviour of the foam was modelled using the crushable foam model in ABAQUS which allows for dissimilar response of the foam in tension and compression.

7.4.2 Experimental methods

Hybrid foam plates were manufactured and comprised two foams, H35 and H200, and a protective layer of polycarbonate (all with properties as described in section 7.3). Two cases were tested. Case 1 assessed the behaviour of a hybrid plate when $D/c_1 = 0.5$ and Case 2 when $D/c_1 = 2$. t/c_1 was constant in both cases at a value of $t/c_1 = 0.2$. Hybrid specimens were manufactured by bonding multiple layers of the various foams and polycarbonate layers with dimensions according to Table 7.2. A loctite 401 rapid curing cyanoacrylate adhesive was used to bond the various layers. Homogeneous plates of H200 and H35 foam only were made for comparison in both Case 1 and 2.

Prior to indentation testing the specimens were scanned in an X-ray computed tomography (CT) machine. This gave a three-dimensional image of the internal microstructure of the specimen prior to testing. The specimens were then placed on the loading platen

of a screw-driven Instron tensile test machine and were subsequently indented using spherical indenters with diameters of $D = 2.5$mm or $D = 10$mm for Case 1 and Case 2 respectively as described in Table 7.2. A post-failure X-ray CT scan was performed to give insight into the failure mechanism.

TABLE 7.2: Indenter and specimen dimensions for experimental indentation study.

	2r (mm)	c_1 (mm)	c_2 (mm)	D (mm)	D/c_1	t/c_1
Case 1	150	5	50	2.5	0.5	0.2
Case 2	200	5	50	10	2	0.2

7.5 Results and discussion

7.5.1 General FE parametric results

Shown in Figure 7.2 is a collection of typical load versus displacement responses for the indentation of a multilayer plate (where $t/c_1 = 0.1$). We observe that the load versus displacement response is generally linear in all cases which is typical of a stretching dominated response. Inspection of the stresses in the face sheet during indentation confirm that high degrees of stretching occurs in the radial direction.

An important result arises in which the multilayer case begins to approach the response of the reference H200 case when $D/c_1 < 1$. That is, we can achieve the same load carrying capacity with 90% less high density foam and that 90% of the underlying foam specimen has little influence on the load carrying capacity during indentation. Specimen failure is observed to occur via face sheet necking, local to the indenter. Shown in Figure 7.3 is the peak load for all simulations carried out over the full range of D/c_1 and t/c_1 values. Here we see that for $D/c_1 \leq 1$ the peak load of a hybrid structure equals that of a H200 homogeneous plate across the whole range of t/c_1 values. When $D/c_1 > 1$ we observe that the peak load of the hybrid foam material is always below that of H200 homogeneous plate but greater than the H35 plate. The peak load tends towards the response of the homogeneous H35 plate as t/c_1 increases for $D/c_1 > 1$. The physical explanation for such trends is based on the following two observations from FE

i) As D/c_1 increases the influence of the indenter becomes important; the size of the crush zone becomes much greater than the size of the foam layer (c_1) and the crush zone mostly occurs within the H35 foam. Explained in the converse situation, at small D/c_1 values the crush zone is small enough that it exists just within the H200 foam layer and thus carries all the traits of a homogeneous H200 plate.

ii) As t/c_1 increases the bending stiffness of the face sheet becomes dominant relative to the H200 foam layer. This implies a large crush zone and thus little influence of the H200 layer, and a dominant H35 layer, resulting in the lower peak loads.

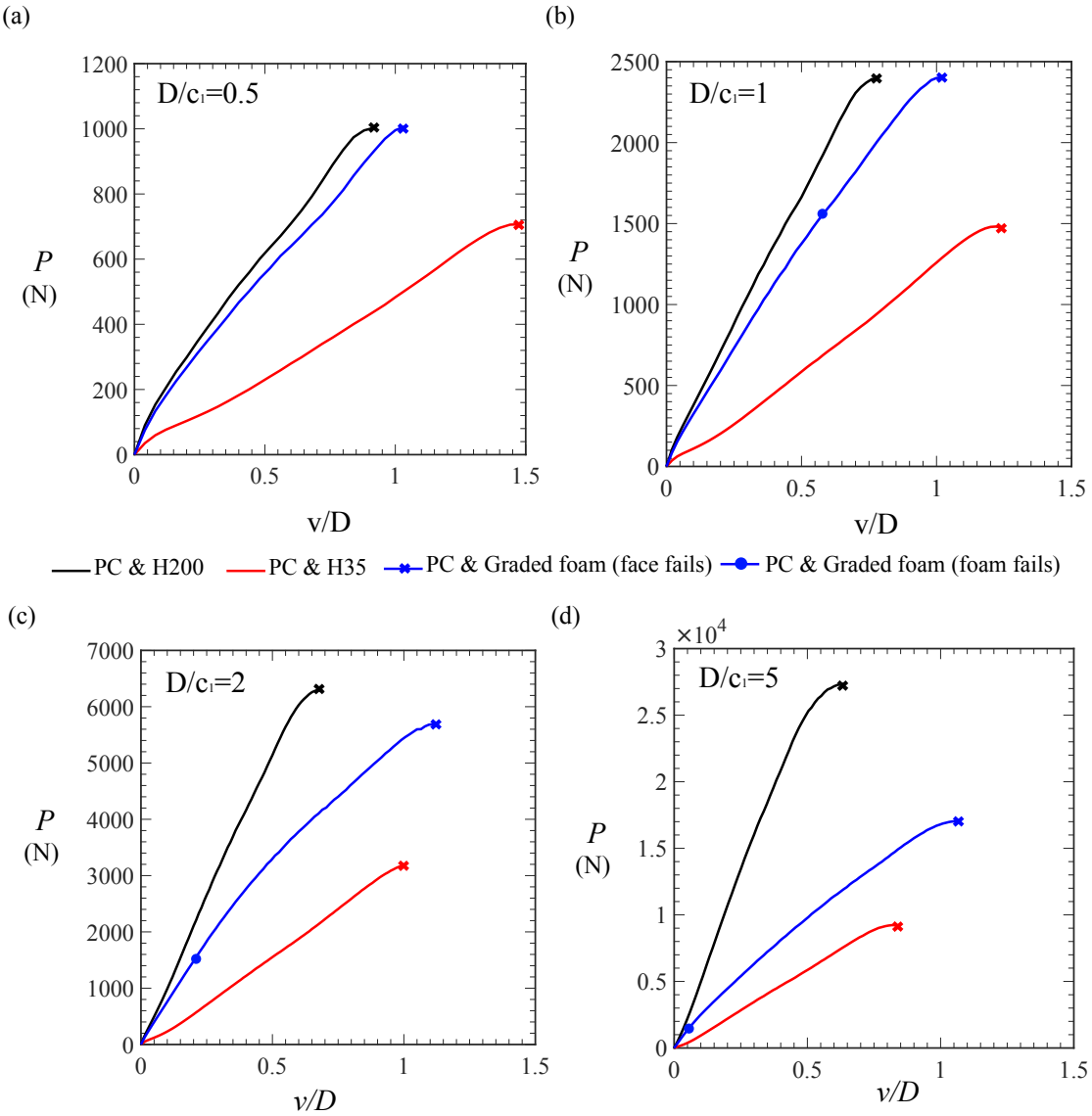

FIGURE 7.2: Load versus displacement response for $D/c_1 = [0.5, 1, 2, 5]$ at a constant value of $t/c_1 = 0.1$.

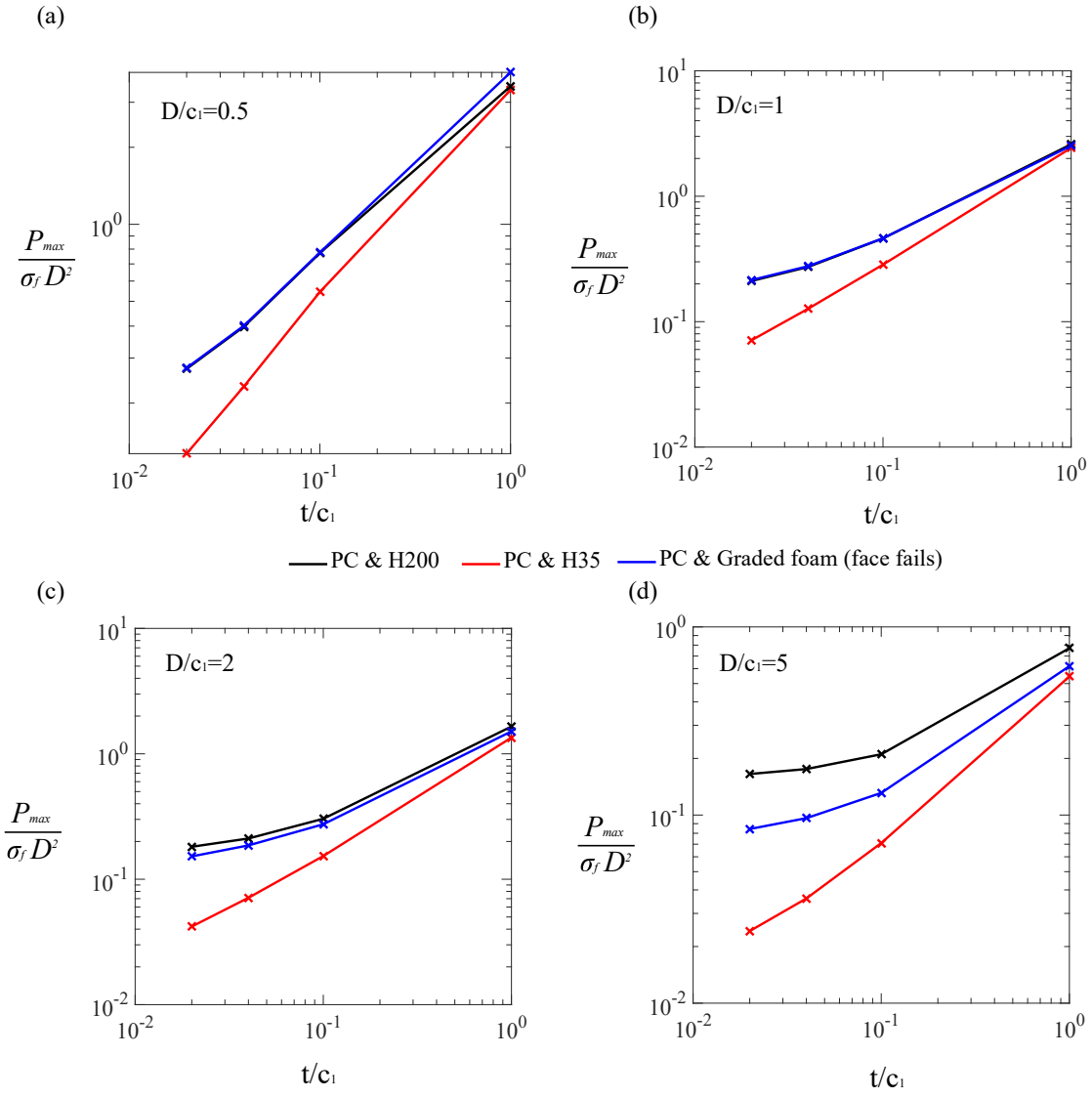

FIGURE 7.3: Normalised peak load as a function of t/c_1 for $D/c_1 = [0.5, 1, 2, 5]$.

The energy absorbed up until the peak load is plotted as a function of t/c_1 for a range of values of D/c_1 in Figure 7.4. We observe that the energy absorbed for the hybrid foam is similar or higher than the majority of the reference cases. This may be attributed to the bending action associated with indentation of the hybrid structure; the intermediate H200 layer bends unlike the reference homogeneous cases. The compliance due to the bending structure delays stretching and thus failure of the PC facesheet and thus the failure of the entire structure resulting in higher normalised energy absorption despite the lower normalised failure load in some cases.

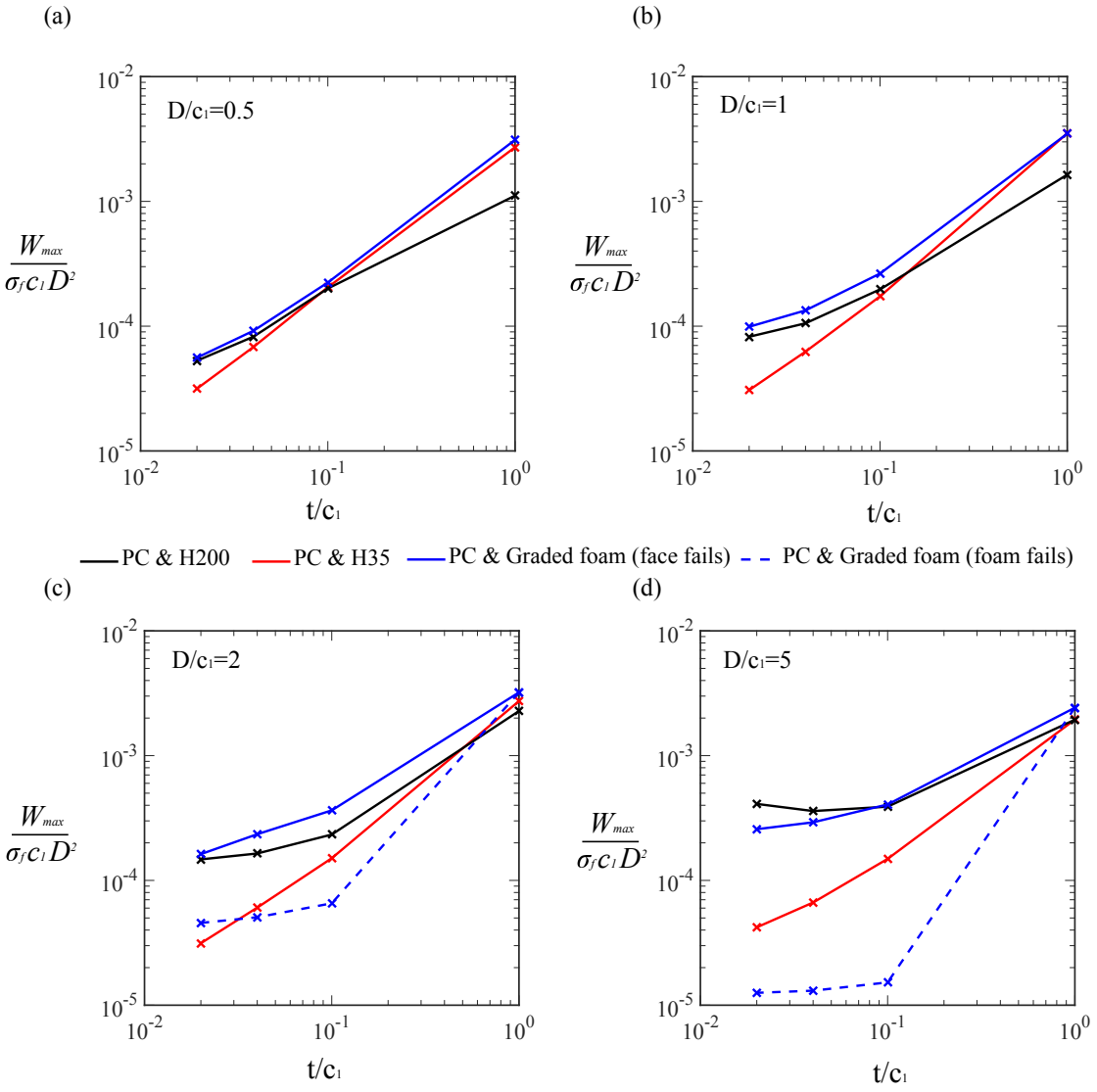

FIGURE 7.4: Normalised peak energy absorbed as a function of t/c_1 for $D/c_1 = [0.5, 1, 2, 5]$.

7.5.2 Predicted specimen failure

We anticipate that there is the possibility for foam failure within the specimen. The strain is monitored at the interface between the H200 foam and the H35 foam. The H200 foam bends due to the compliant foundation underneath. Hence we anticipate that it will fail in tension under bending and thus we use the tensile failure strain of H200 foam ($\varepsilon_{f,c1} = 0.16$) as a failure criterion. This failure is indicated in Figure 7.2, and we note that failure of the foam will occur at a constant value of indentation load although at increasingly lower normalised displacement values, v/D, with increasing D/c_1. Furthermore, if we plot the normalised displacement at failure v_f/D as a function

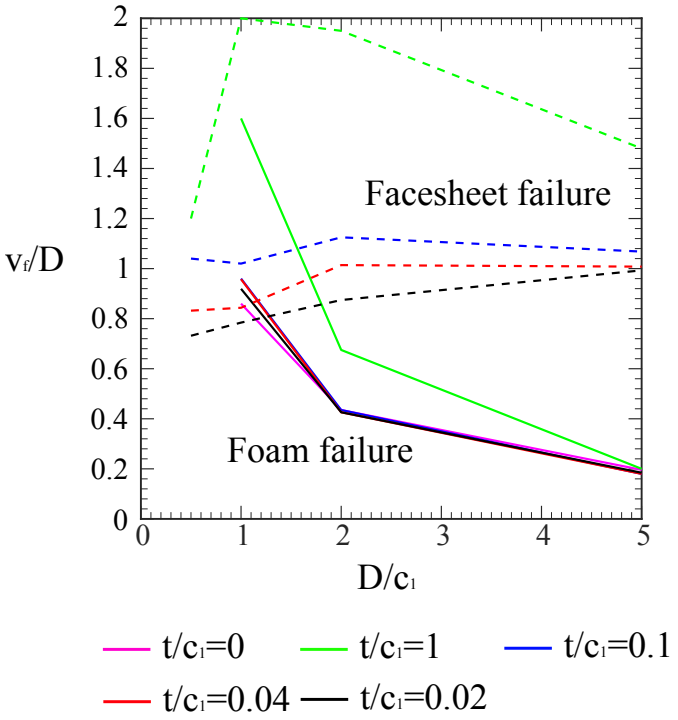

FIGURE 7.5: Normalised displacement to failure as a function of D/c_1 for $t/c_1 = [0, 0.02, 0.04, 0.1, 1]$, based on the foam, and the face sheet failure criterion.

of D/c_1 for all t/c_1 values we can observe a number of interesting results (see Figure 7.5. First, we see that the displacement to failure is not influenced by changes in t/c_1. In addition we observe that foam failure does not occur for $D/c_1 < 1$. In broad terms we can say that as D/c_1 increases, the displacement to foam failure decreases. These results have the potential for limiting the effectiveness of using a lightweight hybrid structure such as this. Initial experiments are carried out to explore this issue later in the chapter.

7.5.3 Protection of underlying structure

In Figure 7.6 we plot the pressure p_{max} (normalised by the maximum indenter pressure $\bar{P}$) on the underlying surface beneath the PC layer and foam, and directly in line with the indenter (as shown in Figure 7.1), as a function of t/c_1 for a range of values of D/c_1. We observe that, as D/c_1 increases, the level of protection improves, that is we observe a decrease in $p_{max}/\bar{P}$. This is explained as follows. The level of membrane stretching, and the size of the shear lag region is directly related to the size of the indenter as seen in

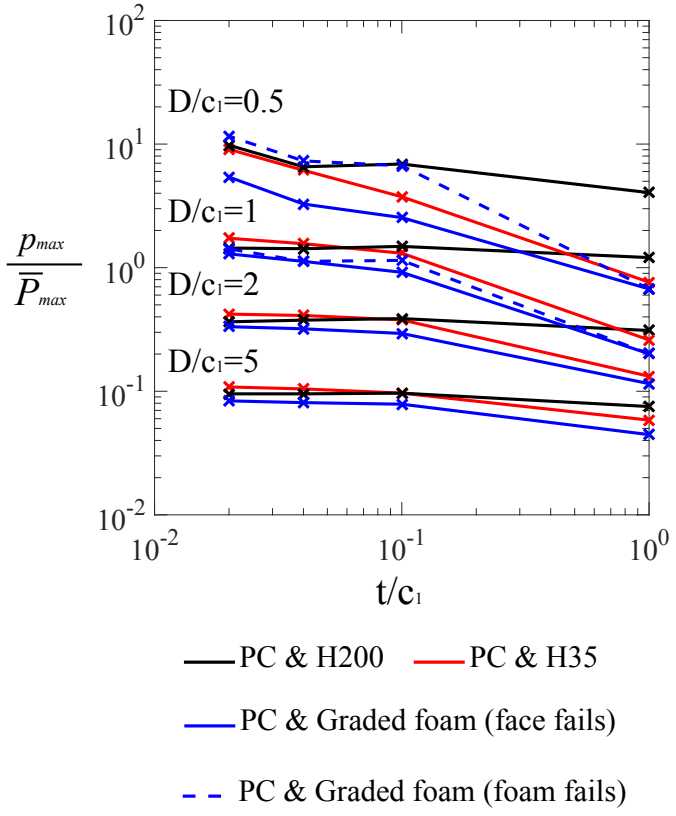

FIGURE 7.6: Normalised protection parameter as a function of t/c_1 for $D/c_1 = [0.5, 1, 2, 5]$.

the plane strain response in Chapter 6. We observe such behaviour in the present study and that this acts as a protection mechanism for the underlying surface. We also see improvement in the protection as t/c_1 increases. Again membrane stretching increases when a thicker facesheet is present and we arrive at the same conclusion.

When a hybrid foam structure is used, we observe a moderate improvement in protection. It is clear, as per the results of Giannakopoulos and Suresh (1997a,b) that a decreasing Young's modulus with depth results in the concentration of stresses at the upper surface adjacent to the indenter. However it appears that the relative influence of this particular arrangement of materials is stronger at lower values of $D/c_1 < 1$ as seen in Figure 7.6.

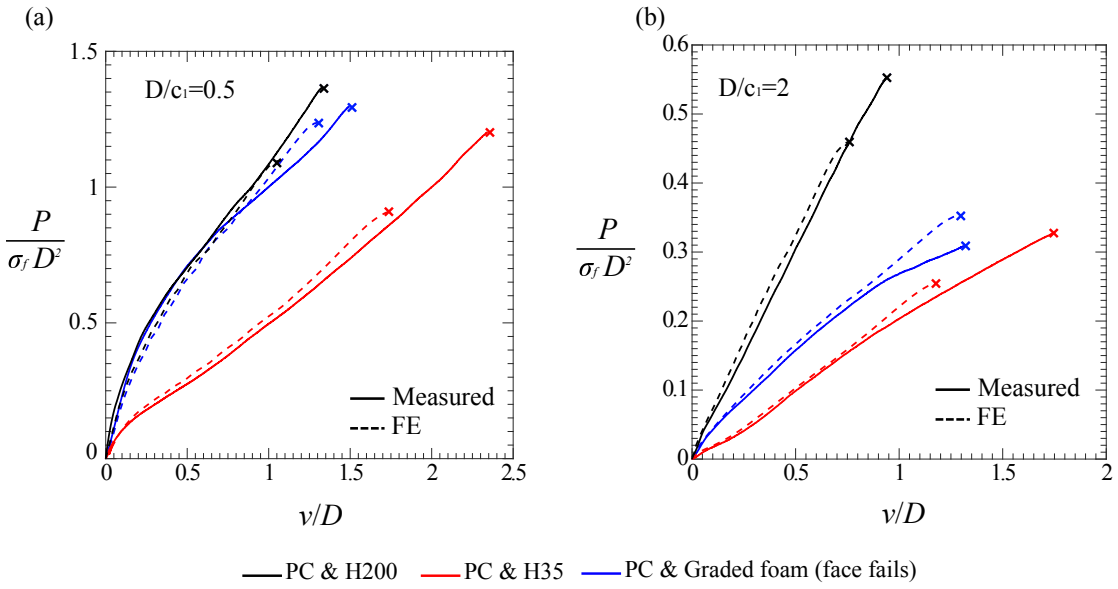

FIGURE 7.7: Measured load versus displacement response for (a) Case 1 and (b) Case 2

7.5.4 Experimental results

The normalised experimental load versus displacement response for both Case 1 and Case 2 are shown in Figure 7.7. In broad terms, we observe excellent agreement between FE and measured data, and of even more significance, we observe the same general behaviour as that found in the FE parametric study; a similar given indentation response for a 70% lighter structure.

The hybrid material in Case 1 approaches that of the heavier, homogeneous H200 response, whilst in Case 2 it is only marginally better than the homogeneous H35 response. These results are in line with the FE parametric study. One point of interest is that the premature failure due to cracking of the foam at the foam-foam interface does not occur as expected from the FE parametric study. This is confirmed in the post-experiment X-Ray CT scans shown in Figure 7.8 (a) and (d); specimen occurs by face sheet necking. This result does not render the data from section 7.5.2 obsolete, it merely necessitates the need for further experiments and general study of the indentation of hybrid foam plates.

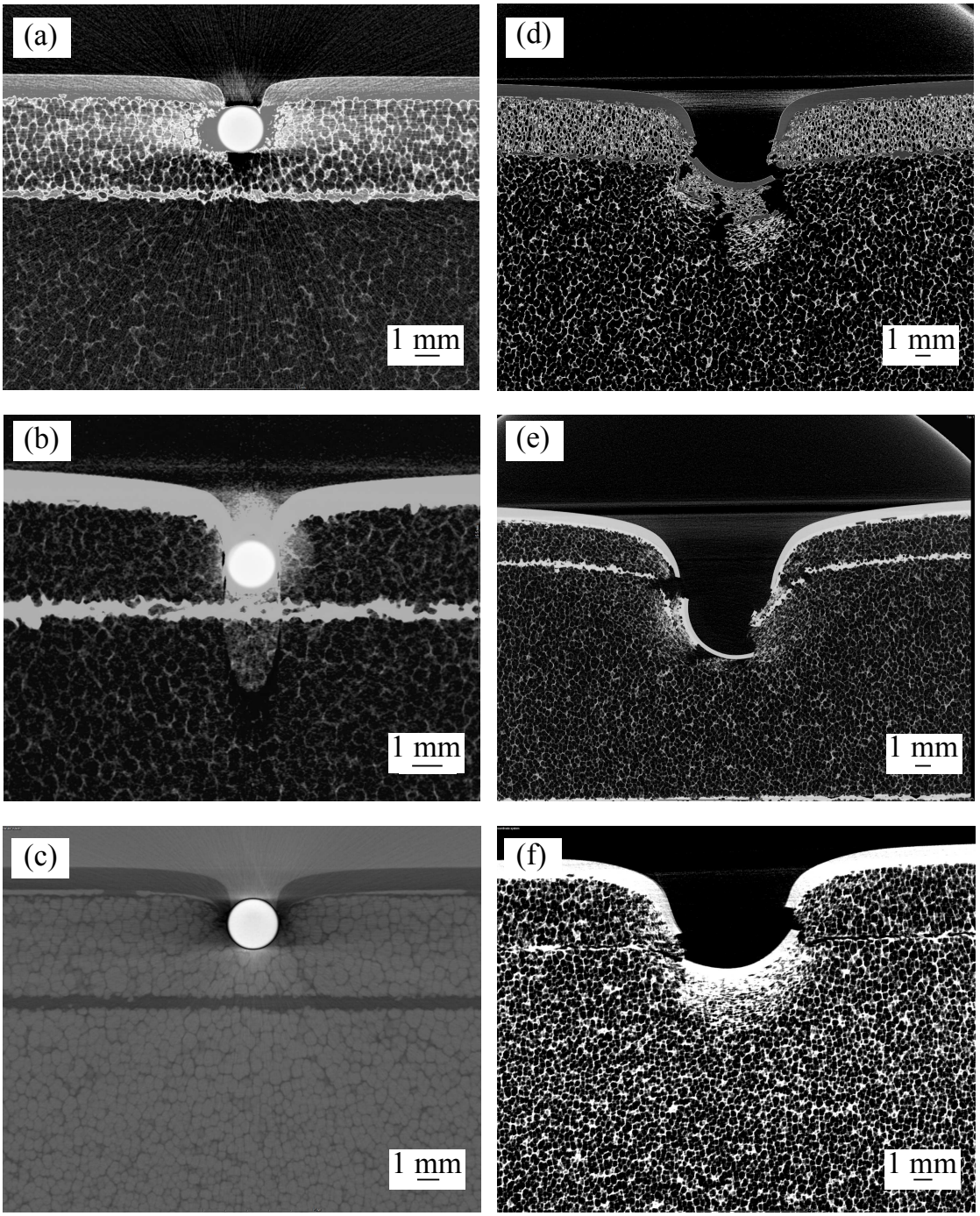

FIGURE 7.8: Post-failure X-ray CT images at failure for Case 1 (a)-(c) and Case 2 (d)-(f). (a) and (d) show the hybrid cases. (b) and (e) show the H35 reference specimen. (c) and (f) show the H200 reference specimens.

7.6 Concluding remarks

Giannakopoulos and Suresh (1997a,b) provided some basic insights into the behaviour of elastic indentation behaviour of graded materials. We found that they proved useful within this study as basic guidelines for the design of a hybrid layered foam structure. For example, we chose to have a system where the Young's modulus decreased with depth; this ensured that the stresses were localised to the exterior of the specimen i.e. adjacent to the top layer and not at the bottom surface. This results in protection of the bottom surface as required.

We performed a parametric finite element study complemented by experiments which studied the indentation of a thin PC plate attached to a foundation consisting of a high density PVC foam foundation which is in turn attached to a relatively thicker foundation of lower density PVC foam. The following dimensionless parameters were varied in the finite element study; indenter diameter/facesheet thickness (D/t), and indenter diameter/high density foam foundation thickness (D/c_1). We then observed that, despite its 70% reduction in mass, the hybrid structure could provide similar indentation resistance to that of a structure with a homogenous, high density foam foundation. This was observed to occur due to the localisation of deformation in the upper high density foam foundation whilst leaving the lower foam foundation relatively undeformed. If the indenter becomes large relative to the size of the high density foam layer then the hybrid structure becomes less effective at energy absorption and more useful in protecting the underlying surface (underneath the low density foam foundation). Thus a trade-off occurs between the indenter size and high density foam thickness.

This chapter has demonstrated a simple method for producing a lightweight, protective structure through the use of a gradient structure. The chapter provides promising results but is a preliminary study in essence and it is clear that a large amount of research remains to be carried out on such structures. For example, this study has been carried out at one ratio of the thickness of the high density foam layer to the thickness of the low density foam layer i.e. a 70% reduction in mass. The study must be carried out for a range of system masses.

Chapter 8

Conclusions and future work

The central theme of this thesis was the mechanics of layered foams, a generalised phrase that encompassed sandwich beams, foam protected by a reinforcing layer, and foams with gradient properties. The objectives of this thesis, as outlined in section 1.3, were thus described as follows: (i) to investigate the influence of residual stress on the collapse mechanisms of sandwich beams (ii) study the first yield behaviour of sandwich beams and the subsequent influence of residual stress (iii) understand and quantify the deep indentation behaviour of a foam protected by a reinforcing layer and (iv) understand the indentation behaviour of a graded foam plate. These objectives were addressed in Chapters 4, 5, 6, and 7 respectively. the present chapter outlines the primary conclusions from these chapters and gives potential areas of future work that may need to be addressed in this field.

8.1 Chapter 4-The influence of residual stress on the elastic indentation collapse mode of sandwich beams with elastic face sheets

a) An analytical description predicting the influence of an additional axial load in the face sheets was provided and indicated that significant changes in collapse load may

occur as a result. The analytical model expands upon the models of both Steeves and Fleck (2004b) and Tagarielli et al. (2004).

b) This model was then used to form a collapse load map for a sandwich beam system comprising GFRP (elastic) facesheets and PVC foam (rigid-perfectly-plastic) core in which the influence of residual stress was included. This new collapse mode map showed contours of the relative change in collapse load due to the presence of residual stress as well as the trajectory of the boundaries of this map under the influence of changing residual stress.

c) A series of numerical simulations were carried out, which successfully validated the analytical model in the case a of simply supported beam for both tensile and compressive residual stresses in the facesheet. We observed significant potential for increase in collapse load and thus energy absorbed by a sandwich beam specimen. Conversely, it is clear that compressive residual stresses in the face sheet promotes elastic indentation collapse and impacts negatively on the collapse load and energy absorption characteristics of a beam.

d) The FE simulations also demonstrated the significant role that facesheet thickness/indenter size ratio plays on the energy absorption characteristics under deep indentation at depths greater than the facesheet thickness. We found that the numerical simulations for a clamped case validated the model where compressive residual stresses were concerned. However, we observed that tensile residual stresses did not produce the expected increase in collapse but instead promoted membrane stretching, and alternatively produced significant increases in energy absorbed as a result.

8.1.1 Future work-Chapter 4

The study presented in this chapter has given insight into the behaviour of sandwich beams under the action of residual stress and has provided new potential design tools for the industrial end user of sandwich panels which allows greater energy absorption and collapse loads for the same weight. However, there are significant caveats that must be noted, and addressed in future studies. Firstly, the present study has shown

theoretical and numerical analysis only. Experiments are required in order to provide further insight into the behaviour described in preceding sections. Second, we have not provided any feasible, practical method for inducing residual stresses in a sandwich panel of such materials. This issue is discussed in more detail in the following chapter. The failure of the face sheet or foam has not been included in our analysis and this has the potential to limit the effectiveness of mechanisms described within this chapter.

8.2 Chapter 5-The influence of residual stress on the first yield and collapse behaviour of sandwich beams with elasto-plastic facesheets

a) An analytical description predicting the influence of a residual stress field on the elastic limit of a sandwich beam in bending. Three modes were identified: i) yield of the face sheets via global bending of the sandwich structure, ii) yield via indentation i.e. local bending of the face sheet and simultaneous yield of the core adjacent to the indenter/point load, and iii) yield via shearing of the entire cross section of the core. Residual stress was predicted to reduce the load at yield or the elastic limit of the sandwich panel.

b) Akin to collapse mode maps, first yield maps were formulated for a sandwich beam in three point bending giving the operative first yield mode for a set of dimensionless beam geometry and constituent material values. The boundaries of the maps depended on indenter shape (flat punch or cylindrical indenter) and level of residual stress present.

c) An experimental approach to applying a residual stress field to a sandwich beam was developed. An analytical prediction of the residual stress present after the experimental procedure was formulated. This also enabled an analysis of the limitations of the chosen experimental procedure.

d) A combination of experiments and finite element models were used to successfully validate the analytical models of a) whilst also highlighting the post-collapse behaviour of the beam and its final failure. In a number of cases, residual stress was shown to limit the displacement to failure of the sandwich beam.

8.2.1 Future work-Chapter 5

This chapter has provided significant insight into the prediction of the load and location at which the elastic limit is exceeded on a sandwich panel, providing a useful tool for the designer to predict failure or permanent deformation of a sandwich panel. Despite this, there is significant work yet to be carried out on this topic. First, a significant quantity of additional experimental and finite element geometries and materials are required to provide a comprehensive approach to validation of the models and maps provided here. Secondly, the experimental approach used here is sufficient for initial insights into the influence of residual stress on the flexural response of sandwich panels. However, there is significant scope for further optimisation of the experimental method, which, if done successfully would allow for other traditional stiffer face sheet materials to be studied such as GFRP and CFRP. This would also allow the elastic indentation response of Chapter 5 to be probed experimentally.

8.3 Chapter 6-Indentation of a layer on foam substrate

a) Plane strain indentation is by a flat-bottom punch or by a cylindrical roller, and the strain distribution within the PC face sheet and in the foam substrate are measured by digital image correlation. With increasing indent depth, the face sheet bends and stretches elastically and then plastically until face sheet or substrate fail. The generation of membrane tension in the face sheet plays a major role in supporting the indentation load when the indent depth exceeds the thickness of the face sheet and leads to a strong hardening behaviour beyond the initial collapse load for indentation. Finite element predictions of the full indentation response are based upon the measured tensile and compressive responses of the PVC foam and PC layer.

b) An analytical model is developed by matching the stretching response of the PC face sheet to the indentation response of the underlying foam, with due consideration for load diffusion from membrane tension of the PC face sheet into the underlying foam substrate. The indentation model is calibrated by ancillary finite element simulations of the load diffusion problem, and they emphasise the role of a shear lag zone in dictating the large indentation resistance. The indentation response of the bi-layer is also compared with that of a sandwich beam in 3-point bending.

c) Experiments, finite element simulations and an additional analytical model for indentation of the sandwich beam in 3-point bending reveal that strong hardening of the post-yield load versus displacement response is now absent, in contrast to that of the bi-layer. The lack of hardening in 3-point bending is traced to the relatively low value of the plastic bending moment of the beam section.

8.3.1 Future work-Chapter 6

This chapter provided a comprehensive study on the deep indentation of a layer on foam substrate. The model proposed here considers the indentation an elastic membrane stretching whilst attached to a plastic foundation. Brief insight is given into plastic membrane stretching, however we do not predict the final failure of the membrane. Further work should be carried out to this end, which would also lead to the creation of design maps for the industrial designer. Such a map would give energy absorption and peak load as a function of indenter size, foam strength, face sheet strength, and face sheet ductility.

8.4 Chapter 7-The indentation response of lightweight multilayer foam plates

a) A parametric finite element study complemented by experiments which studied the indentation of a thin PC plate attached to a foundation consisting of a high density PVC foam foundation which is in turn attached to a relatively thicker foundation

of lower density PVC foam. The following dimensionless parameters were varied in the finite element study; indenter diameter/facesheet thickness (D/t), and indenter diameter/high density foam foundation thickness (D/c_1). It was observed that, despite its 70% reduction in mass, the hybrid structure could provide similar indentation resistance to that of a structure with a homogenous, high density foam foundation. This was observed to occur due to the localisation of deformation in the upper high density foam foundation whilst leaving the lower foam foundation relatively undeformed.

b) It was found that, if the indenter becomes large relative to the size of the high density foam layer then the hybrid structure becomes less effective at energy absorption and more useful in protecting the underlying surface (underneath the low density foam foundation). Thus a trade-off occurs between the indenter size and high density foam thickness.

c) We found that the guidelines of Giannakopoulos and Suresh (1997a,b) proved useful within this study as basic guidelines for the design of a hybrid layered foam structure. For example, we chose to have a system where the Young's modulus decreased with depth; this ensured that the stresses were localised to the exterior of the specimen i.e. adjacent to the top layer and not at the bottom surface. This results in protection of the bottom surface as required.

8.4.1 Future work-Chapter 7

This chapter has demonstrated a simple method for producing a lightweight, protective structure through the use of a gradient structure. The chapter provides promising results but is a preliminary study in essence and it is clear that a large amount of research remains to be carried out on such structures. For example, this study has been carried out at one ratio of the thickness of the high density foam layer to the thickness of the low density foam layer i.e. a 70% reduction in mass. The study must be carried out for a range of system masses.

8.5 Published work

Chapter 6 has resulted in two publications in international scientific journals. The references are given below. Publications based on Chapters 4, 5 and 7 are in preparation.

Boyce, AM, Deshpande, VS, and Fleck, NA (2017) On the Indentation Resistance of a PC Layer on PVC Foam Substrate. Advanced Engineering Materials, vol. 19, no. 10, p. 1700075, 2017.

Boyce, AM and Tankasala, HC and Fleck, NA (2019) Indentation of a layer on foam substrate. International Journal of Mechanical Sciences, 150. pp. 379-392. ISSN 0020-7403

Appendix A: A material model for PVC foam

The post-yield behaviour of the PVC foam substrate is modelled using the ABAQUS crushable foam model with volumetric hardening. This phenomenological model allows for a dissimilar response of the foam in tension and compression, as commonly observed in polymer foams such as PVC, see Figure 3.5. The yield surface is assumed to be elliptical, and of the form

$$\phi = \sigma_e^2 + \alpha_{DF}^2(\sigma_m^2 - A^2) - B^2 \leq 0 \tag{8.1}$$

where σ_e is the von Mises effective stress, σ_m is the mean stress, and α_{DF} is the shape factor of the yield ellipse. The parameters A and B scale with the hydrostatic compressive strength of the foam p_c and with the hydrostatic tensile strength p_t according to

$$A = \frac{p_c - p_t}{2} \quad \text{and} \quad B = \alpha_{DF}\frac{p_c - p_t}{2} \tag{8.2}$$

In order to account for the observed value of zero plastic Poisson's ratio for the PVC foam, a non-associated plastic flow rule is adopted, with an assumed flow potential μ of the form

$$\mu = \sigma_e^2 + \frac{9}{2}\sigma_m^2 \tag{8.3}$$

During plastic flow, the hydrostatic compressive strength p_c increases with the increasing magnitude of the volumetric compressive plastic strain, while the hydrostatic tensile strength p_t remains constant. The hardening response of the foam is specified in the FE model by providing the uniaxial Cauchy stress versus true plastic strain data from a uniaxial compression test.

The shape factor α_{DF} of the yield surface is specified via the two strength ratios: (i) the ratio of the initial yield strength in uniaxial compression to hydrostatic compression, k_1 , and (ii) the ratio of the yield strength in hydrostatic tension to the initial yield strength in hydrostatic compression, k_2. These are related to α_{DF} according to

$$\alpha_{DF} = \frac{3k_1}{\sqrt{(3k_2 + k_1)(3 - k_1)}} \tag{8.4}$$

The values of k_1 and k_2 are such that $0 < k_1 < 3$ and $k_2 > 0$. For the PVC H200 foam employed in this study, $k_1 \approx 2$ based on the experimental study of Deshpande and Fleck, and $k_2 = 2.2$ in order for the predicted uniaxial tensile strength for the foam to match the measured uniaxial tensile strength (to within 3%). Consequently, we obtain $\alpha_{DF} \approx 2$ for the H200 foam.

Bibliography

Allen, H. G. (1969). *Analysis and design of structural sandwich panels*. Pergamon Press, Oxford.

Andrews, E. W., Gioux, G., Onck, P., and Gibson, L. J. (2001). Size effects in ductile cellular solids. Part II: Experimental results. *International Journal of Mechanical Sciences*, 43(3):701–713.

Andrews, E. W., Sanders, W., and Gibson, L. J. (1999). Compressive and tensile behaviour of aluminum foams. *Materials Science and Engineering A*, 270(2):113–124.

Apetre, N. A., Sankar, B. V., and Ambur, D. R. (2008). Analytical modeling of sandwich beams with functionally graded core. *Journal of Sandwich Structures and Materials*, 10(1):53–74.

Ashby, M. F., Evans, A. G., Fleck, N. A., Gibson, L. J., Hutchinson, J. W., and Wadley, H. N. G. (2000). *Metal foams: a design guide*. Butterworth, Heinemann, London.

Bart-Smith, H., Hutchinson, J. W., and Evans, A. G. (2001). Measurement and analysis of the structural performance of cellular metal sandwich construction. *International Journal of Mechanical Sciences*, 43(8):1945–1963.

Biot, M. A. (1937). On bending of an infinite beam on an elastic Foundation. *Journal of Applied Mathematics and Mechanics*, 22(5):984–988.

Bostrom, P. O. (1975). Collapse modes of a rigid-plastic beam on a rigid-plastic foundation. *International Journal of Mechanical Sciences*, 17:73–84.

Boyce, A. M., Deshpande, V. S., and Fleck, N. A. (2017). On the Indentation Resistance of a PC Layer on PVC Foam Substrate. *Advanced Engineering Materials*, 19:1700075.

Chen, C., Harte, A. M., and Fleck, N. A. (2001). Plastic collapse of sandwich beams with a metallic foam core. *International Journal of Mechanical Sciences*, 43(6):1483–1506.

Cui, L., Kiernan, S., and Gilchrist, M. D. (2009). Designing the energy absorption capacity of functionally graded foam materials. *Materials Science and Engineering A*, 507(1-2):215–225.

Daynes, S., Diaconu, C. G., Potter, K. D., and Weaver, P. M. (2010). Bistable Prestressed Symmetric Laminates. *Journal of Composite Materials*, 44(9):1119–1137.

Daynes, S., Potter, K. D., and Weaver, P. M. (2008). Bistable prestressed buckled laminates. *Composites Science and Technology*, 68(15-16):3431–3437.

Deshpande, V. S. and Fleck, N. A. (2000). Isotropic constitutive models for metallic foams. *Journal of the Mechanics and Physics of Solids*, 48(6):1253–1283.

Deshpande, V. S. and Fleck, N. A. (2001). Multi-axial yield behaviour of polymer foams. *Acta Materialia*, 49(10):1859–1866.

DIAB (2005). Divinycell H- grade technical manual.

Fancey, K. S. (2011). Prestressed polymeric composites produced by viscoelastically strained nylon 6,6 fibre reinforcement. *Journal of Reinforced Plastics and Composites*, 19(15/2000):1251–1266.

Fazal, A. and Fancey, K. S. (2014). UHMWPE fibre-based composites: Prestress-induced enhancement of impact properties. *Composites Part B: Engineering*, 66:1–6.

Flores-Johnson, E. A. and Li, Q. M. (2010). Indentation into polymeric foams. *International Journal of Solids and Structures*, 47(16):1987–1995.

Gaitanaros, S. and Kyriakides, S. (2015). On the effect of relative density on the crushing and energy absorption of open-cell foams under impact. *International Journal of Impact Engineering*, 82:3–13.

Giannakopoulos, A. E. (2002). Indentation of plastically graded substrates by sharp indentors. *International Journal of Solids and Structures*, 39:2495–2515.

Giannakopoulos, A. E. and Pallot, P. (2000). Two-dimensional contact analysis of elastic graded materials. *Journal of the Mechanics and Physics of Solids*, 48(8):1597–1631.

Giannakopoulos, A. E. and Suresh, S. (1997a). Indentation of solids with gradients in elastic properties: Part I. Point force. *International Journal of Solids and Structures*, 34(19):2357–2392.

Giannakopoulos, A. E. and Suresh, S. (1997b). Indentation of solids with gradients in elastic properties: Part II. Axisymmetric indentors. *International Journal of Solids and Structures*, 34(19):2393–2428.

Gibson, L. J. and Ashby, M. F. (1999). *Cellular Solids: Structure and Properties*. Cambridge University Press, Oxford.

Gibson, L. J., Ashby, M. F., and Harley, B. A. (2010). *Cellular Materials in Nature and Medicine*. Cambridge University Press, Oxford.

Hetenyi, M. (1961). *Beams on elastic foundation : theory with applications in the fields of civil and mechanical engineering*. Ann Arbor, MI: Univeristy of Michigan Press.

Jang, W. Y. and Kyriakides, S. (2009). On the crushing of aluminum open-cell foams : Part I . Experiments. *International Journal of Solids and Structures*, 46(3-4):617–634.

Ke, L. L. and Wang, Y. S. (2006). Two-dimensional contact mechanics of functionally graded materials with arbitrary spatial variations of material properties. *International Journal of Solids and Structures*, 43:5779–5798.

Koiter, W. T. (1966). On the diffusion of load from a stiffener into a sheet. *Quarterly Journal of Mechanics and Applied Mathematics*, 3(2):164–178.

Li, Y., Ramesh, K. T., and Chin, E. S. C. (2001). Dynamic characterization of layered and graded structures under impulsive loading. *International Journal of Solids and Structures*, 38(34-35):6045–6061.

Liu, Z., Meyers, M. A., Zhang, Z., and Ritchie, R. O. (2017). Functional gradients and heterogeneities in biological materials: Design principles, functions, and bioinspired applications. *Progress in Materials Science*, 88:467–498.

Martin, P. A., Richardson, J. D., Gray, L. J., and Berger, J. R. (2002). On Green's function for a three-dimensional exponentially graded elastic solid. *Proceedings: Mathematical, Physical and Engineering Sciences*, 458(2024):1931–1947.

McCormack, T. M., Miller, R., Kesler, O., and Gibson, L. J. (2001). Failure of sandwich beams with metallic foam cores. *International Journal of Solids and Structures*, 38:4901–4920.

Mines, R. A. W. and Li, Q. M. (2000). Static Behaviour of Transversely Loaded CFRP Laminate Panels Subject to In-Plane Tension. *Strain*, 36(2):71–80.

Mohan, K., Yip, T. H., Sridhar, I., and Seow, H. P. (2007). Effect of face sheet material on the indentation response of metallic foams. *Journal of Materials Science*, 42(11):3714–3723.

Motahhari, S. and Cameron, J. (1998). Impact strength of fiber pre-stressed composites. *Journal of Reinforced Plastics and Composites*, 17(2):123–130.

Mu, L., Cho, C., Zhao, G., and Xiao, D. (2015). A new indentation model for sandwich circular panels with gradient metallic foam cores. *Composites Part B: Engineering*, 83:270–275.

Muki, R. and Sternberg, E. (1967). Transfer of Load From an Edge-Stiffener to a Sheet — A Reconsideration of Melan's Problem. *Journal of Applied Mechanics*, 34(3):679–686.

Nishi, Y., Okada, T., Okada, S., Hirano, M., Matsuda, M., Matsuo, A., and Faudree, M. C. (2014). Effects of Tensile Prestress Level on Impact Value of 50 vol % Continuous Unidirectional 0 Degree Oriented Carbon Fiber Reinforced Epoxy Polymer (CFRP). *Materials Transactions*, 55(2):318–322.

Olurin, O. B., Fleck, N. A., and Ashby, M. F. (2000). Indentation resistance of an aluminium foam. *Scripta Materialia*, 43(11):983–989.

Onck, P., Andrews, E. W., and Gibson, L. J. (2001). Size effects in ductile cellular solids. Part I: modeling results. *International Journal of Mechanical Sciences*, 43(3):681–699.

Petras, A. and Sutcliffe, M. P. F. (1999). Failure mode maps for honeycomb sandwich panels. *Composite Structures*, 44(4):237–252.

Pitarresi, G. and Amorim, J. (2011). Indentation of rigidly supported sandwich beams with foam cores exhibiting non-linear compressive behaviour. *Journal of Sandwich Structures and Materials*, 13(5):605–636.

Plantema, F. J. (1966). *Sandwich Construction: The Bending and Buckling of Sandwich Beams, Plates and Shells*. John Wiley & Sons Ltd.

Poapongsakorn, P. and Kanchanomai, C. (2011). Time-dependent deformation of closed-cell PVC foam. *Journal of Cellular Plastics*, 47(4):323–336.

Qin, Q. H. and Wang, T. J. (2012). Plastic Analysis of Metal Foam Core Sandwich Beam Transversely Loaded by a Flat Punch: Combined Local Denting and Overall Deformation. *Journal of Applied Mechanics*, 79(4):041010.

Qin, Q. H., Zhang, J. X., Wang, Z. J., Li, H. M., and Guo, D. (2014). Indentation of sandwich beams with metal foam core. *Transactions of Nonferrous Metals Society of China*, 24(8):2440–2446.

Richards, J. and Richards, M. (1990). Prestressed plastic foam structural member, Patent No. US4903446A.

Rubino, V., Deshpande, V. S., and Fleck, N. A. (2010). The three-point bending of Y-frame and corrugated core sandwich beams. *International Journal of Mechanical Sciences*, 52(3):485–494.

Shuaeib, F. M. and Soden, P. D. (1997). Indentation Failure of Composite Sandwich Beams. *Composites Science and Technology*, 57(9-10):1249–1259.

Soden, P. D. (1996). Indentation of composite sandwich beams. 31(5).

Steeves, C. A. and Fleck, N. (2004a). Collapse mechanisms of sandwich beams with composite faces and a foam core, loaded in three-point bending. Part II: Experimental investigation and numerical modelling. *International Journal of Mechanical Sciences*, 46:585–608.

Steeves, C. A. and Fleck, N. A. (2004b). Collapse mechanisms of sandwich beams with composite faces and a foam core, loaded in three-point bending. Part I: Analytical models and minimum weight design. *International Journal of Mechanical Sciences*, 46:561–583.

Tagarielli, V. L. and Fleck, N. A. (2005). A Comparison of the Structural Response of Clamped and Simply Supported Sandwich Beams With Aluminium Faces and a Metal Foam Core. *Journal of Applied Mechanics*, 72(3):408.

Tagarielli, V. L., Fleck, N. A., and Deshpande, V. S. (2004). Collapse of clamped and simply supported composite sandwich beams in three-point bending. *Composites Part B: Engineering*, 35(6-8):523–534.

Thomsen, O. T., Bozhevolnaya, E., and Lyckegaard, A. (2005). *Sandwich Structures 7: Advancing with Sandwich Structures and Materials*. Proceedings of the 7th International Conference on Sandwich Structures, Aalborg University, Aalborg, Denmark, 29-31 August, Springer.

Triantafillou, T. C. and Gibson, L. J. (1987a). Failure mode maps for foam core sandwich beams. *Materials Science and Engineering*, 95:37–53.

Triantafillou, T. C. and Gibson, L. J. (1987b). Failure mode maps for foam core sandwich beams. *Materials Science and Engineering*, 95:37–53.

Tuttle, M. E. (1988). A Mechanical/Thermal Analysis of Prestressed Composite Laminates. *Journal of Composite Materials*, 22(8):780–792.

Tuttle, M. E., Koehler, R. T., and Keren, D. (1996). Controlling thermal stresses in composites by means of fibre prestress. *Journal of Composite Materials*, 30(4):486–502.

Vasu, T. S. and Bhandakkar, T. K. (2018). Plane strain cylindrical indentation of functionally graded half-plane with exponentially varying shear modulus in the presence of residual surface tension. *International Journal of Mechanical Sciences*, 135(October 2017):158–167.

Xiao, D., Mu, L., and Zhao, G. (2016). Influence of positive gradient metallic cellular core on energy dissipation of sandwich panels under indentation. *Archive of Applied Mechanics*, 86:1901–1911.

Xie, Z. Y., Yu, J. L., and Zheng, Z. J. (2011). A plastic indentation model for sandwich beams with metallic foam cores. *Acta Mechanica Sinica/Lixue Xuebao*, 27(6):963–966.

Yu, T. X. and Stronge, W. J. (1990). Large deflections of a rigid-plastic beam-on-foundation from impact. *International Journal of Impact Engineering*, 9(1):115–126.

Zenkert, D. (1995). *Introduction to Sandwich Construction*. Engineering Materials Advisory Services Ltd.

Zhang, J., Qin, Q., Ai, W., Wang, Z., and Wang, T. J. (2016). Indentation of Metal Foam Core Sandwich Beams: Experimental and Theoretical Investigations. *Experimental Mechanics*, 56(5):771–784.

Ziegler, T. and Kraft, T. (2014). Functionally graded materials with a soft surface for improved indentation resistance: Layout and corresponding design principles. *Computational Materials Science*, 86:88–92.